

**Numerical modelling of classical and quantum effects
in non-linear optical systems**

Von der Fakultät für Mathematik und Physik
der Gottfried Wilhelm Leibniz Universität Hannover
zur Erlangung des Grades

Doktor der Naturwissenschaften
– Dr. rer. nat. –

genehmigte Dissertation
von

Dipl.-Phys. Nico Lastzka

geboren am 5. September 1978 in Nienburg

2010

Referent:	Prof. Dr. Roman Schnabel
Korreferent:	Prof. Dr. Karsten Danzmann
Tag der Promotion:	26.11.2010

Abstract

High precision laser-optical experiments generally include optical resonators and often make use of non-linear materials. Due to the complexity of these setups, simulations are needed in order to optimize their performance.

Within this thesis several numerical simulation tools have been developed aiming for the assistance of high precision laser interferometric experiments. The application N.L.C.S. models a cavity containing a second order non-linear material. The classical fields as well as the quantum mechanical properties such as squeezing and entanglement of the interacting light modes can be calculated for a number of experimental setups. This includes doubly as well as singly resonant systems with arbitrary detuning and phase mismatch. The input beam is treated as a spatially Gaussian beam, leading to a realistic modelling of the interaction within the non-linear material. Due to the numerical nature of the code it is possible to simulate low finesse cavities as well as the single-pass through a non-linear crystal. The analysis of a second-harmonic generator revealed a new effect that influences the effective non-linearity. This effect is due to the Gouy phase shift of the laser beam and has to be taken into account when designing non-linear resonators.

A purely classical simulation was developed to describe the deformation of the Airy peaks from a cavity containing an absorbing material. It is shown that the peak shape depends on the scan direction. This hysteresis is due to a thermally induced self-phase modulation of the light field. Based on this thermo-optical effect a new method for the measurement of small optical absorptions was developed. The simulation shows that the detection of absorptions as low as $10^{-8}/\text{cm}$ should be possible. This may allow for the investigation of new materials for the test masses of the next generation gravitational wave detectors.

The last part of the thesis describes the automatic lock algorithm that was implemented to provide a control of the GEO 600 squeezed light source around the clock. The software was realized by using a *Python* interface to the EPICS channel access protocol. A generic sequential lock algorithm was developed that can readily be used to also control other complex experiments. Another possible operating place could be the gravitational wave detector prototype facility at the Albert-Einstein-Institute.

Keywords: non-linear cavities, absorption measurement, numerical simulation

Kurzfassung

Optische Resonatoren und nichtlineare Materialien kommen in vielen hochpräzisen laseroptischen Experimenten zur Anwendung. Die Komplexität dieser Aufbauten erfordert quantitative Simulationen, um deren Leistungsfähigkeit zu optimieren.

Im Rahmen dieser Doktorarbeit wurden mehrere numerische Simulationen entwickelt. Die Anwendung N.L.C.S. beschreibt einen Resonator, welcher ein Material mit einer Nichtlinearität zweiter Ordnung enthält. Dabei können sowohl die klassischen, als auch die quantenmechanischen Eigenschaften der wechselwirkenden Moden für verschiedene experimentelle Aufbauten berechnet werden. Dazu gehören einfach- und doppelt resonante Systeme mit beliebigen Resonatorverstimnungen und Phasenfehlanspassungen. Der einlaufende Laserstrahl wird hierbei als räumlicher Gauß'scher Strahl behandelt, welches zu einer realistischen Modellierung der Wechselwirkung innerhalb des Kristalls führt. Die numerische Behandlung dieser Systeme ermöglicht die Berechnung von optischen Resonatoren geringer Güte, sowie den einmaligen Durchgang durch ein nichtlineares Medium. Die Anwendung führte zur Entdeckung eines neuen Effektes, welcher zur Verringerung der effektiven Nichtlinearität des Resonators führen kann. Dieser Effekt basiert auf der Gouy-Phase und muß bei dem Entwurf nichtlinearer Resonatoren berücksichtigt werden.

Eine rein klassische Simulation wurde entwickelt, um die Deformationen der „Airy peaks“ eines optischen Resonators zu untersuchen, welcher ein absorbierendes Material beinhaltet. Diese werden durch eine thermisch induzierte Selbstphasenmodulation des Lichtfeldes hervorgerufen. Basierend auf diesem thermo-optischen Effekt wurde eine neue Methode zur Messung von geringen optischen Absorptionen entwickelt. Eine theoretische Vorhersage der Empfindlichkeit zeigt, daß die Detektion von Absorptionen im Bereich von $10^{-8}/\text{cm}$ möglich sein sollte. Dies ermöglicht die Untersuchung von neuen Materialien für die Testmassen der Gravitationswellendetektoren der nächsten Generation.

Im letzten Teil dieser Arbeit wird die computergestützte Steuerung der Quetschlichtquelle für den Gravitationswellendetektor GEO 600 beschrieben. Die Software wurde mit Hilfe der *Python* Schnittstelle zum EPICS „channel access protocol“ programmiert und stellt ein allgemeines Verfahren bereit, um die Regelkreise von Untersystemen eines komplexen Experiments sequentiell zu aktivieren. Sie kann damit auch für andere Experimente übernommen werden. Ein mögliches Anwendungsgebiet sind die Experimente, welche im Rahmen des Gravitationswellendetektor-Prototypen am AEI geplant sind.

Stichworte: nichtlineare Resonatoren, Absorptionsmessung, numerische Simulation

Contents

Abstract	i
Kurzfassung	iii
Contents	vi
List of Figures	viii
List of Tables	ix
1. Introduction	1
2. Physical concepts	5
2.1. Gaussian beams	5
2.2. Description of cavities without non-linearities	10
2.3. The quantum mechanical description of light	11
2.4. Characterization of squeezed light	14
2.5. The covariance matrix of the field quadratures	16
2.6. The second order susceptibility	17
3. N.L.C.S. - The non-linear cavity simulator	21
3.1. The model of a non-linear cavity	21
3.2. Calculation of the classical fields	22
3.3. Calculation of the quantum fluctuations	24
3.3.1. The matrix formalism	24
3.3.2. Implementation of optical loss	28
3.3.3. Calculation of the covariance matrix	28
3.4. The usage of N.L.C.S.	32
3.4.1. Running N.L.C.S. from the command line	32
3.4.2. The input file format	33
3.5. Modelling different regimes	38
3.5.1. Non-linear materials without a cavity	38
3.5.2. Resonators without non-linear materials	43
3.5.3. Squeezing in second harmonic generation	44
3.5.4. Optical parametric oscillation below and above threshold	49

Contents

3.5.5. Kerr squeezing	50
3.6. Error estimation	57
3.7. Influence of the Gouy phase shift	59
4. Modelling thermal effects inside optical cavities	69
4.1. Overview	69
4.2. Estimation of the heating process	70
4.3. Time domain simulation of the cavity	72
4.4. Numerical calculation of the temperature distribution	75
4.5. The simulation code	77
4.6. Airy peak deformation in the presence of absorption	81
4.7. Simulation parameter overview	84
4.8. Determination of the optical absorption	88
5. An automated control system for the GEO 600 squeezer	93
5.1. Introduction to the LIGO Control and Data System	93
5.2. Overview of the GEO 600 squeezed light source	94
5.3. A generic sequential control solution	96
5.4. Using the sequential control interface	101
5.5. Controlling the GEO 600 squeezer	104
5.6. An operator GUI using the Qt libraries	109
A. Self-developed applications	111
A.1. <i>CDSplot</i>	111
A.2. <i>FB_access.py</i>	112
A.3. <i>JamMt</i> - Just another mode matching tool	113
A.4. <i>rtmodule</i>	114
A.5. <i>QtAgilisControl</i>	115
A.6. <i>libaguc2</i>	115
A.7. Extending the power of N.L.C.S.	117
B. Steepest slope position of an Airy peak deformed by the Kerr-effect	119
Bibliography	121
Publications	127
Acknowledgements	129

List of Figures

2.1. Intuitive interpretation of the origin of the Gouy phase shift.	7
2.2. Properties of a Gaussian beam.	8
2.3. Schematic of an empty cavity.	10
2.4. Output power for an empty cavity.	11
2.5. The vacuum state in comparison to a squeezed state.	13
2.6. Schematic of a homodyne detector.	15
3.1. Schematic of a non-linear cavity	22
3.2. Configuration file for N.L.C.S.	35
3.3. N.L.C.S. configuration file for simulating a singly resonant SHG.	37
3.4. Single-pass conversion efficiency vs. phase mismatch.	39
3.5. Single-pass conversion efficiency vs. pump power.	40
3.6. Influence of losses to a squeezed state.	42
3.7. N.L.C.S. configuration file for simulating the entanglement at a beam-splitter.	42
3.8. Entanglement at a beam splitter	43
3.9. Squeezing in reflection of a detuned filter cavity.	45
3.10. Conversion efficiency from an SHG cavity vs. pump power.	46
3.11. SHG squeezing depending on the conversion efficiency.	47
3.12. Shg entanglement depending on the conversion efficiency.	48
3.13. N.L.C.S. configuration file for simulating an OPO.	49
3.14. Squeezing from an OPO cavity.	50
3.15. Purity and entanglement from an OPO cavity.	51
3.16. N.L.C.S. configuration file for simulating a Kerr non-linear cavity.	52
3.17. Operating points for generating Kerr-squeezing.	53
3.18. Deformed Airy peaks from a Kerr resonator.	55
3.19. Kerr squeezing vs. cavity detuning.	56
3.20. Squeezing spectra from a Kerr non-linear cavity	57
3.21. Correction terms for the linearized theory for an OPO below threshold.	59
3.22. Phase matching of Gaussian beams.	62
3.23. Compensation of the Gouy phase in the single-pass.	63
3.24. Schematic of the double-pass through a non-linear crystal.	64
3.25. Effective non-linearity vs. differential phase at the HR stack.	66

List of Figures

4.1.	Schematic of the heat profile due to coating absorption.	71
4.2.	Schematic of an absorbing cavity.	73
4.3.	Code design.	78
4.4.	Schematic of the core calculation.	80
4.5.	The ringing effect from a high finesse cavity.	82
4.6.	Airy peaks from an absorbing cavity.	83
4.7.	Hysteresis effect from an absorbing cavity.	84
4.8.	Grid search for the best parameters.	85
4.9.	Parameters that have only a very weak influence on the result. . . .	86
4.10.	Parameters that have weak influence on the result.	87
4.11.	Parameters that have a high influence on the result.	88
4.12.	Necessary measurement data for determining the absorption.	89
4.13.	Schematic of a hemilithic resonator.	89
4.14.	Results of the first absorption measurement.	90
4.15.	Hysteresis as expected from a crystalline silicon cavity.	91
5.1.	Schematic setup of the GEO 600 squeezed light source.	95
5.2.	Schematic of the automated locking scheme.	99
5.3.	Example log file for the GEO 600 squeezer.	101
5.4.	The configuration file config.py.	102
5.5.	Configuration files for the GEO 600 squeezer.	103
5.6.	Performance of the GEO 600 squeezer.	107
5.7.	Screenshot of the operator GUI for controlling the GEO 600 squeezed light source.	109
A.1.	The main window of <i>CDSplot</i>	112
A.2.	Main window of <i>JamMt</i>	113
A.3.	Main window of <i>QtAgilisControl</i>	115
B.1.	Exact position of the steepest slope of an Airy peak.	120

List of Tables

3.1.	N.L.C.S. parameters for the x and y axes	36
4.1.	Material parameters and estimated values for silicon.	71
4.2.	Overview of the three parameter categories.	86
5.1.	The <i>Controller</i> class.	99
5.2.	Parameters within the configuration file <i>parts_init.py</i>	105
5.3.	Parameters of the <i>dump_spectra</i> script.	106

1. Introduction

Non-linear optical systems have been studied theoretically for half a century now and with the development of the laser [1] it was possible to test these theoretical concepts experimentally. From the first observation of second harmonic generation by Franken et al. in 1961 [2] to the first detection of squeezed states of light by Slusher et al. [3] it took 25 years. It took another 25 years to optimize the squeezed light sources such that the first application of squeezed light in metrology was possible [4, 5]. Currently, the gravitational wave detector GEO 600 has been extended by a squeezed light source [6].

Beyond second harmonic generation and squeezing of laser light, there are more non-linear systems of interest. Many of these are not purely optical. Examples are the opto-mechanical coupling due to radiation pressure noise or the generation of entangled states of light within non-linear materials. Apart from the quantum mechanical point of view, the classical properties of these systems are also of interest. For example an ordinary cavity becomes non-linear if it contains an absorbing material that leads to the heating of either the cavity mirrors or an intra-cavity material. Since the temperature distribution acts back on the light field, the system becomes non-linear and thermo-optical effects can be observed.

In the past, the descriptions of these cavities were naturally based on approximations to understand the physical concepts of these devices. But as the complexity of table top experiments in quantum optics steadily increases, the possibility to realistically model such experiments is very useful. In contrast to a qualitative (and in most cases analytic) theory, where the primary goal is to derive relations between physical quantities, a simulation should yield quantitative results that can be used to optimize real world experiments. Writing such simulations is therefore like performing an experiment inside a computer and builds the interface between the theoretical and experimental world.

For many cases, the equations that describe the physical properties of the optical setups can only be solved numerically. Therefore, the knowledge of programming languages and numerical techniques is required to develop powerful tools that can then be used by experimentalists to design new experiments or to model existing setups.

The rigorous modelling of complex systems can even yield new physical effects that were hidden by similar phenomena. An example is the influence of the Gouy phase shift on the effective non-linearity that is described in Chapter 3. The discovery

1. Introduction

of this effect is important for the optimal design of non-linear resonators and can also be used to increase the single-pass effective non-linearity by using a tighter focusing of the beam as suggested by Boyd and Kleinman [7]. The idea behind it is to make the refractive index dependent on the propagation distance inside a non-linear material. This could be realized by either applying an electrical field or a temperature gradient to the crystal.

This thesis is organized as follows: The first Chapter summarizes physical concepts which are used within the other Chapters and also found their way into the applications that were developed. The latter are shortly explained in the Appendix. The theory that is presented includes the properties and propagation of Gaussian beams and the description of optical resonators. For the quantum mechanical simulations it is necessary to quantize the electro-magnetic field and to introduce the covariance matrix that is a full description of a Gaussian state. From the latter matrix it is then possible to determine the strength of the squeezing, the purity of a state and the entanglement of different modes. The measure that is used for the entanglement within this thesis is the logarithmic negativity [8] which is also described in that Chapter. Lastly, the formal description of the second order non-linear susceptibility is given.

In Chapter 3 the numerical simulation tool N.L.C.S. is described. This tool is able to calculate the classical as well as the quantum mechanical properties of resonators that include second order non-linear crystals. Due to the numerical nature of the application, all system parameters that influence the effective non-linearity are included such that experiments can be described precisely. This is the major difference to the usual calculation that uses the effective non-linearity as a free parameter. This is also the reason why N.L.C.S. can be used to simulate low finesse cavities and even single-pass setups correctly. The usage of the application lead also to the discovery of the Gouy phase effect that was already mentioned. Based on this result, an analytical treatment of this effect was performed.

The theoretical description of a new scheme to measure tiny optical absorptions based on a thermally induced self-phase modulation is then described in Chapter 4. The experience in modelling non-linear resonators that was gained from the previous Chapter was combined with the modelling of the time and position dependent temperature distribution caused by the absorption of a Gaussian beam which was developed by Hello and Vinet [9, 10]. First measurements to prove the usability of this method were performed and the results were recently published [11]. It is further planned to use this method to examine materials for the next generation gravitational wave detectors. These detectors are already limited by absorptions of as low as $10^{-6}/\text{cm}$ because of thermal deformations of the mirrors and also photo-thermal noise [12, 13]. The new scheme is expected to reach a sensitivity of $10^{-8}/\text{cm}$ which would make it possible to measure the absorption of crystalline silicon [14].

The last Chapter describes the automatic control of the squeezed light source for

the GEO 600 gravitational wave detector. As this component has to be operated around the clock, a software was developed to automate the task of (re-)locking the components of the squeezer. The software is based on the Control and Data System (CDS) that is developed and operated at the LIGO sites and the Experimental Physics and Industrial Control System (EPICS). These software suites have been designed to operate large scale experiments, where the latter originates from the particle accelerators that are operated world-wide. The automatic control was implemented by using the EpicsCA interface to the EPICS channel access protocol and provides a generic sequential lock algorithm that can readily be used by other experiments.

2. Physical concepts

In this Chapter I summarize the theoretical foundations on which the following Chapters rely on. The first topic is the classical description of a laser beam as a transverse electromagnetic mode and its transformation by using the ABCD matrix formalism. As these modes are also the eigenmodes of an optical resonator, the properties of such a device are presented. The quantization of the electro-magnetic field then leads to the description of squeezed states of light and its detection by using the covariance matrix of a Gaussian state. As these states are generated from non-linear processes, the last Section describes the second order non-linearity $\chi^{(2)}$.

2.1. Gaussian beams

The propagation of electromagnetic fields in free space is governed by the following scalar wave equation

$$[\nabla^2 + k^2]\bar{E}(x, y, z) = 0, \quad (2.1)$$

where \bar{E} is the complex electrical field and $k = 2\pi/\lambda$ is the wave vector. For a beam propagating along the z axis the plane wave variation of the field e^{-ikz} , which has a period of the wavelength λ , is assumed to be faster than the transversal variations across any plane z . It is therefore convenient to introduce the scalar wave amplitude $u(x, y, z)$ by the definition

$$\bar{E}(x, y, z) = \bar{u}(x, y, z)e^{-ikz}. \quad (2.2)$$

Inserting this into Equation 2.1 yields the reduced equation

$$(\partial_x^2 + \partial_y^2 + \partial_z^2 - 2ik\partial_z)\bar{u} = 0. \quad (2.3)$$

The remaining dependency from the longitudinal coordinate z is mainly due to diffraction effects which will in general be slow compared to the transverse variations due to the finite width of the beam. Mathematically this assumption is expressed by the paraxial approximation

$$|\partial_z^2 \bar{u}| \ll |2k\partial_z \bar{u}|, \quad (2.4)$$

$$|\partial_z^2 \bar{u}| \ll |\partial_x^2 \bar{u}|, \quad (2.5)$$

$$|\partial_z^2 \bar{u}| \ll |\partial_y^2 \bar{u}|. \quad (2.6)$$

2. Physical concepts

This leads to the wave equation in the final form

$$(\partial_x^2 + \partial_y^2 - 2ik\partial_z)\bar{u} = 0. \quad (2.7)$$

As shown by Siegman [15], this paraxial wave equation is valid for beams with a divergence angle of up to $\theta_{div} \approx 30^\circ$. One possible set of solutions to this equation is

$$u_{nm}(x, y, z) = u_n(x, z)u_m(y, z), \quad (2.8)$$

with

$$u_n(x, z) = \left(\frac{2}{\pi}\right)^{1/4} \left(\frac{1}{2^n n! w_0 q(z)}\right)^{1/2} \left(\frac{q_0 q^*(z)}{q_0^* q(z)}\right)^{n/2} H_n\left(\frac{\sqrt{2}x}{w(z)}\right) e^{-i\frac{kx^2}{2q(z)}}. \quad (2.9)$$

These solutions are called the transverse electromagnetic modes (TEM_{mn}) of the radiation field. Here, H_n is the Hermite polynomial of order n , $w(z)$ is the beam radius which is given by

$$w(z) = \sqrt{\frac{\lambda}{\pi} \frac{|q|^2}{\Im(q)}}, \quad (2.10)$$

and the complex beam parameter q is given by

$$\frac{1}{q(z)} = \frac{1}{R_c(z)} - i\frac{\lambda}{\pi w^2(z)}. \quad (2.11)$$

The latter can also be written as

$$q(z) = i z_R + z - z_0 = q_0 + z - z_0, \quad (2.12)$$

where z_0 is the waist position and z_R is the Rayleigh range given by

$$z_R = \frac{\pi w_0^2}{\lambda}. \quad (2.13)$$

The radius of curvature at position z for this beam reads

$$R_c(z) = \frac{|q|^2}{\Re(q)}. \quad (2.14)$$

The divergence angle θ_{div} of the beam, i.e. the angle between the z -axis and $w(z)$ in the far field, is given by

$$\theta_{div} = \arctan\left(\frac{\lambda}{\pi w_0}\right). \quad (2.15)$$

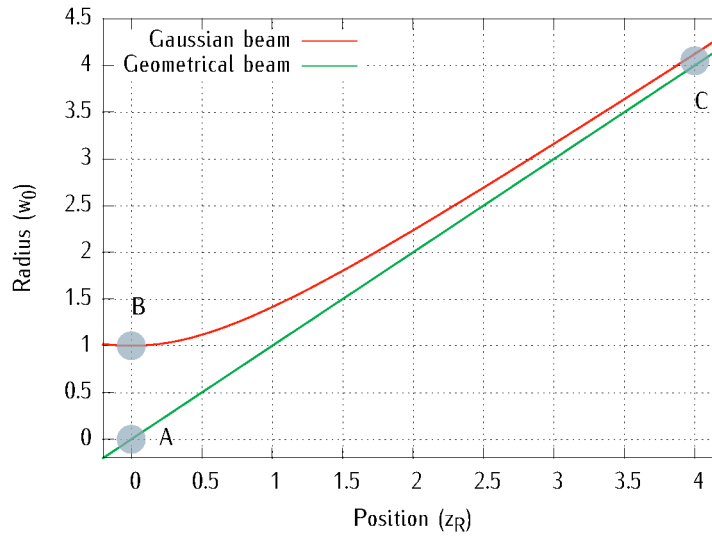


Figure 2.1.: Intuitive interpretation of the origin of the Gouy phase shift as given by Boyd [16]. The distance between A and C is longer than the distance between B and C . Therefore the Gaussian beam is slightly faster than the corresponding geometrical beam when passing the focus, leading to the phase shift that is described by the Gouy phase.

There is also an additional phase compared to plane waves that is known as the Gouy phase shift. For the TEM_{mn} mode it is given by

$$\phi_G(z) = -(n + m + 1) \arctan \left(\frac{z - z_0}{z_R} \right). \quad (2.16)$$

An intuitive interpretation of this phase shift was given by Boyd [16]. He argued that the Gouy phase is due to the shorter distance a beam has to propagate while passing the focus compared to a beam in geometrical optics (see Figure 2.1). This interpretation can not describe the actual dependence of the Gouy phase from the propagation distance, but it explains the total phase shift of 180 degrees when passing the focus of a beam. For a more accurate description see the paper by Feng and Winful [17]. Figure 2.2 summarizes the main properties of the TEM_{00} mode which is also called a Gaussian beam.

The transformation of TEM_{mn} modes when passing optical components can be performed by the ABCD matrix formalism. The complex beam parameter q_2 after

2. Physical concepts

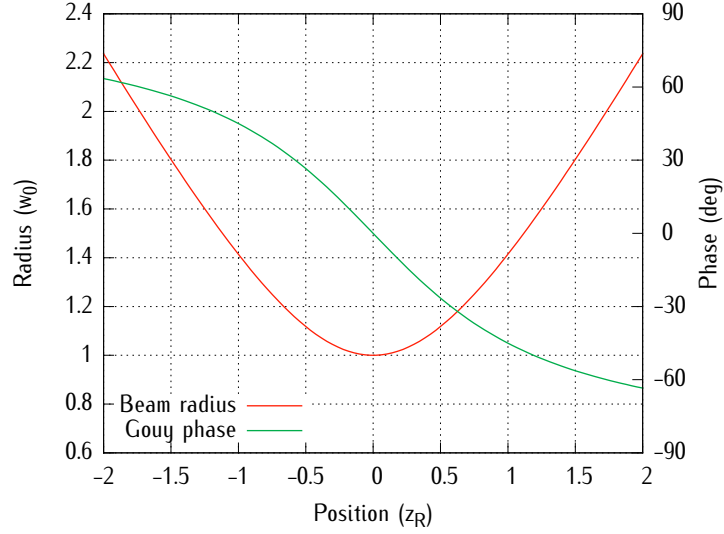


Figure 2.2.: Properties of a Gaussian beam (TEM_{00}). The beam radius at the Rayleigh range is $\sqrt{2}$ times larger than the waist of the beam and the Gouy phase amounts to $\phi_G = \pm 45^\circ$.

the transformation is given by

$$\frac{q_2}{n_2} = \frac{A \frac{q_1}{n_1} + B}{C \frac{q_1}{n_1} + D}, \quad (2.17)$$

where n_1 and n_2 are the refractive indices of the corresponding media and q_1 is the original beam parameter. The coefficients are given by the transformation matrix

$$M = \begin{pmatrix} A & B \\ C & D \end{pmatrix}. \quad (2.18)$$

The modematching tool *JamMt* which is described in Appendix A.3 uses the ABCD matrix formalism for the propagation of a Gaussian beam. Within the thin lens approximation only the matrices for propagating a distance d inside a medium with a refractive index n and the transmission through a thin lens with focal length f are needed. These matrices are given by [18]

$$M_p = \begin{pmatrix} 1 & \frac{d}{n} \\ 0 & 1 \end{pmatrix}, \quad (2.19)$$

$$M_f = \begin{pmatrix} 1 & 0 \\ -\frac{1}{f} & 1 \end{pmatrix}. \quad (2.20)$$

2.2. Description of cavities without non-linearities

As *JamMt* can also simulate thick (real) lenses, which might be tilted by an angle α_1 with respect to the incident beam, the matrix for propagating through an interface with arbitrary radius of curvature R is needed as well. This matrix is given by

$$M_i = \begin{pmatrix} \frac{\cos(\alpha_2)}{\cos(\alpha_1)} & 0 \\ \frac{\Delta n}{R} & \frac{\cos(\alpha_1)}{\cos(\alpha_2)} \end{pmatrix}, \quad (2.21)$$

$$\Delta n = \frac{n_2 \cos(\alpha_2) - n_1 \cos(\alpha_1)}{\cos(\alpha_1) \cos(\alpha_2)}, \quad (2.22)$$

where the angle α_2 is given by Snell's law

$$n_1 \sin(\alpha_1) = n_2 \sin(\alpha_2). \quad (2.23)$$

The transformation by a thick lens, which is called a substrate within *JamMt*, is then given by a product of a propagation and two interface matrices.

For the eigenmode calculation of an optical resonator, the reflection off a curved interface with radius R is needed, which is given by

$$M_R = \begin{pmatrix} 1 & 0 \\ -\frac{2n}{R} & 1 \end{pmatrix}. \quad (2.24)$$

As the eigenmode has to reproduce its beam parameter after one round trip inside the resonator, the following equation has to be satisfied

$$q = \frac{Aq + B}{Cq + D} \rightarrow Cq^2 + (D - A)q - B = 0, \quad (2.25)$$

where A , B , C and D are the elements of the product matrix that describes the round trip. The waist position z_0 and the Rayleigh range z_R are then given by [19]

$$z_0 = z_1 - \frac{A - D}{2C}, \quad (2.26)$$

$$z_R = \frac{\sqrt{4 - (A + D)^2}}{2|C|}, \quad (2.27)$$

where z_1 is the reference plane, i.e. the plane where the round trip started. Note that the Rayleigh range is only defined if the radicand is bigger than zero. This leads to the stability criterion for an optical resonator

$$-1 < g = \frac{1}{2}(A + D) < 1, \quad (2.28)$$

where g is called the stability parameter of the cavity.

2. Physical concepts

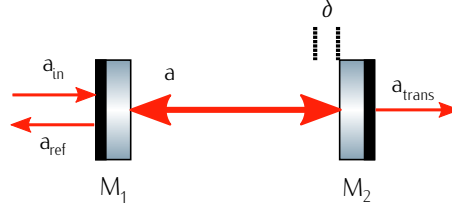


Figure 2.3.: Schematic of an empty cavity. The field a is confined by the two mirrors M_1 and M_2 . For zero detuning δ the cavity is on resonance and the intra-cavity field reaches its maximum. The output fields in transmission and reflection of the resonator are denoted by a_{trans} and a_{ref} , respectively.

2.2. Description of cavities without non-linearities

The schematic of an empty optical resonator is shown in Figure 2.3. An optical field a_{in} is coupled into the resonator consisting of the two mirrors M_1 and M_2 . The mirrors have an amplitude reflectivity r_1 and r_2 , respectively. For the lossless case, the mirror transmissivities are given by the relation $t = \sqrt{1 - r^2}$. The intra-cavity field a is defined right after the first mirror and the output fields in transmission and reflection are denoted by a_{trans} and a_{ref} , respectively. Further, the field a gains a phase 2δ while travelling through the resonator. This phase is also called the *detuning* of the cavity.

In the steady state the intra-cavity field a has to fulfil the following self-consistency equation

$$a = t_1 a_{in} + r_1 r_2 e^{2i\delta} a. \quad (2.29)$$

Solving this equation for the intra-cavity field yields the expression

$$a = \frac{t_1 a_{in}}{1 - r_1 r_2 e^{2i\delta}}, \quad (2.30)$$

from which the two output fields can be calculated by the relations

$$a_{trans} = t_2 e^{i\delta} a = -\frac{t_1 t_2 e^{i\delta}}{1 - r_1 r_2 e^{2i\delta}} a_{in}, \quad (2.31)$$

$$a_{ref} = r_1 a_{in} + t_1 r_2 e^{2i\delta} a = \left(r_1 - \frac{t_1^2 r_2 e^{2i\delta}}{1 - r_1 r_2 e^{2i\delta}} \right) a_{in}. \quad (2.32)$$

The output power for both ports normalized to the input power is plotted in Figure 2.4. The periodicity of the peaks is given by the free spectral range (FSR) which is given by

$$\text{FSR} = \frac{c}{2L}, \quad (2.33)$$

2.3. The quantum mechanical description of light

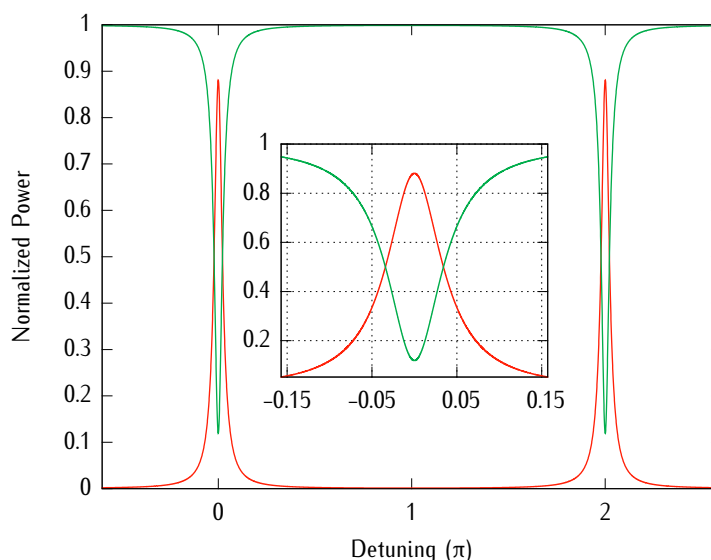


Figure 2.4.: Output power for an empty cavity in transmission and reflection depending on the cavity detuning. The power was normalized to the input power. The inset is a zoom of the single peaks.

where c is the speed of light and L is the optical path length for half a round-trip. The full width at half maximum (FWHM) is defined as the range in which the peak drops to half of its maximum value. This quantity is given by the relation [20]

$$\text{FWHM} = 2 \arccos \left(1 - \frac{(1 - r_1 r_2)^2}{2r_1 r_2} \right). \quad (2.34)$$

Another important quantity is the finesse F which is defined by

$$F = \frac{\text{FSR}}{\text{FWHM}} \approx \frac{\pi \sqrt{r_1 r_2}}{1 - r_1 r_2}, \quad (2.35)$$

where the approximation is valid for finesse values of greater than 6.4 with only an error of 1 % compared to the exact value.

2.3. The quantum mechanical description of light

This section gives a short summary of the quantization of the electromagnetic field and defines the operators as they are used within this thesis.

2. Physical concepts

The Hamilton operator for the harmonic oscillator is given by

$$H = hf\left(\hat{a}^\dagger \hat{a} + \frac{1}{2}\right), \quad (2.36)$$

where h is Planck's constant and f is the frequency of the oscillator. The eigenstates of the number operator $\hat{n} = \hat{a}^\dagger \hat{a}$ are the so-called Fock states $|n\rangle$. Their eigenvalue n is the number of energy quanta (photons) of the state. The operators \hat{a} and \hat{a}^\dagger are defined by the relations

$$\hat{a}|n\rangle = \sqrt{n}|n-1\rangle, \quad (2.37)$$

$$\hat{a}^\dagger|n\rangle = \sqrt{n+1}|n+1\rangle. \quad (2.38)$$

Their action on a Fock state is to annihilate and create photons. The commutator relation of these operators reads

$$[\hat{a}, \hat{a}^\dagger] = 1, \quad (2.39)$$

which means that a Heisenberg uncertainty relation is connected to these operators and any derived operators. As the annihilation and creation operators are not hermitian, and therefore not observable, it is necessary to form a hermitian operator

$$\hat{X}^\theta = \hat{a}e^{-i\theta} + \hat{a}^\dagger e^{i\theta}, \quad (2.40)$$

which is called the general quadrature operator. Using the definition of the amplitude (\hat{X}^+) and phase (\hat{X}^-) quadrature of an electromagnetic field, it is possible to write the quadrature operator in the form

$$\hat{X}^\theta = \hat{X}^+ \cos(\theta) + \hat{X}^- \sin(\theta), \quad (2.41)$$

$$\hat{X}^+ = \hat{a}^\dagger + \hat{a}, \quad (2.42)$$

$$\hat{X}^- = i(\hat{a}^\dagger - \hat{a}). \quad (2.43)$$

These new quadrature operators fulfil the commutation relation

$$[\hat{X}^+, \hat{X}^-] = 2i, \quad (2.44)$$

which leads to the following Heisenberg uncertainty relation

$$\Delta\hat{X}^+ \Delta\hat{X}^- \geq 1. \quad (2.45)$$

From this it follows that even a Fock state without any photons (*vacuum state*) shows some fluctuations of the quadrature operator. While its mean value is still zero in this case, the variance is given by

$$\langle 0 | \left(\hat{X}^\theta \right)^2 | 0 \rangle = 1, \quad (2.46)$$

2.3. The quantum mechanical description of light

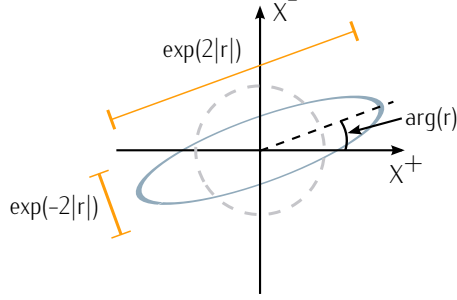


Figure 2.5.: The vacuum state in comparison to a squeezed state in quadrature space. The complex squeezing parameter $r = |r| \exp(i \arg(r))$ determines the strength of the squeezing and the orientation of the squeezing ellipse.

which means that the vacuum state is a minimum uncertainty state with equal noise for any quadrature angle θ .

As the Heisenberg uncertainty principle makes a statement about the product of two quantities, it is of course allowed to reduce one of the quadrature variances at the cost of increasing the other one. These states are called squeezed states of light and are mathematically generated by applying the squeeze operator \hat{S} to a vacuum state

$$|s\rangle = \hat{S}|0\rangle = e^{\frac{1}{2}(r^* \hat{a}^2 - r \hat{a}^{\dagger 2})}|0\rangle, \quad (2.47)$$

where the complex squeezing parameter r determines the strength and the quadrature of the squeezing. The comparison between a vacuum state and a squeezed state is depicted in Figure 2.5. Because the squeezing operator involves the annihilation and creation of two photons at the same time, it is necessary to use non-linear optical processes to create squeezed states of light.

The generation of squeezing at a sideband frequency Ω can be described by creating one photon at the upper and lower sideband each. The mathematical formalism was developed by Caves and Schumaker [21] and is known as the two-photon formalism. The quantization of classical modulation sidebands around the carrier leads to a new class of operators. These operators are a generalization of the creation and annihilation operators which operate on single photons. With the definition $\hat{a}_{\pm} = \hat{a}(\omega_0 \pm \Omega)$ the new operators read

$$\hat{a}_1(\Omega) = \sqrt{\frac{\omega_0 + \Omega}{2\omega_0}} \hat{a}_+ + \sqrt{\frac{\omega_0 - \Omega}{2\omega_0}} \hat{a}_-^{\dagger}, \quad (2.48)$$

$$\hat{a}_2(\Omega) = -i\sqrt{\frac{\omega_0 + \Omega}{2\omega_0}} \hat{a}_+ + i\sqrt{\frac{\omega_0 - \Omega}{2\omega_0}} \hat{a}_-^{\dagger}, \quad (2.49)$$

where ω_0 is the carrier frequency. For optical fields the sideband frequency can be

2. Physical concepts

assumed to be much smaller than the carrier frequency. In this limit the operators become hermitian and are therefore observables.

2.4. Characterization of squeezed light

For the detection of squeezed light, a balanced homodyne readout scheme is frequently used. It is based on overlapping the squeezed state with a strong local oscillator beam on a 50/50 beam splitter. The general situation of interfering two light fields on a beam splitter with amplitude reflectivity r and transmissivity t is shown in Figure 2.6.

The output fields b_1 and b_2 can in general be written as

$$b_1 = te^{i\phi_3}a_1 + re^{i\phi_4}a_2, \quad (2.50)$$

$$b_2 = te^{i\phi_1}a_2 + re^{i\phi_2}a_1, \quad (2.51)$$

where the reflection and transmission may introduce the phases ϕ_i ($i \in [1; 4]$). For the lossless case, the conservation of energy requires that

$$|a_1|^2 + |a_2|^2 = |b_1|^2 + |b_2|^2. \quad (2.52)$$

This leads to the following equation

$$|b_1|^2 + |b_2|^2 = (t^2 + r^2)(|a_1|^2 + |a_2|^2) + 2rt\Re\{a_1a_2^*e^{i\Delta\phi_{34}} + a_1^*a_2e^{i\Delta\phi_{12}}\}, \quad (2.53)$$

where the difference phases are defined by

$$\Delta\phi_{ij} = \phi_i - \phi_j. \quad (2.54)$$

It follows that the lossless beam splitter has to fulfil the two equations

$$r^2 + t^2 = 1, \quad (2.55)$$

$$\Delta\phi_{12} + \Delta\phi_{34} = \pi. \quad (2.56)$$

One common choice of the phases is the symmetric case, where $\phi_1 = \phi_3 = \pi/2$ and $\phi_2 = \phi_4 = 0$. This is especially useful for actual calculation, because you don't have to distinguish the input modes, but rather assign a $\pi/2$ phase shift for each transmission and a zero phase shift for each reflection. In cases where an additional phase ϕ_{coat} is introduced by the coating in reflection (see text around Equation 3.99), the above phase relation requires a different sign for these phases, i.e. $\phi_2 = \phi_{\text{coat}}$ and $\phi_4 = -\phi_{\text{coat}}$, which makes it necessary to carefully distinguish the two input modes and assign the correct phases to them.

2.4. Characterization of squeezed light

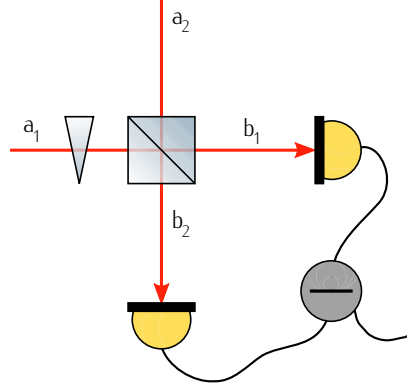


Figure 2.6.: Two optical fields are combined at a beam splitter with amplitude reflectivity r and transmissivity t . The difference current of the two photodiodes provides information about the noise properties of the state.

The balanced homodyne detection scheme can now be described by the symmetric choice of phases with equal values for the reflection and transmission $r = t = \sqrt{1/2}$. The input field operators \hat{a}_1 and \hat{a}_2 can generally be written as

$$\hat{a}_1 = a_1 + \delta\hat{a}_1, \quad (2.57)$$

$$\hat{a}_2 = a_2 + \delta\hat{a}_2, \quad (2.58)$$

where a_1 and a_2 are now the expectation values of the operators, whereas $\delta\hat{a}_1$ and $\delta\hat{a}_2$ describe the noise of the fields. The mean value of the noise operators is by definition zero, since

$$\langle \delta\hat{a} \rangle = \langle \hat{a} - a \rangle = a - a = 0. \quad (2.59)$$

If we now assign an arbitrary phase θ to the local oscillator beam and further assume that this beam \hat{a}_1 is much stronger than the signal beam \hat{a}_2 , we end up with the following expressions for the photocurrents at the two output ports

$$I_1 = b_1^\dagger b_1 = \frac{a_1}{2} \left(\delta\hat{X}_1^+ + \delta\hat{X}_2^\theta \right) + \text{DC} + O(\delta^2) \quad (2.60)$$

$$I_2 = b_2^\dagger b_2 = \frac{a_1}{2} \left(\delta\hat{X}_1^+ - \delta\hat{X}_2^\theta \right) + \text{DC} + O(\delta^2), \quad (2.61)$$

where $\delta\hat{X}_1^+$ is the amplitude quadrature of the local oscillator and $\delta\hat{X}_2^\theta$ is the quadrature noise of the signal beam at angle θ . The DC term summarizes all the terms that are constant, i.e. do not contain any noise operator, whereas the term $O(\delta^2)$ contains all terms that are proportional to the square of two noise operators. The latter terms can be neglected as they are usually much smaller than the other terms.

2. Physical concepts

The sum and difference of the photocurrent fluctuations is now given by

$$I_+ = I_1 + I_2 = a_1 \delta \hat{\chi}_1^+, \quad (2.62)$$

$$I_- = I_1 - I_2 = a_1 \delta \hat{\chi}_2^\theta. \quad (2.63)$$

This result is quite remarkable because it allows to measure any quadrature of the signal beam by adjusting the phase of the local oscillator beam and looking at the difference current of the two homodyne photodiodes.

2.5. The covariance matrix of the field quadratures

If the fluctuations of the quadrature operator $\delta \hat{\chi}^\theta$ obey a Gaussian probability distribution for all quadrature angles θ , the state is said to be a *Gaussian state*. As this distribution is completely described by its mean and variance and the phase space is defined by two orthogonal quadratures $\delta \hat{\chi}^\theta$ and $\delta \hat{\chi}^{\theta+\pi/2}$, a Gaussian state is completely characterized by its covariance matrix γ that is defined by

$$\gamma = \begin{pmatrix} \langle (\delta \hat{\chi}^\theta)^2 \rangle & \frac{1}{2} \langle \delta \hat{\chi}^\theta \delta \hat{\chi}^{\theta+\pi/2} + \delta \hat{\chi}^{\theta+\pi/2} \delta \hat{\chi}^\theta \rangle \\ \frac{1}{2} \langle \delta \hat{\chi}^\theta \delta \hat{\chi}^{\theta+\pi/2} + \delta \hat{\chi}^{\theta+\pi/2} \delta \hat{\chi}^\theta \rangle & \langle (\delta \hat{\chi}^{\theta+\pi/2})^2 \rangle \end{pmatrix}. \quad (2.64)$$

For a physical state that obeys the Heisenberg uncertainty principle, the covariance matrix has to fulfil

$$\det(\gamma + i\Omega) > 0, \quad \Omega = \begin{pmatrix} 0 & 1 \\ -1 & 0 \end{pmatrix}, \quad (2.65)$$

where $\det(M)$ is the determinant of the matrix M . The determinant of the covariance matrix itself is a measure of the purity ρ of the state which is defined by

$$\rho = \frac{1}{\sqrt{\det(\gamma)}}. \quad (2.66)$$

On the main diagonal of the matrix the variance V of the orthogonal quadratures $\delta \hat{\chi}^\theta$ and $\delta \hat{\chi}^{\theta+\pi/2}$ are placed, from which the squeezing strength on a logarithmic scale V_{dB} can be gained by the relation

$$V_{\text{dB}} = 10 \log_{10}(V), \quad (2.67)$$

which is due to the vacuum state having a variance $V = 1$.

To find the optimal squeezing angle from the covariance matrix a principal axis transformation has to be performed. With the definition

$$\gamma = \begin{pmatrix} A & B \\ B & D \end{pmatrix}, \quad (2.68)$$

2.6. The second order susceptibility

the angles for the two principal axis are given by

$$\phi_{\pm} = \arctan\left(\frac{V_{\pm} - A}{B}\right) \quad (2.69)$$

and the variances V_{\pm} in the new coordinate system are given by

$$V_{\pm} = \frac{\text{tr}(\gamma)}{2} \pm \sqrt{\frac{\text{tr}(\gamma)^2}{4} - \det(\gamma)}. \quad (2.70)$$

For the case that $B = 0$ the covariance matrix is already represented in the basis of the principal axis so that the angles ϕ_{\pm} are zero and $\pi/2$, respectively.

Another quantity of interest is the entanglement of any two modes of the system. As a measure for the entanglement we use the so-called logarithmic negativity [8], which is an easy to calculate quantity for Gaussian states. Given the two-mode covariance matrix γ in the form

$$\gamma = \begin{pmatrix} A & C \\ C^T & B \end{pmatrix}, \quad (2.71)$$

with the 2×2 matrices A , B and C , the logarithmic negativity E_N is given by

$$E_N = \sum_i F(c_i). \quad (2.72)$$

Here, the function $F(c)$ is defined by

$$F(c) = \begin{cases} 0 & \text{for } 2c \geq 1 \\ -\log_2(2c) & \text{else,} \end{cases} \quad (2.73)$$

and the eigenvalues c_i are calculated by solving the equation

$$c^4 + (\det(A) + \det(B) - 2\det(C))c^2 + \det(\gamma) = 0. \quad (2.74)$$

2.6. The second order susceptibility

In this Section the non-linear coupling constant is explained that is used for the simulation of cavities that include a material with a non-vanishing second order susceptibility. For a more detailed description of non-linear optics see for example the book of Boyd [22].

An electrical field generally leads to a polarization P inside a material that might be expanded into a series

$$P = \sum_i \chi^{(i)} E^i, \quad (2.75)$$

2. Physical concepts

where $\chi^{(i)}$ is the optical susceptibility of order i and E is the electrical field amplitude. Within this thesis we will only focus on the second order non-linearity $\chi^{(2)}$. The polarization caused by only $\chi^{(2)}$ can be written as

$$P_i(\omega_n + \omega_m) = \sum_{jk} \sum_{(nm)} \chi_{ijk}^{(2)}(\omega_n + \omega_m, \omega_n, \omega_m) E_j(\omega_n) E_k(\omega_m), \quad (2.76)$$

where i, j and k are the Cartesian coordinates of the vectors \vec{P} and \vec{E} and ω_n are the frequencies of the optical fields. The brackets around the indices n and m indicate that the sum is taken with the restriction of a constant value of $\omega_n + \omega_m$.

This equation requires that all of the 324 complex elements of the $\chi_{ijk}^{(2)}$ tensor have to be known in order to describe the non-linear interaction. In order to reduce the number of independent tensor elements one can exploit several symmetries of the $\chi^{(2)}$ tensor. Since the polarization \vec{P} and the optical fields \vec{E} have to be real quantities one can conclude that

$$P(-\omega) = P(\omega)^*, \quad E(-\omega) = E(\omega)^* \quad (2.77)$$

$$\rightarrow \chi_{ijk}^{(2)}(-\omega_n - \omega_m, -\omega_n, -\omega_m) = (\chi_{ijk}^{(2)}(\omega_n + \omega_m, \omega_n, \omega_m))^*. \quad (2.78)$$

Another relation is due to the intrinsic symmetry of the tensor. Since j, k, n and m are dummy indices, it is allowed to just interchange j, k and n, m leading to the following restriction of the $\chi^{(2)}$ tensor

$$\chi_{ijk}^{(2)}(\omega_n + \omega_m, \omega_n, \omega_m) = \chi_{ikj}^{(2)}(\omega_n + \omega_m, \omega_m, \omega_n). \quad (2.79)$$

The other symmetries are valid for lossless materials which means that all optical frequencies involved are far away from a resonance frequency. One can then show that the $\chi_{ijk}^{(2)}$ tensor is real and obeys full permutation symmetry. The latter results in the following relations

$$\chi_{ijk}^{(2)}(\omega_1 + \omega_2, \omega_1, \omega_2) = \chi_{jki}^{(2)}(\omega_3 - \omega_2, -\omega_2, \omega_3), \quad (2.80)$$

$$\chi_{ijk}^{(2)}(\omega_1 + \omega_2, \omega_1, \omega_2) = \chi_{kij}^{(2)}(\omega_3 - \omega_1, \omega_3, -\omega_1). \quad (2.81)$$

Lastly, the so-called Kleinman symmetry states that the $\chi_{ijk}^{(2)}$ tensor is frequency independent whenever the lowest resonance frequency of the material is higher than all the optical frequencies that are involved in the non-linear process. This leads to the relations

$$\chi_{ijk}^{(2)} = \chi_{jki}^{(2)} = \chi_{kij}^{(2)} = \chi_{ikj}^{(2)} = \chi_{jik}^{(2)} = \chi_{kji}^{(2)}, \quad (2.82)$$

which make it possible to define the matrix $d_{il} = \frac{1}{2}\chi_{il}^{(2)}$ where the index l is mapped to the indices j, k in the following manner

2.6. The second order susceptibility

$$\begin{array}{l} jk : 11 \quad 22 \quad 33 \quad 23, 32 \quad 31, 13 \quad 12, 21 \\ l : 1 \quad 2 \quad 3 \quad 4 \quad 5 \quad 6 \end{array} .$$

This leads to the following 3×6 matrix

$$d_{il} = \begin{pmatrix} d_{11} & d_{12} & d_{13} & d_{14} & d_{15} & d_{16} \\ d_{21} & d_{22} & d_{23} & d_{24} & d_{25} & d_{26} \\ d_{31} & d_{32} & d_{33} & d_{34} & d_{35} & d_{36} \end{pmatrix}, \quad (2.83)$$

which has only 10 independent real elements.

The effective non-linearity d_{eff} can now be calculated for a given propagation direction and polarization of the interacting fields by actually performing the summation over the indices j and k in the equation

$$P_l(\omega_n + \omega_m) = \sum_{jk} \sum_{(nm)} 2d_{il} E_j(\omega_n) E_k(\omega_m). \quad (2.84)$$

A list of the effective non-linearities for different crystals can be found in [23].

3. N.L.C.S. – The non-linear cavity simulator

In this chapter a new numerical tool is introduced that is able to simulate the classical as well as the quantum mechanical properties of a cavity containing a non-linear medium with a second-order susceptibility. The pump beams are treated as Gaussian beams which leads to a realistic description of these cavities. Due to the numerical treatment singly-resonant as well as doubly-resonant resonators can be described precisely. In contrast to other methods, the non-linear coupling includes arbitrary beam parameters and phase mismatch and is therefore able to predict the behaviour of the system for a variety of experimental setups. The tool can be downloaded at [24].

3.1. The model of a non-linear cavity

Figure 3.1 shows a schematic of the non-linear cavity that can be handled by the simulation. The resonator is build by the mirrors M_1 and M_2 and can be pumped by using the two input ports in_1 and in_2 with fields at the idler, signal and harmonic wavelength. The remaining mirrors V_1 and V_2 are used to simulate losses within the non-linear material by coupling vacuum states into these additional ports. The output ports that are relevant are out_1 and out_2 which are referred to as the reflection and transmission port, respectively. The cavity detuning δ is equally split for each single-pass through the non-linear materials nlc_1 and nlc_2 . The two different crystals within the simulation were chosen to stay as general as possible. This way it is possible to describe a standing-wave as well as a travelling-wave cavity or even placing two different crystals (e.g. different phase mismatches) inside the resonator. The only difference of these cavity layouts is that for a standing-wave cavity, the crystals nlc_1 and nlc_2 are physically identical. Only the propagation direction of the light differs which might lead to a change in the waist position. For a travelling-wave resonator it is generally possible to use two different crystals within only one cavity. The most common case would still be to use a bow-tie setup that uses only one crystal. This can be simulated by setting either one of the non-linearities to zero.

Furthermore, the intra-cavity field has been split up into the fields c_1 (right after mirror M_1), c'_1 (right before mirror M_2), c_2 (right after mirror M_2) and c'_2 (right before mirror M_1). The fields with a prime belong to the primeless fields that were

3. N.L.C.S. - The non-linear cavity simulator

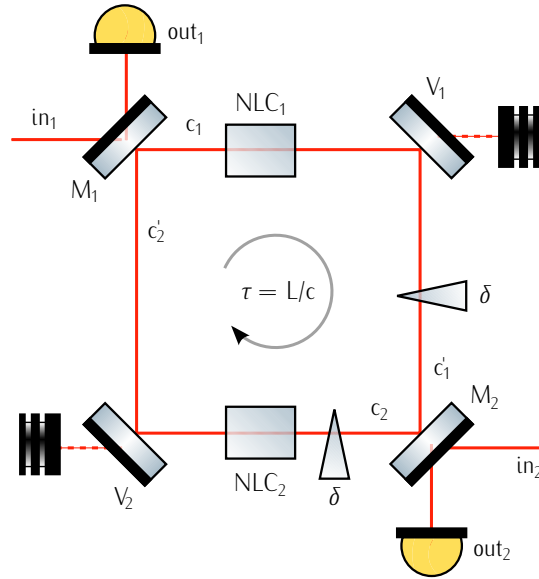


Figure 3.1.: Schematic overview of the non-linear cavity that can be handled by the numerical simulation.

just propagated by a single-pass through a non-linear crystal, reflected at the loss introducing mirror and then propagated through free space to gain the detuning phase δ . The simulation is performed in time-domain using the discrete time steps $\tau = L/c$, where c is the speed of light and L the optical path for one round-trip inside the resonator.

3.2. Calculation of the classical fields

For the calculation of the classical fields, a numerical time-domain simulation is used. This is necessary, because of the description of the non-linear interaction of Gaussian beams, which in general can not be solved analytically. The simulation propagates the field c_1 for each mode through the whole resonator every single round-trip and compares the successive fields. If the difference of these fields undergoes a certain limit the cavity has reached its steady state and the calculation stops. From the steady state value of the field c_1 it is then possible to determine the remaining fields inside the cavity as well as the output fields.

To describe the non-linear interaction within the intra-cavity material, the fol-

3.2. Calculation of the classical fields

Following set of equations for the amplitudes of the fields is used [25]

$$\partial_z A_s = -\iota\kappa(\lambda_s)f(z)A_i^*A_b - \frac{\alpha_s}{2}A_s, \quad (3.1)$$

$$\partial_z A_i = -\iota\kappa(\lambda_i)f(z)A_s^*A_b - \frac{\alpha_i}{2}A_i, \quad (3.2)$$

$$\partial_z A_b = -\iota\kappa(\lambda_b)f^*(z)A_sA_i - \frac{\alpha_b}{2}A_b, \quad (3.3)$$

where the indices i , s and b denote the idler, signal and harmonic mode, respectively. The partial derivative is taken with respect to the longitudinal coordinate z . The non-linear interaction is described using the wavelength dependent parameter $\kappa(\lambda)$ which is defined by

$$\kappa(\lambda) = \frac{2\pi d_{\text{eff}}}{n\lambda}. \quad (3.4)$$

Here, n is the index of refraction, λ the wavelength and d_{eff} is the effective non-linearity as described in Section 2.6. The complex function $f(z)$ includes the phase mismatch as well as the correction for Gaussian beams and is given by the equation

$$f(z) = \frac{e^{-\iota\Delta kz}}{1 - \iota \frac{z-z_0}{z_R}}, \quad (3.5)$$

where z_0 is the beam waist position and z_R is the Rayleigh range of either one of the beams. It is assumed that all interacting beams have the same waist position and identical Rayleigh ranges. The latter statement holds whenever the following condition is fulfilled

$$\theta_{\text{div}}^2 = \left(\frac{\lambda}{\pi w_0} \right)^2 \ll 1, \quad (3.6)$$

where θ_{div} is the divergence angle of the Gaussian beam. As an example, a wavelength of $\lambda = 1064$ nm and a waist size of $w_0 = 1$ μm , the divergence angle amounts to $\theta_{\text{div}}^2 \approx 0.115$ which is still smaller than unity. This shows that for all practical purposes the assumption of equal Rayleigh ranges holds.

The wave vector mismatch $\Delta k = (k_s + k_i) - k_b$ combines the wave vectors of the interacting beams inside the non-linear material which are given by $k = 2\pi n/\lambda$. The set of differential equations also contains the amplitude absorption coefficients α for each mode.

As stated above, there is no analytical solution to this set of differential equations in the general case. Therefore these are numerically solved for each round-trip of the cavity modes, by considering the fields at the output of a tiny segment of width Δz . In this case the optical fields and the function $f(z)$ can be assumed to be constant

3. N.L.C.S. - The non-linear cavity simulator

over the length of the segment and the equations can be approximated to

$$A_s(z + \Delta z) = A_s(z) - \Delta z \left(\iota\kappa(\lambda_s)f(z)A_i(z)^*A_b(z) + \frac{\alpha_s}{2}A_s(z) \right), \quad (3.7)$$

$$A_i(z + \Delta z) = A_i(z) - \Delta z \left(\iota\kappa(\lambda_i)f(z)A_s(z)^*A_b(z) + \frac{\alpha_i}{2}A_i(z) \right), \quad (3.8)$$

$$A_b(z + \Delta z) = A_b(z) - \Delta z \left(\iota\kappa(\lambda_b)f^*(z)A_s(z)A_i(z) + \frac{\alpha_b}{2}A_b(z) \right). \quad (3.9)$$

These equations are iteratively applied to the input fields until the end of the non-linear material has been reached as also explained in [25]. The output power for mode m is then given by the relation

$$P_m^{\text{out}} = \frac{\epsilon_0 c \pi W_0^2}{4} |A_m|^2, \quad (3.10)$$

where c is the speed of light and ϵ_0 the vacuum permittivity.

3.3. Calculation of the quantum fluctuations

3.3.1. The matrix formalism

In contrast to the calculation of the classical fields, which rely on a non-linear set of equations, the quantum mechanical fluctuations can be determined by linearizing the equations. This makes it possible to use a matrix formalism. The matrices that are needed consist of the reflection and transmission at a mirror, the propagation in free space and the non-linear interaction of the fields inside the crystal. The determination of the latter matrix can be done by writing the annihilation operator as $\hat{a} = A + \delta\hat{a}$, where A is the mean value which is given by the steady state solution as given in the previous Section and $\delta\hat{a}$ are the quantum fluctuations around this mean value. If we now insert this expression into the set of equations 3.3 considering only terms that are linear in the quantum fluctuations, we end up with the following set of equations

$$\partial_z \delta\hat{a}_s = -\iota\kappa(\lambda_s)f(z)(A_i^* \delta\hat{b} + A_b \delta\hat{a}_i^\dagger), \quad (3.11)$$

$$\partial_z \delta\hat{a}_i = -\iota\kappa(\lambda_i)f(z)(A_s^* \delta\hat{b} + A_b \delta\hat{a}_s^\dagger), \quad (3.12)$$

$$\partial_z \delta\hat{b} = -\iota\kappa(\lambda_b)f^*(z)(A_s \delta\hat{a}_i + A_i \delta\hat{a}_s). \quad (3.13)$$

Note that the absorption was neglected within these equations for the fluctuations, since they can not be coherently subtracted from a quantum field. Instead, the absorption has to be represented by vacuum fields that couple into the two additional mirrors V_1 and V_2 .

Since the above equations are now linear, we can define a matrix that acts on the state vector

$$\delta s = (\delta\hat{a}_s, \delta\hat{a}_s^\dagger, \delta\hat{a}_i, \delta\hat{a}_i^\dagger, \delta\hat{b}, \delta\hat{b}^\dagger)^T. \quad (3.14)$$

3.3. Calculation of the quantum fluctuations

For a small propagation Δz all the fields and the function $f(z)$ in the above equations can again be assumed to be constant and therefore the matrix for this transformation reads

$$\Delta\chi = \begin{pmatrix} 1 & 0 & 0 & \bar{\xi}_s A_b & \bar{\xi}_s A_i^* & 0 \\ 0 & 1 & \bar{\xi}_s^* A_b^* & 0 & 0 & \bar{\xi}_s^* A_i \\ 0 & \bar{\xi}_i A_b & 1 & 0 & \bar{\xi}_i A_s^* & 0 \\ \bar{\xi}_i^* A_b^* & 0 & 0 & 1 & 0 & \bar{\xi}_i^* A_s \\ -\bar{\xi}_b^* A_i & 0 & -\bar{\xi}_b^* A_s & 0 & 1 & 0 \\ 0 & -\bar{\xi}_b A_i^* & 0 & -\bar{\xi}_b A_s^* & 0 & 1 \end{pmatrix}, \quad (3.15)$$

where the function $\bar{\xi}_m$ for the mode m has been defined as

$$\bar{\xi}_m = -\iota\kappa_m(\lambda_m)f(z)\Delta z. \quad (3.16)$$

The single-pass interaction can now be described by a multiplication of these matrices each describing the propagation through a single segment of the non-linear crystal. The total matrix for the non-linear interaction on a length L can therefore be written as

$$\chi = \prod_{n=0}^{L/\Delta z} \Delta\chi(n\Delta z), \quad (3.17)$$

where $L/\Delta z$ is the number of crystal segments. This procedure to divide the medium into small sections is equivalent to the calculation of the classical fields in Section 3.2. The output state δs_{out} after passing the non-linear medium can now simply be written as

$$\delta s_{\text{out}} = \chi \delta s_{\text{in}}. \quad (3.18)$$

The remaining matrices that act on the state vector δs to describe the other transformations are given by

$$R = \begin{pmatrix} r_s e^{\iota\phi_s} & 0 & 0 & 0 & 0 & 0 \\ 0 & r_s e^{-\iota\phi_s} & 0 & 0 & 0 & 0 \\ 0 & 0 & r_i e^{\iota\phi_i} & 0 & 0 & 0 \\ 0 & 0 & 0 & r_i e^{-\iota\phi_i} & 0 & 0 \\ 0 & 0 & 0 & 0 & r_b e^{\iota\phi_b} & 0 \\ 0 & 0 & 0 & 0 & 0 & r_b e^{-\iota\phi_b} \end{pmatrix}, \quad (3.19)$$

for the reflection off a mirror,

$$T = \begin{pmatrix} \iota t_s & 0 & 0 & 0 & 0 & 0 \\ 0 & -\iota t_s & 0 & 0 & 0 & 0 \\ 0 & 0 & \iota t_i & 0 & 0 & 0 \\ 0 & 0 & 0 & -\iota t_i & 0 & 0 \\ 0 & 0 & 0 & 0 & \iota t_b & 0 \\ 0 & 0 & 0 & 0 & 0 & -\iota t_b \end{pmatrix}, \quad (3.20)$$

3. N.L.C.S. - The non-linear cavity simulator

for the transmission through a mirror and

$$\delta = \begin{pmatrix} e^{i\delta_s} & 0 & 0 & 0 & 0 & 0 \\ 0 & e^{-i\delta_s} & 0 & 0 & 0 & 0 \\ 0 & 0 & e^{i\delta_i} & 0 & 0 & 0 \\ 0 & 0 & 0 & e^{-i\delta_i} & 0 & 0 \\ 0 & 0 & 0 & 0 & e^{i\delta_b} & 0 \\ 0 & 0 & 0 & 0 & 0 & e^{-i\delta_b} \end{pmatrix}, \quad (3.21)$$

for the free space propagation.

Here, r_m and t_m are the amplitude reflectivity and transmissivity, respectively, and an additional phase ϕ_m may be introduced during the reflection. The single-pass detuning δ_m of the cavity for mode m is given by

$$\delta_m = \delta_0 + 2\pi\omega/\text{FSR}, \quad (3.22)$$

where δ_0 is the detuning due to a change in the optical path length of the cavity, ω is the sideband frequency and FSR is the free spectral range of the resonator.

It is now possible to write the steady state condition for the intra-cavity state vectors c_1 and c_2 as

$$c_1 = T_1 \text{in}_1 + R_1 R_{v_1} \chi_2 \delta T_2 \text{in}_2 + R_1 c'_2 + R_1 T_{v_2} \text{vac}_2 + R_1 R_{v_1} \chi_2 \delta R_2 \delta T_{v_1} \text{vac}_1, \quad (3.23)$$

$$c_2 = T_2 \text{in}_2 + R_2 c'_1 + R_2 \delta R_{v_1} \chi_1 T_1 \text{in}_1 + R_2 \delta T_{v_1} \text{vac}_1 + R_2 \delta R_{v_1} \chi_1 R_1 T_{v_2} \text{vac}_2. \quad (3.24)$$

Using the relations

$$c'_1 = \delta R_{v_1} \chi_1 c_1, \quad (3.25)$$

$$c'_2 = R_{v_2} \chi_2 \delta c_2, \quad (3.26)$$

we end up with the expressions for the intra-cavity state vectors

$$c_1 = A(T_1 \text{in}_1 + R_1 R_{v_2} \chi_2 \delta T_2 \text{in}_2 + R_1 T_{v_2} \text{vac}_2 + R_1 R_{v_2} \chi_2 \delta R_2 \delta T_{v_1} \text{vac}_1), \quad (3.27)$$

$$c_2 = B(T_2 \text{in}_2 + R_2 \delta R_{v_1} \chi_1 T_1 \text{in}_1 + R_2 \delta T_{v_1} \text{vac}_1 + R_2 \delta R_{v_1} \chi_1 R_1 T_{v_2} \text{vac}_2). \quad (3.28)$$

The matrices A and B are given by

$$A = (1 - R_1 R_{v_2} \chi_2 \delta R_2 \delta R_{v_1} \chi_1)^{-1}, \quad (3.29)$$

$$B = (1 - R_2 \delta R_{v_1} \chi_1 R_1 R_{v_2} \chi_2 \delta)^{-1}. \quad (3.30)$$

3.3. Calculation of the quantum fluctuations

The state vectors of the output fields for the steady state are then given by

$$\text{out}_1 = R_1 \text{in}_1 + T_1 R_{v_2} \chi_2 \delta c_2 + T_1 T_{v_2} \text{vac}_2 \quad (3.31)$$

$$\text{out}_2 = R_2 \text{in}_2 + T_2 \delta R_{v_1} \chi_1 c_1 + T_2 \delta T_{v_1} \text{vac}_1 . \quad (3.32)$$

We are now able to define the transfer matrices T_{ik} for each propagation from an input port i to an output port k . The output ports are out_1 ($k = 1$) and out_2 ($k = 2$), whereas the input ports are in_1 , in_2 , vac_1 and vac_2 , labeled by $i = 1, 2, 3, 4$ respectively. Using this mapping the following eight transfer matrices are defined

$$T_{11} = R_1 + T_1 R_{v_2} \chi_2 \delta B R_2 \delta R_{v_1} \chi_1 T_1 , \quad (3.33)$$

$$T_{21} = T_1 R_{v_2} \chi_2 \delta B T_2 , \quad (3.34)$$

$$T_{31} = T_1 R_{v_2} \chi_2 \delta B R_2 \delta T_{v_1} , \quad (3.35)$$

$$T_{41} = T_1 R_{v_2} \chi_2 \delta B R_2 \delta R_{v_1} \chi_1 R_1 T_{v_2} + T_1 T_{v_2} , \quad (3.36)$$

$$T_{12} = T_2 \delta R_{v_1} \chi_1 A T_1 , \quad (3.37)$$

$$T_{22} = R_2 + T_2 \delta R_{v_1} \chi_1 A R_1 R_{v_2} \chi_2 \delta T_2 , \quad (3.38)$$

$$T_{32} = T_2 \delta R_{v_1} \chi_1 A R_1 R_{v_2} \chi_2 \delta R_2 \delta T_{v_1} + T_2 \delta T_{v_1} , \quad (3.39)$$

$$T_{42} = T_2 \delta R_{v_1} \chi_1 A R_1 T_{v_2} . \quad (3.40)$$

Since these transfer matrices were calculated using the equations for the electrical field, we still have to normalize them to be valid for the transformation of the annihilation and creation operators. The relation between the field strength E and the annihilation operator reads

$$E \propto \sqrt{\frac{h\nu}{w_0^2}} \hat{a} , \quad (3.41)$$

where h is the Heisenberg constant, ν the frequency of the light field and w_0 the waist size of the beam. From the equation

$$E_{\text{out}} = B \hat{a}_{\text{out}} = T B \hat{a}_{\text{in}} , \quad (3.42)$$

it follows that the transfer matrix T has to be changed to $B^{-1} T B$, where the matrix B is given by

$$B = \begin{pmatrix} 1 & 0 & 0 & 0 & 0 & 0 \\ 0 & 1 & 0 & 0 & 0 & 0 \\ 0 & 0 & x_i & 0 & 0 & 0 \\ 0 & 0 & 0 & x_i & 0 & 0 \\ 0 & 0 & 0 & 0 & x_b & 0 \\ 0 & 0 & 0 & 0 & 0 & x_b \end{pmatrix} . \quad (3.43)$$

3. N.L.C.S. - The non-linear cavity simulator

Here, the fields were normalized with respect to the signal mode. The quantity x_m for the idler and harmonic modes is given by

$$x_m = \frac{\lambda_s}{\lambda_m}. \quad (3.44)$$

For the degenerate case we get $x_i = 1$ and $x_b = 2$. Now, the vacuum level for all modes is one on a linear scale. Note that this normalization is only needed because of the non-linear medium that mixes the fields.

3.3.2. Implementation of optical loss

As stated before, the absorption losses can not be coherently subtracted from the quantum field fluctuations as it was possible for the mean value of the fields. Instead, the losses have to be included by considering a vacuum field that mixes with the quantum fields of the cavity modes. This vacuum field is uncorrelated to the other fields which implies that we can simply add up the variances of these fields.

Technically, all the intra-cavity losses are represented by the transmissivity of the two additional mirrors V_1 and V_2 that are shown in Figure 3.1. The amplitude reflectivity r_m of these mirrors for the mode m can be written as

$$r_m = e^{-l_m}, \quad (3.45)$$

where l_m is the overall absorption for a single-pass through the non-linear material. For the mirror V_2 the losses of nlc_2 have to be used, whereas mirror V_1 includes the losses of nlc_1 .

The external losses that are due to the quantum efficiency of the homodyne detector are considered by a transformation of the resulting covariance matrix. For a detection efficiency η , the covariance matrix reads

$$\gamma = \mathbb{1} + \eta(\gamma_0 - \mathbb{1}), \quad (3.46)$$

where γ_0 is the covariance matrix without external losses and $\mathbb{1}$ is the unity matrix.

3.3.3. Calculation of the covariance matrix

To calculate the covariance matrix of the output state δS_{out} , we start with the relation between the input i and output k

$$\delta S_{\text{out},k} = \sum_i T_{ik} \delta S_{\text{in},i}, \quad (3.47)$$

which is given by using the transfer matrices defined in the previous Section. The summation has to be done over all the input ports. Since the covariance matrix is

3.3. Calculation of the quantum fluctuations

defined by the second momenta of the quadrature operators and the state vector δs was defined by the annihilation and creation operators, we first have to introduce the state vector in the quadrature basis q . The most general definition of this quantity is given by

$$q = (\delta\hat{\chi}_s^{(\theta_s)}, \delta\hat{\chi}_s^{(\theta_s+\pi/2)}, \delta\hat{\chi}_i^{(\theta_i)}, \delta\hat{\chi}_i^{(\theta_i+\pi/2)}, \delta\hat{\chi}_b^{(\theta_b)}, \delta\hat{\chi}_b^{(\theta_b+\pi/2)}), \quad (3.48)$$

where θ_m is the quadrature angle for mode m . For each mode also the orthogonal quadrature has to be given in this state vector. If all of the quadrature angles are zero, the quadrature state vector reduces to

$$q = (\delta\hat{\chi}_s^+, \delta\hat{\chi}_s^-, \delta\hat{\chi}_i^+, \delta\hat{\chi}_i^-, \delta\hat{\chi}_b^+, \delta\hat{\chi}_b^-), \quad (3.49)$$

where $\delta\hat{\chi}_m^+$ and $\delta\hat{\chi}_m^-$ are the amplitude and phase quadrature, respectively.

The transformation between δs and q can be written in a compact form by using the following matrix relation

$$q = \phi\delta s + (\phi\delta s)^\dagger = (\phi + \phi^* S)\delta s. \quad (3.50)$$

Here, the quadrature phase matrix ϕ and the matrix S are given by

$$\phi = \begin{pmatrix} e^{i\theta_s} & 0 & 0 & 0 & 0 & 0 \\ 0 & e^{i(\theta_s+\pi/2)} & 0 & 0 & 0 & 0 \\ 0 & 0 & e^{i\theta_i} & 0 & 0 & 0 \\ 0 & 0 & 0 & e^{i(\theta_i+\pi/2)} & 0 & 0 \\ 0 & 0 & 0 & 0 & e^{i\theta_b} & 0 \\ 0 & 0 & 0 & 0 & 0 & e^{i(\theta_b+\pi/2)} \end{pmatrix}, \quad (3.51)$$

$$S = \begin{pmatrix} 0 & 1 & 0 & 0 & 0 & 0 \\ 1 & 0 & 0 & 0 & 0 & 0 \\ 0 & 0 & 0 & 1 & 0 & 0 \\ 0 & 0 & 1 & 0 & 0 & 0 \\ 0 & 0 & 0 & 0 & 0 & 1 \\ 0 & 0 & 0 & 0 & 1 & 0 \end{pmatrix}. \quad (3.52)$$

The latter matrix is the first Pauli matrix and provides the identity

$$\delta s^\dagger = S\delta s, \quad (3.53)$$

which is the matrix representation of the hermitian conjugation.

We can now write the quadrature state vector of the output field depending on the state vector of the input field like

$$q_{\text{out},k} = (\phi + \phi^* S)\delta s_{\text{out},k} = (\phi + \phi^* S) \sum_i T_{ik} \delta s_{\text{in},i} = \sum_i \tilde{T}_{ik} \delta s_{\text{in},i}. \quad (3.54)$$

3. N.L.C.S. - The non-linear cavity simulator

Here, we again have to sum over all input ports i and we defined the matrix

$$\tilde{T}_{ik} = (\phi + \phi^* S) T_{ik}. \quad (3.55)$$

The elements of the covariance matrix γ for the output ports k and l at the sideband frequency ω in the notation we used so far is defined as

$$\gamma_{\alpha\beta}^{kl}(\omega) = \frac{1}{2} \langle (q_{\text{out},k}(\omega))_{\alpha} (q_{\text{out},l}(-\omega))_{\beta} + (q_{\text{out},k}(\omega))_{\beta} (q_{\text{out},l}(-\omega))_{\alpha} \rangle. \quad (3.56)$$

Here, the indices α and β range from one to six. For identical output ports $k = l$ the variances of the quadrature operators can be found on the main diagonal. All the other elements are the covariances of the quadrature operators. The negative frequency part shows up because of the two-photon formalism which describes the interaction of the upper and lower sideband correctly [21]. The sideband frequency is entering the calculation only within the matrix for the cavity detuning δ , since the optical field gains an additional phase of $2\pi\omega/\text{FSR}$ at the sideband frequency ω .

Since the second term of the above expression can be gathered by simply exchanging the indices α and β , it is sufficient to calculate only the first term which results in

$$\begin{aligned} M_{\alpha\beta}^{kl} &:= \langle (q_{\text{out},k}(\omega))_{\alpha} (q_{\text{out},l}(-\omega))_{\beta} \rangle \\ &= \langle \sum_{i,j} (\tilde{T}_{ik}(\omega) \delta s_{\text{in},i})_{\alpha} (\tilde{T}_{jl}(-\omega) \delta s_{\text{in},j})_{\beta} \rangle \\ &= \sum_{i,j} \langle \sum_n (\tilde{T}_{ik}(\omega))_{\alpha n} (\delta s_{\text{in},i})_n \sum_m (\tilde{T}_{jl}(-\omega))_{\beta m} (\delta s_{\text{in},j})_m \rangle \\ &= \sum_{i,j,m,n} (\tilde{T}_{ik}(\omega))_{\alpha n} (\tilde{T}_{jl}(-\omega))_{\beta m} \underbrace{\langle (\delta s_{\text{in},i})_n (\delta s_{\text{in},j})_m \rangle}_{(\gamma'_{ij})_{nm}} \\ &= \sum_{i,j,m} (\tilde{T}_{ik}(\omega) \gamma'_{ij})_{\alpha m} (\tilde{T}_{jl}(-\omega))_{\beta m} \\ &= \sum_{i,j} (\tilde{T}_{ik}(\omega) \gamma'_{ij} (\tilde{T}_{jl}(-\omega))^T)_{\alpha\beta}, \end{aligned} \quad (3.57)$$

where we have used the following expression for the elements of the product of two matrices A and B

$$(AB)_{nm} = \sum_j A_{mj} B_{jn}. \quad (3.58)$$

The matrix γ' includes the correlations of the input fields. For simplicity the fields for different input ports and modes are assumed to be uncorrelated. In this case the sub-matrix γ'_m for each mode m is given by

$$\gamma'_m = \begin{pmatrix} \langle \delta \hat{a}_m^2 \rangle & \langle \delta \hat{a}_m \delta \hat{a}_m^\dagger \rangle \\ \langle \delta \hat{a}_m^\dagger \delta \hat{a}_m \rangle & \langle (\delta \hat{a}_m^\dagger)^2 \rangle \end{pmatrix}, \quad (3.59)$$

3.3. Calculation of the quantum fluctuations

and the total matrix γ' reads

$$\gamma'_{ij} = \delta_{ij} \begin{pmatrix} \gamma'_s & 0 & 0 \\ 0 & \gamma'_i & 0 \\ 0 & 0 & \gamma'_b \end{pmatrix}, \quad (3.60)$$

where δ_{ij} is the Kronecker delta.

We can now further relate the matrix γ' to the covariance matrix γ of the input state. By inserting the quadrature representation of the annihilation and creation operators into the expression for γ'_m , we end up with the following expressions for the elements of the matrix γ'_m

$$\langle \delta \hat{a}^2 \rangle = \frac{1}{4} \langle (\hat{X}_1 + \iota \hat{X}_2)^2 \rangle = \frac{1}{4} (V_{11} - V_{22} + 2\iota V_{12}), \quad (3.61)$$

$$\langle (\delta \hat{a}^\dagger)^2 \rangle = \frac{1}{4} \langle (\hat{X}_1 - \iota \hat{X}_2)^2 \rangle = \frac{1}{4} (V_{11} - V_{22} - 2\iota V_{12}), \quad (3.62)$$

$$\begin{aligned} \langle \delta \hat{a} \delta \hat{a}^\dagger \rangle &= \frac{1}{4} \langle (\hat{X}_1 + \iota \hat{X}_2)(\hat{X}_1 - \iota \hat{X}_2) \rangle = \frac{1}{4} (V_{11} + V_{22} - \iota [\hat{X}_1, \hat{X}_2]) \\ &= \frac{1}{4} (V_{11} + V_{22} + 2), \end{aligned} \quad (3.63)$$

$$\begin{aligned} \langle \delta \hat{a}^\dagger \delta \hat{a} \rangle &= \frac{1}{4} \langle (\hat{X}_1 - \iota \hat{X}_2)(\hat{X}_1 + \iota \hat{X}_2) \rangle = \frac{1}{4} (V_{11} + V_{22} + \iota [\hat{X}_1, \hat{X}_2]) \\ &= \frac{1}{4} (V_{11} + V_{22} - 2). \end{aligned} \quad (3.64)$$

Here, we used the commutator relation $[\hat{X}_1, \hat{X}_2] = 2\iota$ and the covariance matrix in the form

$$\gamma = \begin{pmatrix} \langle \hat{X}_1^2 \rangle & \frac{1}{2} \langle \hat{X}_1 \hat{X}_2 + \hat{X}_2 \hat{X}_1 \rangle \\ \frac{1}{2} \langle \hat{X}_1 \hat{X}_2 + \hat{X}_2 \hat{X}_1 \rangle & \langle \hat{X}_2^2 \rangle \end{pmatrix} = \begin{pmatrix} V_{11} & V_{12} \\ V_{12} & V_{22} \end{pmatrix}. \quad (3.65)$$

Here, the quadrature operators \hat{X}_1 and \hat{X}_2 are the amplitude and phase quadratures, respectively.

Since the relation is linear, a compact notation of this transformation is given by the matrix relation

$$\gamma' = \frac{1}{4} (M^T \gamma M + K), \quad (3.66)$$

where the matrices M and K are given by

$$M = \begin{pmatrix} 1 & 1 \\ -\iota & \iota \end{pmatrix}, \quad K = \begin{pmatrix} 0 & 2 \\ -2 & 0 \end{pmatrix}. \quad (3.67)$$

To summarize the result of this Section, the complete covariance matrix of the output state for a resonator including a non-linear medium was derived analytically

3. N.L.C.S. - The non-linear cavity simulator

for an arbitrary sideband frequency. It was assumed that the input fields are uncorrelated but an arbitrary covariance matrix for each input mode can be specified. The covariance matrix of the total output state reads

$$\gamma_{\text{out}}(\omega) = \begin{pmatrix} \gamma^{11} & \gamma^{12} \\ \gamma^{12} & \gamma^{22} \end{pmatrix}. \quad (3.68)$$

The indices denote the port in reflection (1) and transmission (2). It was shown that the elements of the covariance matrix for the output ports k and l is given by the matrix relation

$$\gamma_{\alpha\beta}^{kl}(\omega) = \frac{1}{2} \left(M_{\alpha\beta}^{kl} + M_{\beta\alpha}^{kl} \right), \quad (3.69)$$

where the matrix $M_{\alpha\beta}^{kl}$ is defined by

$$M_{\alpha\beta}^{kl}(\omega) = \frac{1}{4} \sum_i \left((\phi + \phi^* S) T_{ik}(\omega) (M^T \gamma_i M + K) T_{il}^T(-\omega) (\phi + \phi^* S) \right)_{\alpha\beta}. \quad (3.70)$$

Here, γ_i is the covariance matrix for the input field i and the matrices S , M and K are the constant matrices that were derived further above. Note that this relation is a general expression for the transformation of a covariance matrix as long as the transfer matrices are known for the state vector in the basis of annihilation and creation operators. The matrix ϕ essentially corresponds to the homodyne detection scheme, allowing for measuring an arbitrary quadrature of the field. To get the squeezing and the entanglement of the fields we can use the methods that were introduced in Section 2.5.

3.4. The usage of N.L.C.S.

This Section describes the usage of the numerical simulation. It is written in plain C and parses a simple configuration file that the user has to write. The results are written to a file and an additional *Gnuplot* file is created that is used to plot the data. The latest usage information can be viewed by calling N.L.C.S. with the *-h* option.

3.4.1. Running N.L.C.S. from the command line

N.L.C.S. is started from the command line by specifying the name of a single configuration file as the argument. This will invoke the simulation and once it is finished, the results are plotted as specified by the user within the configuration file. The general command line usage of the application looks like

```
nlcs [-aphdtoc] infile [outfile]
```

where *outfile* is the optional filename where the calculated data will be stored. If this filename is not given, the basename of *infile* extended by the suffix *.dat* will be used. The options have the following meaning

- c Invokes a run of the simulation based on the parameters in *infile*.
- p call *Gnuplot* to display the results.
- a This option tells N.L.C.S. to use an approximation rather than the numerical time-domain simulation.
- o Use the transmitted input power as the starting point for the calculation. The default is to use the field from the previous run which is much faster.
- d Print out debugging information.
- t Runs a test suite of several unit tests.
- h Shows a help text.

N.L.C.S. will write a file *columns.txt* into the working directory that contains a list of all the quantities that were calculated together with their column position in the output file. The commands for plotting the data are stored in a separate file which may be edited manually to change the plot style or plot quantities. The filename is the basename of *outfile* extended by the suffix *.gp*.

For each run all results are calculated which includes the output powers, squeezing strengths, all two-mode entanglement combinations, the purity and the parametric gain.

3.4.2. The input file format

N.L.C.S. uses the *libconfuse* [26] for parsing the input files. The benefits of this configuration file parsing library are well organized, easy to edit configuration files and a minimum of code for reading these files. Variables are assigned using a “name = value” style. Throughout the file it is possible to make comments like

```

\\ Everything after '\\ ' (C-style) is treated as a comment
# The same is true for the Shell-style comments after '#'
\* More than one line may be commented by using
 * the C-style syntax '\* ... *\'.
*\

```

The file is divided into sections (indicated by “Section name { }”). Because there are meaningful defaults for each value (e.g. perfect detection), it is not necessary to always specify all possible parameters in the configuration file. Some of the

3. *N.L.C.S. - The non-linear cavity simulator*

parameters can be defined for each mode separately. In these cases the format is “name = {value1, value2, value3}”. The order of the modes is always given as signal, harmonic and idler. It is possible to leave out modes, but you will have to leave the mode order intact. You can also skip whole sections. In Figure 3.2 the complete file format specifying the default values is shown.

3.4. The usage of N.L.C.S.

```
Laser {
    w0 = 24e-6 # fundamental waist radius
    omega = 1e6 # sideband frequency
5    lambda = {1064e-9, 532e-9, 1064e-9} # wavelength

    Port 1 { # same for Port 2
        P = {0, 1, 2} # input laser power
        phi = {0, 0, 0} # input phase
10    }}

    Cavity {
        FSR = 1e9 # free spectral range
        delta = {0, 0, 0} # detuning
        type = "bowtie"
15    nmax = 1000000 # maximum number of round-trips

        Mirror 1 { # same for Mirror 2
            R = {0, 0, 0} # power reflectivity
            phi = {0, 0, 0} # phase in reflection
20        }

        Crystal 1 { # same for Crystal 2
            z = 0.0 # position relative to the waist
            chi = 1e-12 # nonlinearity
25            L = 6.5e-3 # length
            n = 2.23 # index of refraction
            alpha = {0, 0, 0} # power absorption coefficient
            beta = {0, 0, 0} # nonlinear absorption coefficient
            dk = 0.0 # phase mismatch
30        }}

        Homo 1 { # same for Homo 2
            theta = {0, 0, 0} # detection angle
            eta = {1, 1, 1} # quantum efficiency
            optimize = true # lock homo to optimal squeezing
35            g = {1, 1, 1} # electrical gain
        }

        Control {
            step = 100 # X-axis resolution
            nseg = 500 # Number of crystal segments
40            eps = 1e-6 # Steady-state precision
            scan = "" # Which quantity should be scanned?
            x = "" # Plot quantity on the x axis
            y = "" # Plot quantity on the y axis
            PlotRange = {0, 1} # parameter range
45        }
    }
```

Figure 3.2.: Complete configuration file format for N.L.C.S. specifying the default values for each parameter.

3. N.L.C.S. - The non-linear cavity simulator

Scan parameter	
phase mismatch	The wave vector mismatch $\Delta kL/2$.
fundamental power	The fundamental input power for port 1.
harmonic power	The harmonic input power for port 1.
idler power	The idler input power for port 1.
homodyne angle	State tomography by scanning the homodyne angle.
frequency	Sideband frequency to generate a noise spectrum.
detuning	The cavity detuning given in metres.
y axis parameters	
power	Output power for each mode.
conversion efficiency	Output power normalized to the signal input power.
parametric gain	Amplification of the intra-cavity power.
squeezing	Squeezing for each mode of the output state.
squeezing angle	The angle of the optimal squeezing.
purity	Purity of the output states.
entanglement	The two-mode entanglement of the output modes.
finesse	The finesse of the cavity.
error	Deviation from linearized theory.

Table 3.1.: Parameters that can be used for the x and y axes within N.L.C.S..

Currently, the x axis is identical with the parameter that is to be scanned. If you want to plot another quantity on this axis (e.g. squeezing versus conversion efficiency), you will have to edit the *Gnuplot* file manually. Table 3.1 lists all parameters that are available as scan parameters and the parameters that can be plotted on the y axis.

Note that the *x*, *y* and *scan* parameters have to be given in double quotes and in lower case. The units are all SI units without any factorization except for the phases which are always given in units of π .

The code snippet in Figure 3.3 shows an example for the simulation of an SHG cavity, plotting the conversion efficiency over the phase mismatch. More examples can be found in the *examples* folder within the source distribution.

3.4. The usage of N.L.C.S.

```
# Second harmonic generation @1064nm using NLCS.

# use 200 mW of fundamental input power
Laser { Port 1 { P = {0.2} } }

Cavity {
  # singly resonant cavity
  Mirror 1 { R = {0.92} }

  # highly reflective coating
  Mirror 2 { R = {0.9997, 0.9997} }

  # use MgO:LiNbO3
  Crystal 1 {
    chi = 2.6e-12
    L = 6.5e-3
    n = 2.223
    alpha = {0.1, 0.1}
  }
}

# the plot range is appr. the 4. conversion minimum each
Plot {
  range = {-4.0, 4.0}
  scan = "phase mismatch"
  y = "conversion efficiency"
}
```

Figure 3.3.: N.L.C.S. configuration file for simulating a singly resonant SHG.

3.5. Modelling different regimes

This Section describes some examples of the numerical results that can be gained by using N.L.C.S.. All of the following plots have been produced by using either N.L.C.S. directly or by running batch scripts that provide more flexibility. For each plot the corresponding input file is given.

3.5.1. Non-linear materials without a cavity

A single-pass of the fundamental mode through a non-linear material can be simulated by using the following input file

```

Laser {
    gaussian = false
    w0 = 83.5e-6
5
    Port 1 { P = {0.1} }
}
Cavity {
    type = bowtie
10
    Crystal 1 {
        n = 2.2
        L = 0.1
        chi = 5e-12
    }}
15 Plot {
    step = 200
    scan = "phase mismatch"
    y = "conversion efficiency"
    range = {-4.0, 4.0}
20 }

```

This file describes a plane wave of 100 mW power propagating through a non-linear material of length $L = 10$ cm. The *Cavity* section has to be used to specify the non-linear material. Note that per default all mirror reflectivities are zero. For this very weak interaction one can solve the coupled set of non-linear equations with the following result for the conversion efficiency η

$$\eta(\Delta k) = \frac{P_{\text{harmonic}}}{P_{\text{fundamental}}} \propto \text{sinc}^2 \left(\frac{\Delta k L}{2} \right). \quad (3.71)$$

The numerical simulation for the above configuration file results exactly in this function and is shown by the red curve in Figure 3.4. The value for the waist size of $w_0 = 83.5 \mu\text{m}$ was chosen such that the field of the plane wave is equal to the mean field of a Gaussian beam with a waist size of $w_0 = 50 \mu\text{m}$ which is shown in green. For the latter beam the maximal conversion efficiency is shifted and a little bit lower

3.5. Modelling different regimes

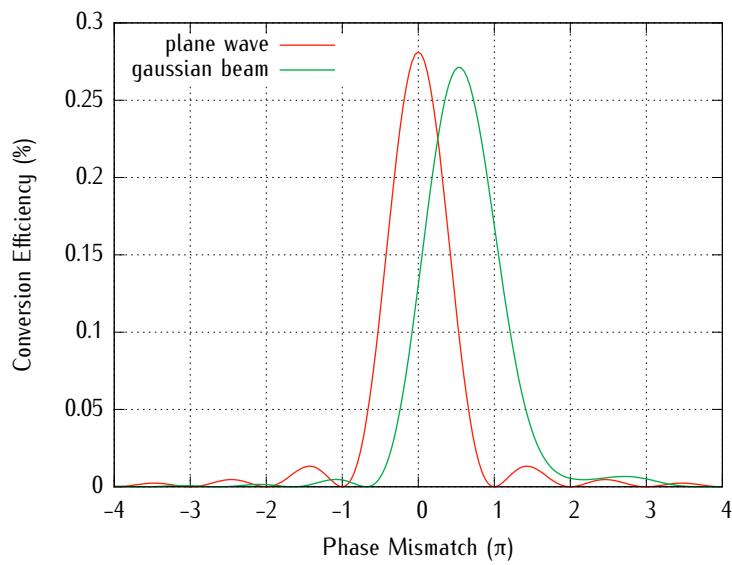


Figure 3.4.: Conversion efficiency for a single-pass through a non-linear medium depending on the phase mismatch. The plane wave considered here has the same mean field across the propagation length as the Gaussian beam. The change in position and height of the maximum is due to the Gouy phase.

3. N.L.C.S. - The non-linear cavity simulator

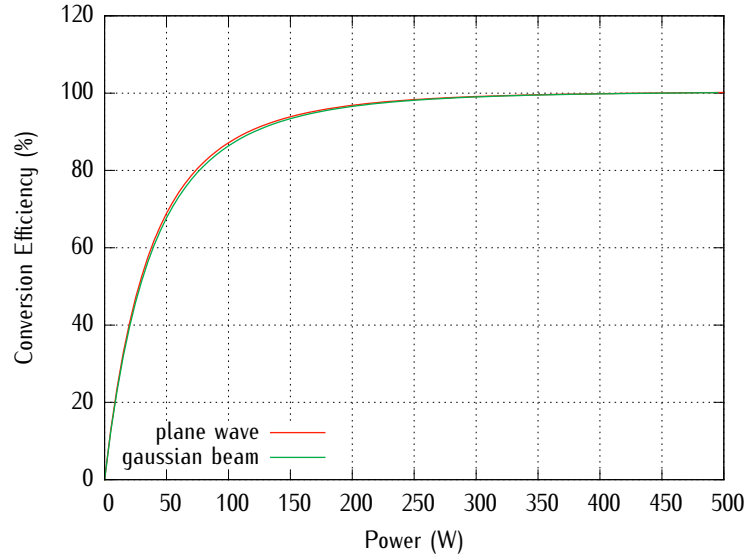


Figure 3.5.: Single-pass conversion efficiency depending on the fundamental pump power. In the case of plane waves perfect phase matching $\Delta k = 0$ was used. For Gaussian beams, however, the optimal phase mismatch depends on the incident power.

than for the plane wave. This is due to the fact that there is no perfect phase matching along the propagation length anymore (see Section 3.7).

Another analytical solution for plane waves in the case of perfect phase matching is shown in Figure 3.5. The only changes to the previous configuration file were the scan parameter and range. These are now given by

```
scan = "fundamental power"
range = {0.0, 1000.0}
```

The analytical function that describes the conversion efficiency in this case is given by

$$\eta(P) = P \cdot \tanh^2 \left(A\sqrt{P} \right), \quad (3.72)$$

where P is the input power of the fundamental mode and the factor A is given by

$$A = 2\kappa L \sqrt{\frac{2}{\epsilon_0 c \pi W_0^2}}. \quad (3.73)$$

This shows that the conversion efficiency asymptotically reaches a value of one, i.e. all the fundamental power can be converted to the second harmonic. Except for

3.5. Modelling different regimes

small deviations this is also true for the focused Gaussian beam, as it is shown by the green curve in Figure 3.5. However, in the latter case the optimal phase mismatch now depends on the input power and therefore has to be adjusted correctly. The reason for this is the following: For weak input powers of the fundamental field its degradation during the propagation can be neglected. Therefore, the conversion takes place inside the whole crystal only weighted by the intensity of the beam. As the pump power increases, the depletion of the fundamental must be taken into account, leading to another weighting factor for the non-linear interaction. The conversion gets stronger before the focus and due to the depletion it gets weaker behind it. Since the phase mismatch is due to the Gouy phase of the beam, the optimum phase mismatch will shift as well.

There are also cases where a non-linear material is not necessary for the simulation. N.L.C.S. can also be used to simulate the effect of losses to a squeezed state of light. The following configuration file uses a single cavity mirror to introduce losses to a squeezed input beam.

```

    Laser {
        Port 1 {
            Xp = {-3.0, -6.0, -10.0}
5         }
    }

    Homo 2 { optimize = true}

10 Plot {
    scan = "mirror reflectivity"
    y = "squeezing"
    range = {0.0, 1.0}
}
```

Here, three different squeezing levels are addressed to the input fields (signal, idler and harmonic) and all the mirror reflectivities are scanned in the range from zero to perfect reflectance. Figure 3.6 shows the degrading of the squeezing due to the losses.

Since a single mirror can be used as a beam splitter, it is also possible to entangle two squeezed states of light. Therefore, the configuration file that is shown in Figure 3.7 uses two equally squeezed input states for the fundamental mode and a single squeezed state for the harmonic mode to investigate the generation of *s-class* and *v-class* entangled states of light, respectively [27]. These states of light are produced by interfering a squeezed state with either a vacuum state (*v-class*) or with another squeezed state (*s-class*) on a beamsplitter. Note that the *s-class* entanglement requires the orthogonal orientation of the squeezing ellipses which is achieved by the squeezing angle $\theta = 0.5\pi$ for one of the fundamental input modes. The mirror mimics a 50/50 beamsplitter and the homodyne angle is scanned. The entanglement

3. N.L.C.S. - The non-linear cavity simulator

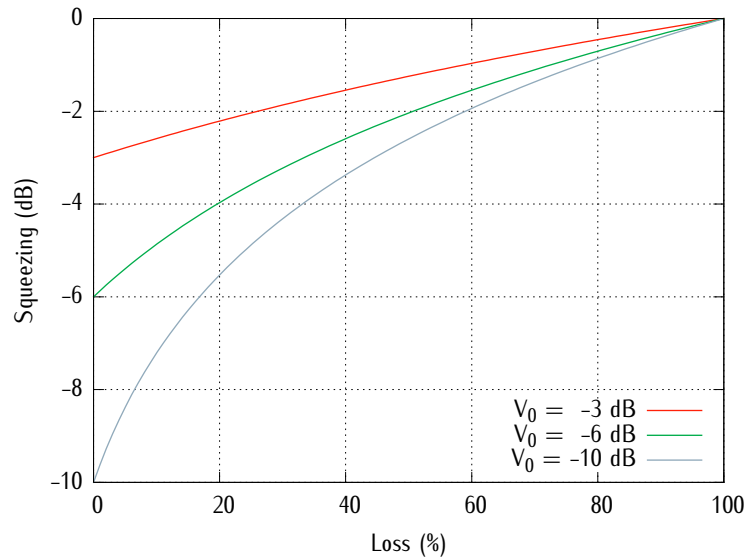


Figure 3.6.: Influence of losses to a squeezed state.

```

Laser {
  Port 1 { Xp = {-3.0, -3.0}}
  Port 2 {
5     Xp = {-3.0}
      theta = {0.5}
  }
}

10 Cavity { Mirror 1 { R = {0.5, 0.5}}}

Plot {
  scan = "homodyne angle"
  y = "entanglement"
15  range = {0, 2}
}

```

Figure 3.7.: N.L.C.S. configuration file for simulating the entanglement at a beamsplitter.

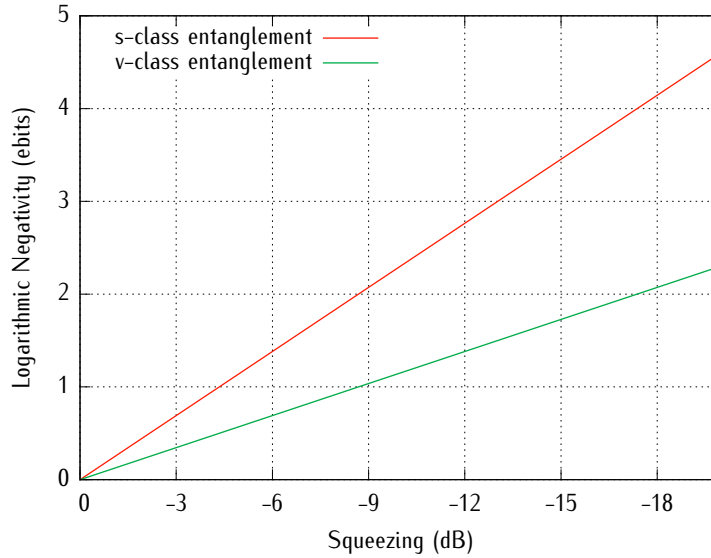


Figure 3.8.: Entanglement at a beam splitter. To generate *v-class* entanglement a squeezed state interferes with a vacuum state at the beam splitter whereas *s-class* entanglement is created by orthogonally overlapping two squeezed states with the same amount of squeezing.

is a property of the state and of course does not depend on the homodyne angle, but since N.L.C.S. does not support to scan the squeezing of the input state directly, a *Python* script was used to repeatedly run N.L.C.S. with an alternating configuration file and to parse the entanglement from the results (see Appendix A.7). Figure 3.8 shows the resulting entanglement at a beam splitter for the *v-class* and *s-class*. For the *v-class* entanglement a squeezing level of -9 dB leads to a logarithmic negativity of $E_N \approx 1$. The *s-class* entanglement is exactly twice the *v-class* entanglement. Since this measure is linear on the logarithmic squeezing scale, the entanglement at a beam splitter provides a useful rule of thumb when comparing the entanglement strength in other scenarios.

3.5.2. Resonators without non-linear materials

As long as radiation pressure noise can be neglected, an empty cavity can not be used to produce squeezing itself, but it can be utilized to generate frequency dependent squeezed states of light. These states are necessary for improving gravitational wave detectors like GEO 600 over the whole detection band [28]. For low frequencies the radiation pressure noise has to be reduced in order to improve the sensitivity, whereas for high frequencies the laser power has to be raised in order to reduce the

3. N.L.C.S. - The non-linear cavity simulator

shot noise. This means that the amplitude quadrature has to be squeezed in the low frequency range whereas it has to be anti-squeezed for the high frequency part of the detection band. This is achieved by reflecting a squeezed state off a detuned filter cavity with the effect that the squeezing ellipse will show a frequency dependent rotation in phase space. The configuration file for simulating this scenario with N.L.C.S. reads

```
Laser {
    lambda = {1064e-9, 1064e-9, 1064e-9}

5    Port 1 {
        P = {70e-6, 70e-6, 70e-6}
        Xp = {-3.0, -3.0, -3.0}
    }
}

10 Cavity {
    delta = {26.866e-9, 26.866e-9, 26.866e-9}
    FSR = 3e8

15    Mirror 1 { R = {0.97, 0.97, 0.97}}
    Mirror 2 { R = {1.0, 1.0, 1.0}}
}

    Homo 1 { theta = {0.0, 0.25, 0.5}}

20 Plot {
    scan = "frequency"
    y = "squeezing"
    range = {12e6, 18e6}

25 }
```

Figure 3.9 shows the reflection of a -3 dB squeezed state at a filter cavity. The carrier was detuned to about 15 MHz and the frequency dependent squeezing for three different homodyne angles is shown. The values were taken from the paper by Chelkowski et al. [29].

3.5.3. Squeezing in second harmonic generation

Single ended resonators containing a phase matched non-linear crystal are routinely used to produce the second harmonic of an optical field. The conversion efficiency of such a second harmonic generator (SHG) depending on the fundamental pump power is shown in Figure 3.10. The maximum of this curve is due to the impedance matching of the resonator. Without the conversion, the resonator is overcoupled and due to the conversion loss on the fundamental mode it becomes impedance matched. At this point the complete input power enters the cavity and therefore

3.5. Modelling different regimes

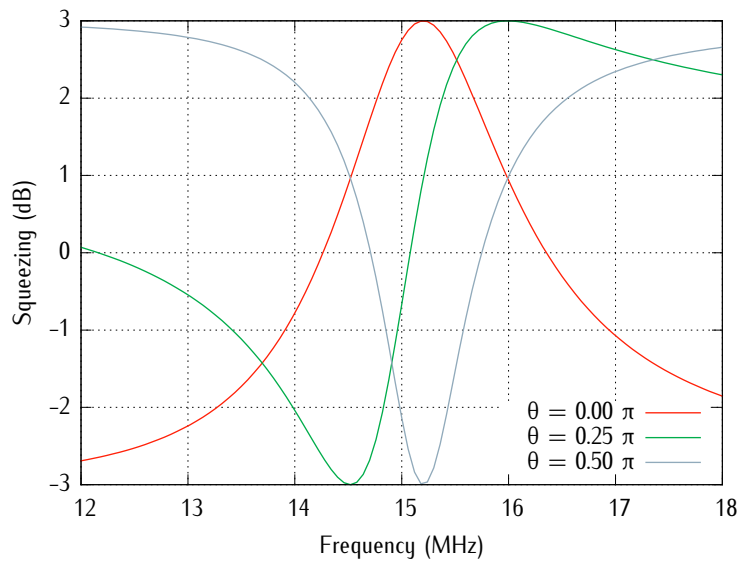


Figure 3.9.: Squeezing in reflection of a detuned filter cavity. The input state was amplitude squeezed to -3 dB and the detuning of the cavity was approximately 15 MHz. The curves show the variance of the amplitude quadrature ($\theta = 0$), the phase quadrature ($\theta = 0.5\pi$) and the quadrature at $\theta = 0.25\pi$.

3. N.L.C.S. - The non-linear cavity simulator

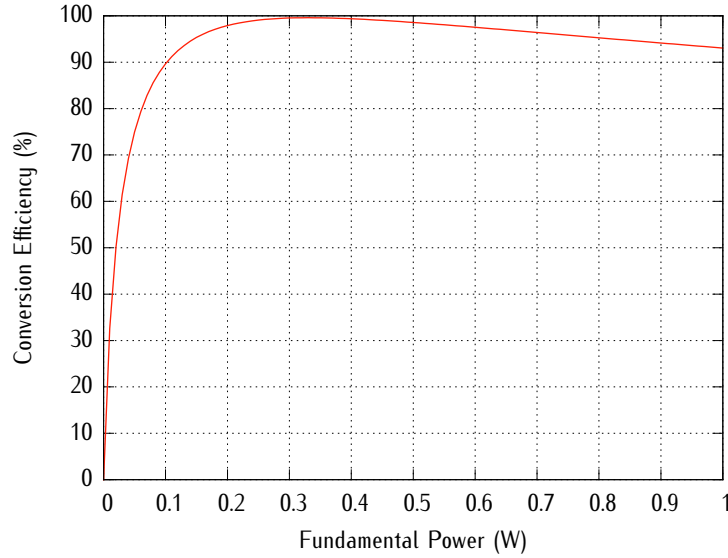


Figure 3.10.: Conversion efficiency from a second harmonic generator depending on the fundamental pump power. The maximum conversion efficiency occurs when the resonator is impedance matched.

perfect conversion can be achieved. For even higher input powers, the single-pass interaction leads to higher losses and thus the resonator becomes undercoupled with the effect that the conversion efficiency decreases.

In Figure 3.11 the corresponding amplitude squeezing for both, the fundamental and harmonic mode, is plotted against the conversion efficiency. This plot has been generated by scanning the fundamental input power. Whereas only a maximum amount of -1.76 dB ($2/3$ in variance) of fundamental squeezing can be achieved, the squeezing of the harmonic mode grows further for increasing input powers. This result was also confirmed by Maeda and Kikuchi [30]. Note that the harmonic mode is squeezed by -3 dB when the cavity is impedance matched. This corresponds to the single-pass interaction, where it was shown [31] that the squeezing of the harmonic mode asymptotically reaches -3 dB as the conversion efficiency goes to 100 %.

The corresponding entanglement of the harmonic and fundamental field is shown in Figure 3.12. At perfect conversion the entanglement amounts to $E_N = 2/3$ which corresponds to an *s-class* entanglement using -3 dB squeezed states. The maximum entanglement occurs at higher input powers than for the impedance matched case.

3.5. Modelling different regimes

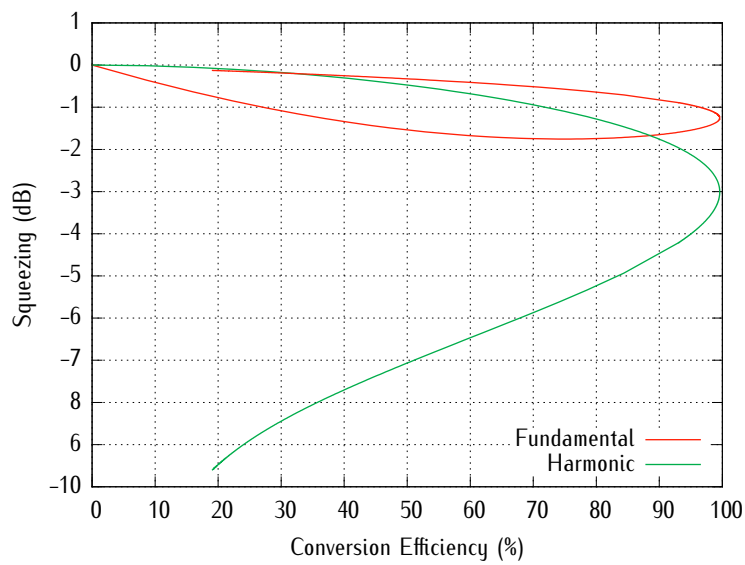


Figure 3.11.: Squeezing as produced by a second harmonic generator depending on the conversion efficiency. At perfect conversion the second harmonic mode is squeezed by -3 dB. The plot was generated by scanning the fundamental input power.

3. N.L.C.S. - The non-linear cavity simulator

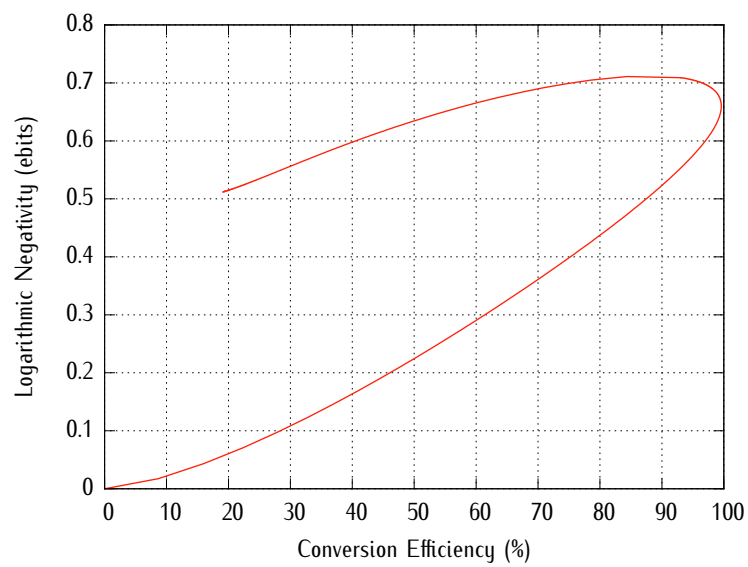


Figure 3.12.: Entanglement of the fundamental and harmonic mode depending on the conversion efficiency of an SHG. The maximum amount is reached slightly after the point of perfect conversion. The plot was generated by scanning the fundamental input power.

```

Laser {
    gaussian = false
    w0 = 25e-6
5
    Port 1 { P = {0.0, 0.1}}
}

Cavity {
10
    Mirror 1 { R = {0.92}}

    Mirror 2 { R = {1.0, 1.0}}

    Crystal 1 {
15
        n = 2.2
        L = 6.5e-3
        chi = 6e-12
    }
}

20
Homo 1 { theta = {0.5, 0.5}}

Plot {
25
    scan = "harmonic power"
    y = "squeezing"
    range = {0.0, 0.5}
}

```

Figure 3.13.: N.L.C.S. configuration file for simulating an OPO.

3.5.4. Optical parametric oscillation below and above threshold

The description of an optical parametric oscillator (OPO) in this Section is performed by using the configuration file shown in Figure 3.13. which describes a single-ended resonator for the fundamental mode where the harmonic pump field is double-passing the non-linear material. The pump power is scanned within a range of approximately two times the threshold power which amounts to $P_{\text{th}} \approx 225 \text{ mW}$ in this case. The homodyne detector looks at the phase quadrature of each mode which is also the quadrature where the highest noise suppression occurs.

For OPO below its threshold the set of non-linear equations decouples and an analytical expression for the variance of the amplitude (V^+) and phase (V^-) quadratures depending only on the ratio $x = \sqrt{P/P_{\text{th}}}$ can be given. Here, P is the power of the harmonic input field and P_{th} is the threshold power above which a bright

3. N.L.C.S. - The non-linear cavity simulator

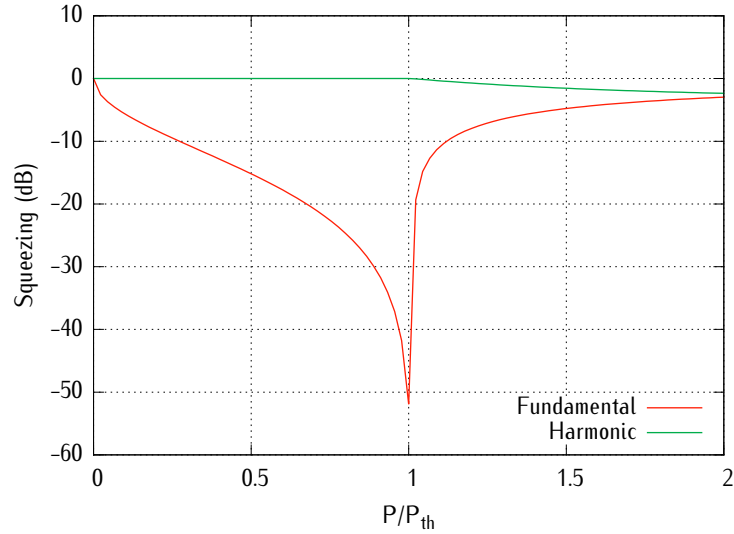


Figure 3.14.: Squeezing of the phase quadrature from an OPO cavity. Below the threshold only the fundamental mode gets squeezed, whereas both modes are squeezed above threshold. The limited amount of squeezing is due to the resolution of the x axis.

fundamental field is produced. The solution is given by [32]

$$V^- = 1 - \frac{4x}{(1+x)^2}, \quad V^+ = \frac{1}{V^-}. \quad (3.74)$$

Figure 3.14 shows the variance of the phase quadrature for the fundamental and harmonic field depending on the pump power. Below the threshold only the fundamental mode is squeezed, whereas above threshold the harmonic mode gets squeezed as well in phase and the variance of the fundamental raises again. Whereas both modes are pure states below the oscillation threshold, the purity suddenly drops as soon as the threshold has been reached and thereafter returning to a pure state again. The entanglement reveals that both modes are correlated above threshold. This behavior is depicted in Figure 3.15, where the purity is plotted on the left and the entanglement between the fundamental and harmonic mode on the right axis.

3.5.5. Kerr squeezing

Although N.L.C.S. is based on a second order non-linear interaction, it can also be used to study the Kerr-effect by using the method of cascaded non-linearities as suggested in [33]. By tuning the phase mismatch it is possible to generate an effective

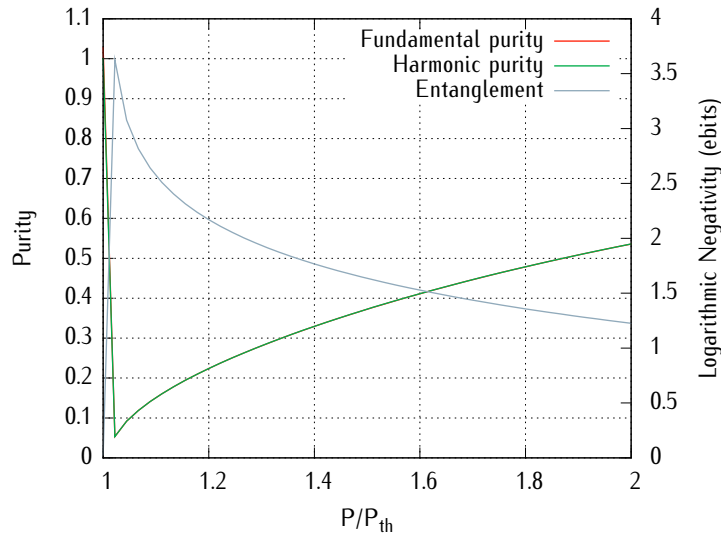


Figure 3.15.: The purity (left axis) and entanglement (right axis) of the output modes from an OPO cavity above threshold. Below threshold the set of equations decouples and therefore no entanglement can be observed.

third order non-linearity which causes an optical Kerr-effect, i.e. an intensity dependent phase shift of the fundamental mode. An approximate treatment of this effect can be found in [25]. To simulate the squeezing spectrum from a Kerr non-linear cavity using N.L.C.S. requires the following steps

1. Tune the temperature to the first conversion minimum.
2. Adjust the cavity detuning to the operating point.
3. Plot the squeezing spectrum.

The intensity dependent phase of the fundamental mode is visible whenever the phase mismatch is not perfect. However, unless the conversion efficiency is not minimal, the fundamental mode will gain losses that will degrade the squeezing. Therefore, the phase mismatch has to be tuned to the first conversion minimum in order to achieve the strongest effective third order non-linearity. Because of the waist size dependence of the conversion minima (see Section 3.5.1) the first thing is to plot the conversion efficiency against the phase mismatch unless plane waves are used in the simulation. The configuration file that is shown in Figure 3.16 was used to produce the curve in Figure 3.17. In this setup the mirrors have no reflectivity for the harmonic mode and therefore this field leaves the resonator symmetrically

3. N.L.C.S. - The non-linear cavity simulator

```
Laser {  
    w0 = 28e-6  
5    Port 1 { P = {0.7}}  
}  
  
Cavity {  
    type = linear  
10  
    Mirror 1 { R = {0.983}}  
    Mirror 2 { R = {0.999999}}  
  
    Crystal 1 {  
15        L = 6.5e-3  
        n = 2.223  
        chi = 2.4e-12  
    }  
}  
20  
Plot {  
    scan = "phase mismatch"  
    y = "conversion efficiency"  
    range = {-3, 3}  
25 }
```

Figure 3.16.: N.L.C.S. configuration file for simulating a Kerr non-linear cavity.

3.5. Modelling different regimes

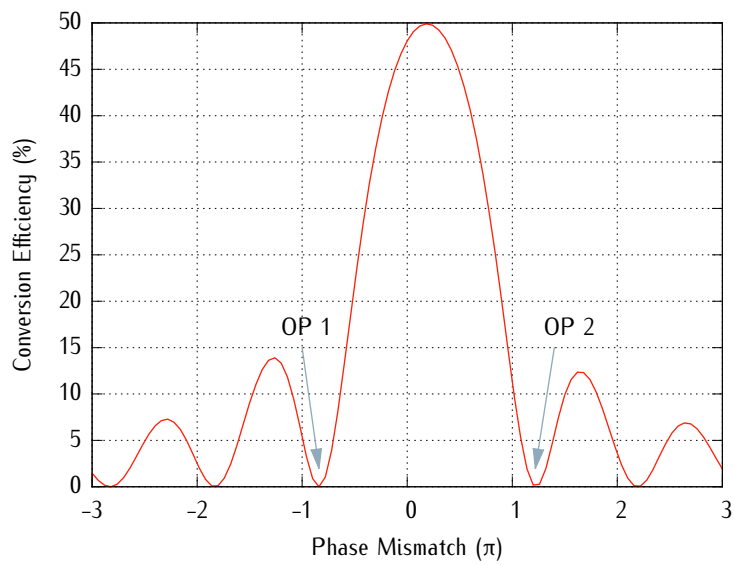


Figure 3.17.: Operating points (OP) for achieving the biggest cascaded non-linearity. Unless plane waves are used, the operating points depend on the waist size of the fundamental mode and hence differ from the plane wave value of $\pm\pi$.

3. N.L.C.S. - The non-linear cavity simulator

to both output ports. This was chosen to simplify the interaction, since a double-pass for the harmonic mode would lead to an interference effect that is discussed in Section 3.7.

After the phase mismatch has been tuned to either one of the operating points OP 1 or OP 2, the resonator has to be scanned to produce an Airy peak. Therefore the configuration file is changed to include the following lines for the phase mismatch

```
Crystal 1 {  
    dk = -0.82 # (OP 1)  
    #dk = 1.22 # (OP 2)  
}
```

and the new plot options

```
Plot {  
    scan = "detuning"  
    y = "power"  
    range = {-2e-9, 2e-9}  
}
```

The peaks of the fundamental mode that is produced in transmission of the resonator for both operating points are shown in Figure 3.18. The Airy peaks of a Kerr non-linear cavity are flipped when changing the operating point but still scanning the resonator in the same direction, which is characteristic for this effect. This is due to the sign change of the phase mismatch which effectively shortens or lengthens the optical path for the fundamental mode. The squeezing of the fundamental mode in reflection of the scanned resonator is depicted in Figure 3.19. The homodyne detector was operated to always find the maximal squeezing by specifying

```
Homo 1 { optimize = true}
```

in the configuration file. The effect of this argument is that a principal axis transformation of the squeezing ellipse in phase space is performed, resulting in the minimal variance of the quantum state as well as the quadrature angle under which this optimal squeezing occurs. The maximal squeezing is produced for the steepest slope of the Airy peak. In this case the amplitude quadrature of the fundamental mode is squeezed.

Finally, the squeezing spectra for the amplitude quadrature of the fundamental mode and different detunings are shown in Figure 3.20. In order to produce the spectrum the configuration file was extended to include the cavities free spectral range

```
Cavity {  
    FSR = 2.455e9  
}
```

3.5. Modelling different regimes

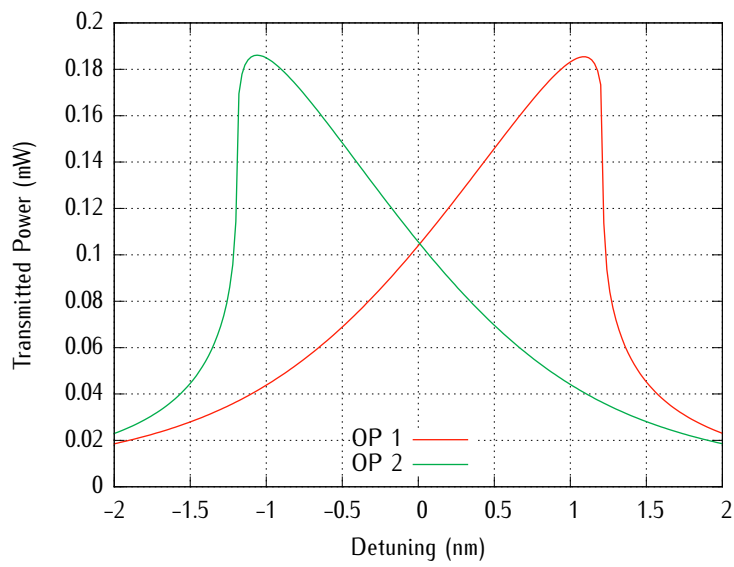


Figure 3.18.: Deformed Airy peaks from a Kerr resonator. The operating points correspond to the negative phase mismatch (OP 1) and the positive phase mismatch (OP 2). The mirrored peaks at the two operating points are characteristic for an optical Kerr non-linearity.

3. N.L.C.S. - The non-linear cavity simulator

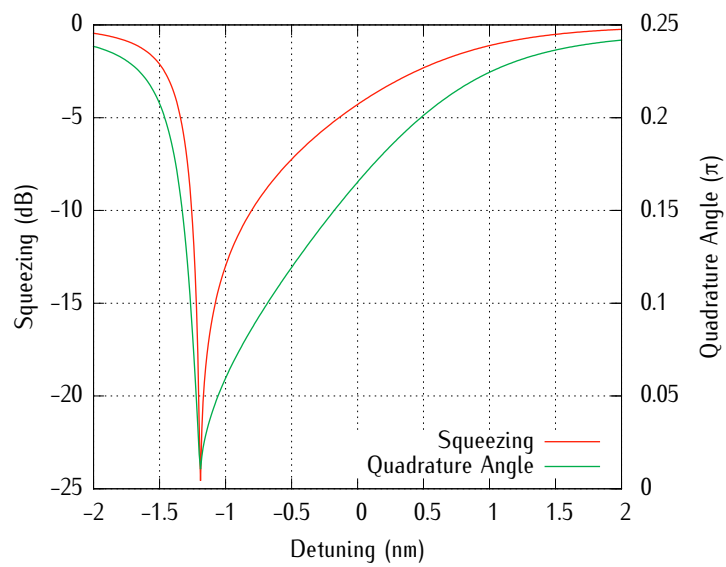


Figure 3.19.: Squeezing of the fundamental mode in reflection of a Kerr non-linear resonator depending on the resonator detuning. The plot shows the optimally squeezed quadrature together with its angle. For the steepest slope of the Airy peak the amplitude quadrature is squeezed.

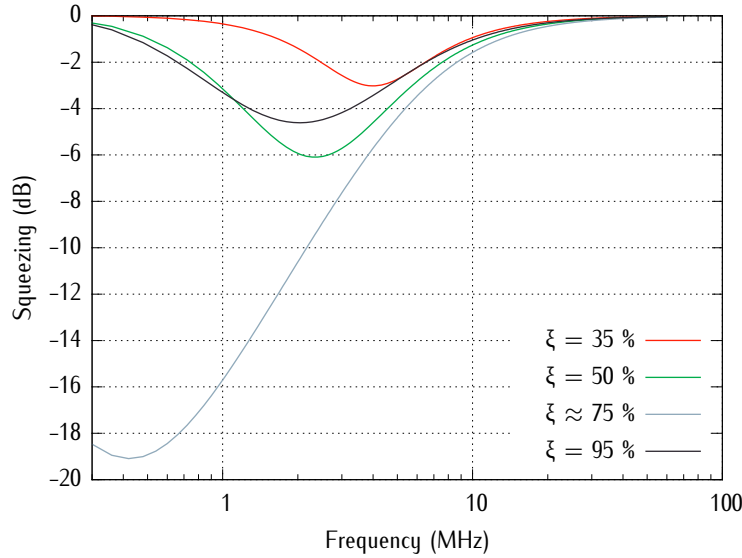


Figure 3.20.: Squeezing spectra of the amplitude quadrature from a Kerr cavity for different detunings. At the steepest slope of the Airy peak ($\xi = 75\%$) the maximum amount of squeezing is produced.

Here, all detunings correspond to the steeper slope of the Airy peak. The detuning $\xi = P_{\text{trans}}/P_{\text{max}}$ is given by the ratio between the transmitted power P_{trans} normalized to the maximal power P_{max} that is transmitted. This is useful since the steepest slope always belongs to a value of $\xi = 0.75$ (see Appendix B). For this value the strongest squeezing is achieved at DC while for other detunings the squeezing is weaker and occurs at different sideband frequencies.

3.6. Error estimation

As said before the coupled set of non-linear equations was linearized in order to calculate the quantum mechanical fluctuations by using the matrix formalism. To find out in which cases this assumption is valid, the terms that were neglected can now be calculated using the transfer matrices that were derived in Section 3.3.1. It is then necessary that these terms are small compared to the other terms in the equations.

The quantization is done by making the equations symmetric and then replacing each field by its annihilation or creation operator. Neglecting the absorption this

3. N.L.C.S. - The non-linear cavity simulator

procedure yields the following relations

$$\partial_z \hat{a}_s = -\iota\kappa(\lambda_s)f(z)\frac{1}{2}(\hat{a}_i^\dagger \hat{a}_b + \hat{a}_b \hat{a}_i^\dagger), \quad (3.75)$$

$$\partial_z \hat{a}_i = -\iota\kappa(\lambda_i)f(z)\frac{1}{2}(\hat{a}_s^\dagger \hat{a}_b + \hat{a}_b \hat{a}_s^\dagger), \quad (3.76)$$

$$\partial_z \hat{a}_b = -\iota\kappa(\lambda_b)f^*(z)\frac{1}{2}(\hat{a}_s \hat{a}_i + \hat{a}_i \hat{a}_s). \quad (3.77)$$

If we again split the fields into the mean value and the fluctuation and then take the expectation value of the above equations we end up with

$$\partial_z A_s = -\iota\kappa(\lambda_s)f(z)(A_i^* A_b + \frac{1}{2}\langle \delta \hat{a}_i^\dagger \delta \hat{a}_b + \delta \hat{a}_b \delta \hat{a}_i^\dagger \rangle), \quad (3.78)$$

$$\partial_z A_i = -\iota\kappa(\lambda_i)f(z)(A_s^* A_b + \frac{1}{2}\langle \delta \hat{a}_s^\dagger \delta \hat{a}_b + \delta \hat{a}_b \delta \hat{a}_s^\dagger \rangle), \quad (3.79)$$

$$\partial_z A_b = -\iota\kappa(\lambda_b)f^*(z)(A_i A_s + \frac{1}{2}\langle \delta \hat{a}_s \delta \hat{a}_i + \delta \hat{a}_i \delta \hat{a}_s \rangle). \quad (3.80)$$

Here, the capital letters correspond to the mean values of the fields whereas the δ terms describe the quantum mechanical fluctuations. Subtracting these mean field equations from the original equations results in the set of equations that were used to develop the matrix formalism in Section 3.3.1. This shows that during the linearization we assumed the following

$$\frac{1}{2}|\langle \delta \hat{a}_i^\dagger \delta \hat{a}_b + \delta \hat{a}_b \delta \hat{a}_i^\dagger \rangle| \ll |A_i^* A_b|, \quad (3.81)$$

$$\frac{1}{2}|\langle \delta \hat{a}_s^\dagger \delta \hat{a}_b + \delta \hat{a}_b \delta \hat{a}_s^\dagger \rangle| \ll |A_s^* A_b|, \quad (3.82)$$

$$\frac{1}{2}|\langle \delta \hat{a}_i \delta \hat{a}_s + \delta \hat{a}_s \delta \hat{a}_i \rangle| \ll |A_s A_i|. \quad (3.83)$$

N.L.C.S. calculates exactly these expectation values on the left hand side using the linearized steady state solution for the quantum mechanical fluctuations and divides these by the right hand side of the above inequalities. The resulting quantities have then to be small compared to one. This error estimation can be plotted by specifying

```
Plot {
    y = "error"
}
```

inside the configuration file for N.L.C.S.. Mathematically, the expectation values are given by the relation

$$\langle \delta \hat{s}_k \delta \hat{s}_l \rangle = \sum_i \left(T_i \mathcal{V}_i' T_i^T \right)_{kl}, \quad (3.84)$$

3.7. Influence of the Gouy phase shift

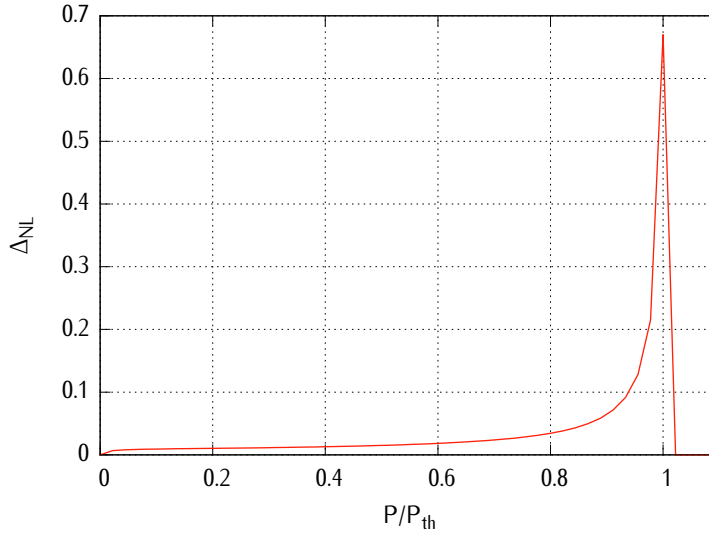


Figure 3.21.: For perfect phase matching the linearization of the quantum fluctuations is invalid in case of the OPO cavity near to its threshold. The linearization is valid if the curve is well below one.

where the sum is taken over all input ports and T_i is the transfer matrix from input i to the intra-cavity field c . The matrix $\gamma'_i = (M^T \gamma M + K)/4$ is again the transformed covariance matrix and $\delta \hat{s}$ is the state vector that was also defined in Equation 3.14.

It turns out that the linearization is only invalid in the case of an optical parametric oscillator near threshold as shown in Figure 3.21. The biggest correction term Δ_{NL} shows up for the calculation of the harmonic mode. As shown by Chaturvedi et al. [34] this system is well described by a semi-classical method and can therefore only generate Gaussian states of light.

3.7. Influence of the Gouy phase shift

In this Section the influence of the Gouy phase shift on the non-linear interaction is investigated. This is helpful to get a physical interpretation of the numerical simulation that was described in the previous Sections. Boyd and Kleinman found [7] that the maximum non-linear coupling between two Gaussian beams of fundamental (subscript 1) and second harmonic (subscript 2) waves is achieved for a positive wave vector mismatch $\Delta k = 2k_1 - k_2 > 0$. It was further shown that this mismatch increases with decreasing waist size of the beam. For a single-pass through a non-linear crystal of length L they numerically found the optimal focusing parameter

3. N.L.C.S. - The non-linear cavity simulator

given by the relation

$$\xi := \frac{L}{2z_R} \approx 2.84, \quad (3.85)$$

where $z_R = \pi w_0^2 n_1 / \lambda$ is the Rayleigh range of the beams inside the crystal, and w_0 , n_1 and λ are the beam's waist radius, refractive index and wavelength, respectively. The quantity ξ is also called the Boyd-Kleinman factor.

First, I will show that this Boyd-Kleinman factor is a consequence of maximizing the intensity of the mean pump field inside the non-linear medium under the constraint of the Gouy phase shift. With this knowledge it is possible to achieve an even higher non-linear interaction by using a position dependent index of refraction to compensate the influence of the Gouy phase shift. It is further shown that this effect has a significant influence on the coupling of the waves when a resonator is used to enhance the non-linearity.

Let me recall the coupled differential equations (see Eq. 3.3) for a single-pass through a $\chi^{(2)}$ non-linear crystal in the case of degenerate fundamental frequencies and without absorption

$$\partial_z A = -\iota g(z) A^* B, \quad (3.86)$$

$$\partial_z B = -2\iota g^*(z) A^2, \quad (3.87)$$

$$g(z) = \kappa \frac{e^{-\iota \Delta k z}}{1 - \iota \frac{z - z_0}{z_R}} = \frac{w_0}{w(z)} e^{-\iota(\Delta k z + \Delta \phi(z))}, \quad (3.88)$$

where A and B are the complex field amplitudes for the fundamental and harmonic mode, respectively. Again, κ is the non-linearity of the material, z_R is the Rayleigh range of the modes and z_0 is the waist position. The function $g(z)$ describes the non-linear interaction and was rewritten to clearly see the influence of the Gouy phase $\phi_G(z)$ on the interaction. The waist radius w and the phase $\Delta \phi$ at the longitudinal position z are given by

$$w(z) = w_0 \sqrt{1 + \left(\frac{z - z_0}{z_R} \right)^2}, \quad (3.89)$$

$$\Delta \phi(z) = -\arctan \left(\frac{z - z_0}{z_R} \right) = \phi_G(z). \quad (3.90)$$

In plane wave theory ($z_R \rightarrow \infty$) one finds $g(z) = \kappa \exp(\iota \Delta k z)$ and $\Delta \phi = 0$, and equal indices of refraction for the two interacting modes provide the maximum non-linearity. When focusing the beam into a non-linear material however, there is a non zero phase difference $\Delta \phi$ which is identical to the Gouy phase shift of a TEM₀₀ mode in our case. Note that each partial wave that is generated within the crystal gains this phase in addition to its propagation phase. From this one can conclude that the Gouy phase shift leads to a non-perfect matching of the (non-planar) phase

3.7. Influence of the Gouy phase shift

fronts in non-linear processes. To quantify this effect, we define the effective non-linearity κ_{eff} of the process. This quantity is proportional to the conversion efficiency in second harmonic generation as well as to the optical gain of optical parametric amplification. For weak interaction, i.e. the pump field is not depleted by the non-linear interaction, κ_{eff} is given by

$$\kappa_{\text{eff}} = \left| \int dz \frac{g(z)}{w_0} \right|^2, \quad (3.91)$$

where the integration is taken over the whole interaction length. For a single-pass through a non-linear medium of length L , the effective non-linearity is given by

$$\kappa_{\text{eff}} = \left| \kappa \int_0^L dz \frac{e^{i(\Delta kz + \phi_G(z))}}{w(z)} \right|^2. \quad (3.92)$$

This quantity is maximized if the averaged field strength inside the crystal is maximized, i.e. if the focus is placed in the crystal center, and if the condition

$$\Delta kz + \phi_G(z) = \phi_0 = \text{const.} \quad (3.93)$$

is satisfied. In this case all partial waves are produced exactly in phase to each other and perfect phase matching is realized.

Curves (a) in Fig. 3.22 show the differential Gouy phase shifts $\Delta\phi(z) = \phi_G(z)$ for weak and strong focusing. In the former case the Gouy phase shift evolves linearly inside the medium, and one can compensate this phase mismatch by choosing $\Delta k = 1/z_R > 0$, as found by Boyd and Kleinman. For stronger focusing, however, it is not possible to achieve perfect compensation by using a constant value of Δk over the crystal length. Curves (b) show the compensating linear phase Δkz that is due to the propagation inside the medium and curves (c) show the total phase ϕ_0 . The value of Δk was chosen to provide the lowest variance of ϕ_0 over the whole interaction range.

From the condition 3.93 we get the expression for the position dependent difference of the refractive indices $\Delta n(z)$

$$\Delta n(z) = \frac{\lambda}{4\pi} \Delta k(z) = \frac{\lambda}{4\pi} \frac{\phi_0 + \arctan\left(\frac{z-z_0}{z_R}\right)}{z}, \quad (3.94)$$

where the constant value of the phase ϕ_0 is set by the Gouy phase at the entrance surface of the non-linear medium

$$\phi_0 = \arctan\left(\frac{z_0}{z_R}\right) = \phi_G(0). \quad (3.95)$$

Figure 3.23 shows $\Delta n(z)$ for a non-linear crystal of length L for different focusing parameters ξ . The focus is always placed at the center of the crystal. These curves

3. N.L.C.S. - The non-linear cavity simulator

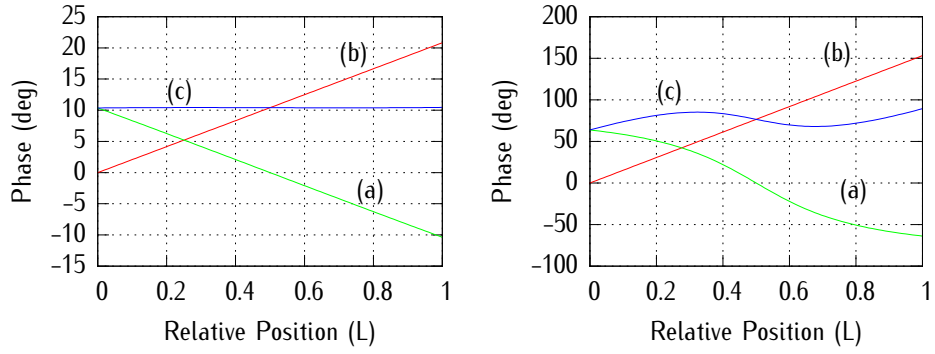


Figure 3.22.: Left: For weak focusing into the non-linear medium ($\xi = 0.18$) the Gouy phase shift can be compensated by choosing $\Delta k = 1/z_R$, and perfect phase matching can be realized over the full crystal length. Right: For stronger focusing ($\xi = 2.03$) a constant Δk can not provide perfect phase matching anymore. (a) Gouy phase shift $\Delta\phi = \phi_G$, (b) compensating phase Δkz , (c) overall phase ϕ_0 , where a constant value describes perfect phase matching.

could experimentally be realized by applying an appropriate temperature gradient along the z -direction. Alternatively, an electrical field applied to the crystal could be used.

The effective non-linearity for the single-pass setup with perfect Gouy phase compensation can be written as

$$\kappa_{\text{eff}} = \left| \kappa \int_0^L dz \frac{1}{w(z)} \right|^2 = \frac{1}{\xi} \ln^2 \left(\frac{\sqrt{1 + \xi^2} + \xi}{\sqrt{1 + \xi^2} - \xi} \right), \quad (3.96)$$

with $\xi = L/2z_R$. The numerical maximization of this expression leads to

$$\xi_{\text{opt}} = 3.32. \quad (3.97)$$

3.7. Influence of the Gouy phase shift

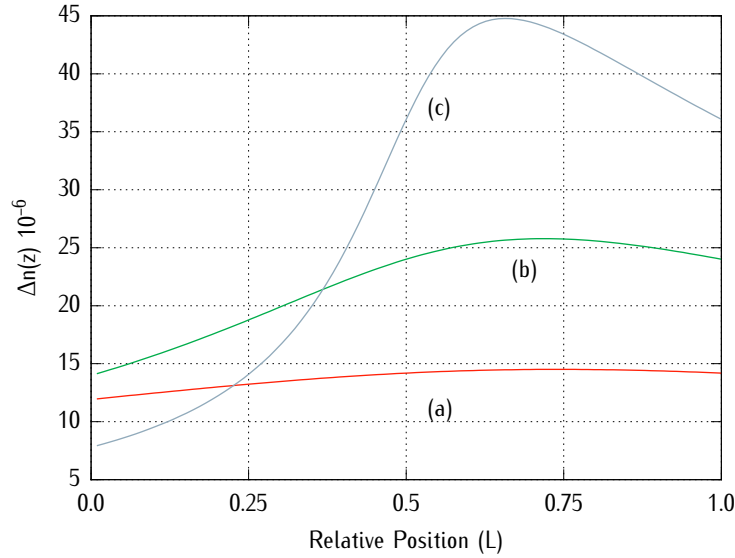


Figure 3.23.: Change of refractive index along the crystal to compensate for the Gouy phase shift, for three different strengths of the focusing. (a) $\xi = 0.55$, (b) $\xi = 1.14$, (c) $\xi = 3.32$.

This result means that using optimum, position dependent phase matching, the optimal waist size is approximately 7.5 % smaller than suggested by the Boyd-Kleinman factor, and according to this, the effective non-linearity is further increased by 4.4 %. This shows that the slight phase mismatch due to the Gouy phase is not the dominating factor for the presence of an optimal focus for the non-linear interaction. As the term $1/w(z)$ is proportional to the electrical field at position z inside the crystal, the integral term in Equation 3.96 is proportional to the mean field \bar{E} inside the crystal

$$\bar{E} \propto \int_0^L dz \frac{1}{w(z)}. \quad (3.98)$$

Therefore, the statement of Boyd and Kleinman that there exists an optimum choice of the focusing parameter ξ is essentially due to the maximization of the intensity of the mean field inside the non-linear material.

The additional Gouy phase causes a much stronger effect when considering a cavity around the non-linear material. This effect is similar to the well known influence of the high reflective coating of a cavity's end mirror that might introduce a differential phase between the fundamental and harmonic wave. The effective non-linearity

3. N.L.C.S. - The non-linear cavity simulator

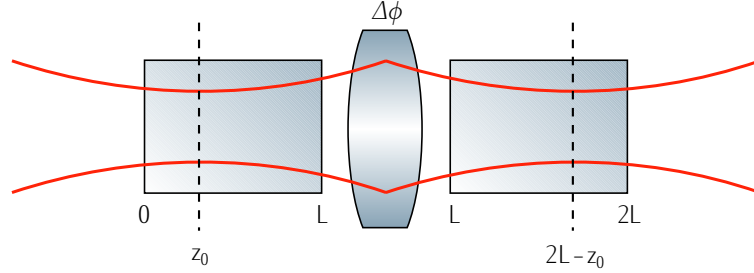


Figure 3.24.: Scheme of the double-pass through a non-linear crystal that is placed inside a resonator. The end mirror of this cavity might introduce a differential phase $\Delta\phi$ between the modes. The resonator was unfolded to depict the different locations of the waist for each single-pass.

for plane waves and a double-pass inside a single ended cavity reads

$$\kappa_{\text{eff}} = \kappa \text{sinc}^2(x) \cos^2 \left(x + \frac{\Delta\phi}{2} \right), \quad (3.99)$$

where $x = \Delta kL/2$, $\Delta\phi$ is the phase difference that is introduced by the highly reflective coating and $\text{sinc}(x) = \sin(x)/x$. To interpret this result, consider the case of perfect phase matching $\Delta k = 0$ so that $\kappa_{\text{eff}} = \kappa \cos^2(\Delta\phi/2)$. If the coating of the end mirror now introduces a differential phase shift of π , the partial waves that were generated in phase on the way to the end mirror will destructively interfere with those waves that are produced on the way back to the incoupling mirror. In this case the effective non-linearity vanishes and no mode conversion will occur at the output of the cavity.

For the calculation of the double-pass effective non-linearity in the case of focused Gaussian beams we model the system with a non-linear medium of length $2L$ with a thin lens at position L that refocuses the beam (see Fig. 3.24). In this way we obtain two waists at positions z_0 and $z'_0 = 2L - z_0$ of size w_0 indicating the way to the end-mirror and the way back, respectively. Now we integrate over $2L$ and find the

3.7. Influence of the Gouy phase shift

following expression for the effective non-linearity for a double-pass of the mode

$$\begin{aligned}
\kappa_{\text{eff}} &= \frac{\kappa}{w_0^2} \left| \int_0^L dz g(z, z_0) + \int_L^{2L} dz g(z, z'_0) e^{i\Delta\phi} \right|^2 \\
&= \frac{\kappa}{w_0^2} \left| \int_0^L dz [g(z, z_0) + g(z+L, z'_0) e^{i\Delta\phi}] \right|^2 \\
&= \kappa \left| \int_0^L dz \frac{e^{i(\Delta kz + \phi_G(z))}}{w(z)} \times \left(1 + \frac{w(z)}{w'(z)} e^{i\theta} \right) \right|^2, \quad (3.100)
\end{aligned}$$

$$\theta = \phi'_G(z) - \phi_G(z) + \Delta kL + \Delta\phi, \quad (3.101)$$

where $w'(z)$ and $\phi'_G(z)$ belong to the focus at position z'_0 and $\Delta\phi$ is again the differential phase that might be introduced by the coating of the back reflecting mirror. The first factor within the integral describes the single-pass interaction whereas the second factor is the correction for reflecting off the end mirror of the cavity.

In the case of weak focusing $|z - z_0| \ll z_R \forall z \in [0, L]$, the above integral can be simplified to

$$\kappa_{\text{eff}} = \text{sinc}^2 \left(\frac{\Delta k' L}{2} \right) \cos^2 \left(\frac{\Delta k' L}{2} + \frac{\Delta\phi'}{2} \right), \quad (3.102)$$

where $\Delta k' := \Delta k - 1/z_R$ and $\Delta\phi' := \Delta\phi + 2(L - z_0)/z_R$. This expression has the same form as the one for plane waves as given above. However, an additional phase shift appears due to the swapping in sign of the wave front's radius of curvature during reflection. It corresponds to minus twice the Gouy phase at the end mirror in the limit considered here. From the expression of $\Delta\phi'$ it follows that this additional phase jump vanishes if the waist is located exactly at the back reflecting surface. In this case we have plane wave fronts at the end mirror and therefore the system is identical to a single-pass through a non-linear medium of length $2L$.

For arbitrary strong focusing of the beam into the center of the non-linear crystal we get the following expression for the effective non-linearity

$$\kappa_{\text{eff}} = 4 \cos^2 \left(\frac{\Delta kL + \Delta\phi}{2} \right) \left| \int_0^L dz \frac{e^{i(\Delta kz + \phi_G(z))}}{w(z)} \right|^2. \quad (3.103)$$

The first factor of this equation provides the optimal phase of the end mirror coating of $\Delta\phi = -\Delta kL$, by maximizing the cosine. To also maximize the integral expression, one has to minimize the variance of the phase argument $\Delta kz + \phi_G(z)$ over the whole interaction range. The variance V_ϕ is given by

$$V_\phi = \frac{1}{L} \int_0^L dz (\Delta kz + \phi_G(z) - \bar{\phi})^2, \quad (3.104)$$

3. N.L.C.S. - The non-linear cavity simulator

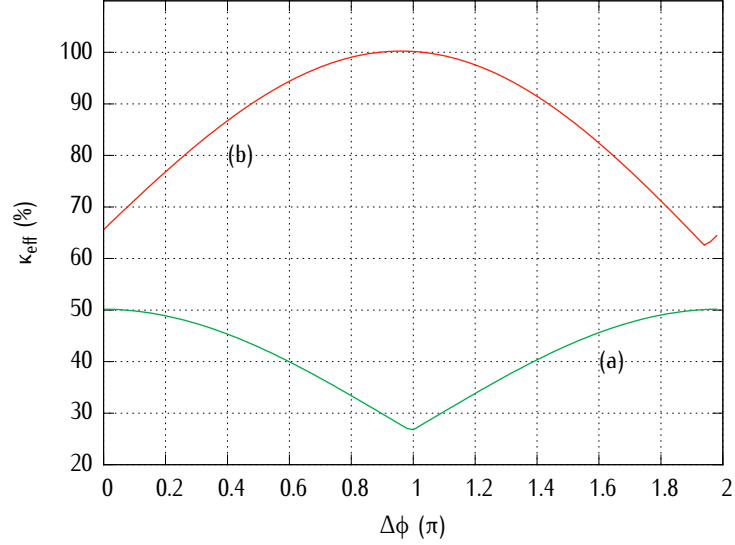


Figure 3.25.: Normalized effective non-linearity κ_{eff} versus the differential phase introduced by the back reflecting surface $\Delta\phi$. For Gaussian beams with waist position on the reflecting surface (a), $\Delta\phi = 0$ generally provides the highest non-linearity (here with strong focusing $\xi = 2.84$, $z_0 = L$); the same result is found for plane waves. Contrary, for $\xi = 2.84$ and $z_0 = L/2$ we find $\Delta\phi \approx \pi$, which is shown in trace (b).

where $\bar{\phi}$ is the mean value of the phase that is defined by

$$\bar{\phi} = \frac{1}{L} \int_0^L dz (\Delta kz + \phi_G(z)) = \frac{\Delta kL}{2}. \quad (3.105)$$

The last identity is due to the fact that the focus is located in the center of the non-linear medium and the Gouy phase being an odd function.

We obtain the following expression for the optimal differential phase $\Delta\phi$ of the end mirror versus the focusing parameter ξ

$$\Delta\phi = -\frac{3}{\xi^2} [(1 + \xi^2) \cdot \arctan(\xi) - \xi]. \quad (3.106)$$

Figure 3.25 shows the effective non-linearity versus the differential coating induced phase $\Delta\phi$ for two different standing wave cavity arrangements. In all cases the second harmonic wave is not resonant but simply back reflected. Both curves use the focusing parameter $\xi = 2.84$, which is the optimum if the phase mismatch is constant. For curve (a) the waist was directly positioned on the surface of the

3.7. Influence of the Gouy phase shift

end mirror which is similar to the case of plane waves. You can see that the effective non-linearity is maximized if the differential phase $\Delta\phi = 0$, whereas the minimum occurs for $\Delta\phi = \pi$. This is exactly the opposite behaviour as for the curve (b) where the focus is placed in the center of the crystal. This is because the Gouy phase at the end of the non-linear crystal has almost reached its maximum value of $\phi_G(\infty) = \pi/2$ since we use the optimal focusing which is rather strong. As shown in a previous paragraph, the focusing leads to an additional phase at the back reflecting mirror that is twice the Gouy phase at this position.

4. Modelling thermal effects inside optical cavities

This Chapter introduces a new method for measuring small optical absorptions. It is based on the deformation of the Airy peak of a high finesse cavity due to thermally induced self-phase modulation. The targeted sensitivity of the scheme is as low as 0.01 ppm/cm and will be used to investigate the absorption of crystalline silicon which is a candidate material for the testmasses of the next generation gravitational wave detectors.

4.1. Overview

Materials with low optical absorption coefficients are essential for high-precision laser-interferometric measurements. Absorptions in mirror substrates of as low as 10^{-6} /cm already limit gravitational wave detectors because absorption leads to heating and a thermal deformation of the mirrors [12] and also to photo-thermal noise [13]. Future gravitational wave detectors will use cryogenically cooled mirrors [35] to reduce thermally excited motions of mirror surfaces. Then, low optical absorptions will become even more crucial. Consequently, the measurement of small absorption coefficients in the regime below 10^{-6} /cm is important to find appropriate mirror materials and to enable the reliable design of future gravitational wave detectors, such as the Einstein Telescope [36].

In the past, several methods have been developed that are able to measure absorption coefficients of the order of 10^{-6} /cm. All these methods are based on indirect measurement schemes. They do not directly sense the power loss of a transmitted beam but utilize the temperature increase that arises due to the absorption. In calorimetric approaches the temperature increase is directly measured [37]. Other approaches exploit light beam deflection or beam shape deformation due to local heating [38, 14].

As opposed to the methods mentioned above, the new approach described in this Chapter utilizes the back-action of the temperature on the optical path of the light that caused this temperature increase. Only the phase but not the shape of the mode is changed. The material under investigation is put inside an optical cavity whose length is linearly scanned over a single Airy peak. Approaching cavity resonance the temperature along the resonator mode increases and the optical path length for

4. Modelling thermal effects inside optical cavities

one round trip changes. The thermally induced optical path length change is a photo-thermal self-phase modulation resulting in a deformed shape of the Airy peak. Since the phase change depends on the light intensity it may be considered as the result of a “thermo-optic-Kerr-effect”. Importantly, the Airy peak deformation depends on the scan direction, i.e. whether the cavity is shortened or lengthened. The hysteresis in the time-resolved measurements provides information of the absorption coefficient, if relevant material parameters are known and included in a numerical time-domain simulation. A positive side-effect of our method is the power build-up inside the cavity which compensates the need for laser sources with higher powers when approaching the regime of extremely low absorption.

4.2. Estimation of the heating process

In this Section we will use the steady-state approximation of the heating process inside a cavity as given by Winkler et al. [12]. This estimation will give us an upper bound for the temperatures and time scales that are involved in the heating process. As we will see in a later Section, the time evolution of the temperature profile can not be neglected in the numerical simulation.

To consider the absorption of the laser power within the mirror coating, we can assume that the temperature change is only relevant within a hemisphere of radius w around the beam center, where w is the radius of the incident beam. This situation is depicted in figure 4.1. In this case the change of the optical path length δs is given by

$$\delta s = \frac{a_{\text{th}} + \frac{\partial n}{\partial T}}{4\pi\kappa} P_a, \quad (4.1)$$

where a_{th} is the thermal expansion coefficient, $\partial n/\partial T$ is the temperature dependence of the index of refraction, κ the thermal conductivity and P_a the light power that is absorbed by the coating. From the relation

$$P_a = \kappa(2\pi w^2)\nabla T \approx 2\pi\kappa w\delta T, \quad (4.2)$$

we get the resulting temperature increase to be

$$\delta T = \frac{P_a}{2\pi\kappa w}. \quad (4.3)$$

Here, it was assumed that the temperature drops linearly along the radius of the hemisphere, i.e. within the beam waist.

Another quantity of interest is the time t that it takes for heating the hemisphere by this temperature δT . This can be derived by demanding that the absorbed power P_a has to heat the hemisphere by the particular temperature difference, which is expressed by the relation

$$P_a = \frac{c_s M \delta T}{t}. \quad (4.4)$$

4.2. Estimation of the heating process

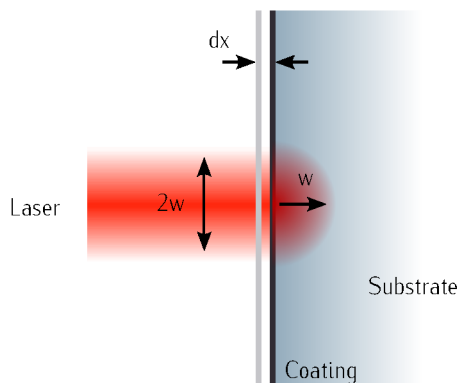


Figure 4.1.: The absorption of the mirror coating leads to a temperature gradient within the hemisphere of radius w around the beam center, which leads to an expansion dx of the mirror.

Material parameter (Si)		Derived parameter	
a_{th} ($10^{-6}/\text{K}$)	2.62	t (ms)	0.49
$\partial n/\partial T$ ($10^{-6}/\text{K}$)	206.0	δT (mK)	48.72
κ (W/(m K))	140.0	δs (nm)	1.78
c_s (J/(kg K))	713.9		
ρ (kg/m^3)	2330.0		

Table 4.1.: Material parameters and estimated values for silicon.

Here, c_s is the specific heat capacity of the material and M is the mass of the hemisphere. Inserting the expressions for δT and using $M = 2/3 \pi w^3 \rho$ leads to the following result

$$t = \frac{1}{3} \frac{c_s \rho w^2}{\kappa}, \quad (4.5)$$

where we have introduced the density ρ of the mirror. In Table 4.1 the estimated values for t , δT and δs for silicon are listed. The beam parameters that were chosen are given by $w = 350 \mu\text{m}$ and $P_a = 15 \text{ mW}$. For calculating the latter value we assumed a cavity finesse of $F = 20000$, a total absorption of $\alpha = 1 \text{ ppm}$ and an incident light power of $P_{\text{in}} = 1 \text{ W}$. The values suggest that the time to heat the small hemisphere is short enough to see an influence on the Airy peaks while scanning the resonator. Furthermore, the maximum temperature of the coating is small enough to neglect other thermal effects that may happen inside the coating layers. As a rule of thumb, typical coatings show an additional phase when they are heated, with a temperature dependence of $d\phi/dT \approx 0.006$ °[39]. To get a feeling on the strength

4. Modelling thermal effects inside optical cavities

of the thermal effect, the additional optical path length has to be compared to the cavity linewidth. At a wavelength of $\lambda = 1550$ nm the linewidth is given by

$$\delta l = \frac{\lambda}{F} = 0.0775 \text{ nm} . \quad (4.6)$$

Because of the high finesse, δs belongs to a detuning of $\delta = \delta s / \delta l \approx 23$. This is a very strong effect and we get a first hint that the approximation can not be applied to the case of scanning such a high finesse cavity.

If we now consider the case of absorption inside the bulk of the mirror, a closed form expression can be given that has the same form as the above expression for the coating. It reads

$$\delta s = 1.3 \frac{a_{\text{th}} + \frac{\partial n}{\partial T}}{4\pi\kappa} p_a d , \quad (4.7)$$

where p_a is the absorbed power per unit length and d is the length of the intra-cavity substrate. For the same power that is absorbed by either the coating or the bulk, these expressions only differ by a factor of 1.3. If we again calculate the change in temperature and the time it takes for this warming, we end up with the following equations

$$\delta T = \frac{1.3 P_a}{4\pi\kappa d} , \quad (4.8)$$

$$t = \frac{1.3 c_s \rho w^2}{4 \kappa} . \quad (4.9)$$

This time the volume that is heated is given by the beam which can be approximated by a rod with mass $M = \pi w^2 d \rho$, where d is the length of the substrate. Because the thickness of the material is generally much bigger than the beam radius, the temperature increase for the bulk absorption is lower than that for the coating absorption given the same absorptions. Note that the expression for the time constant is almost identical and deviates only by 2.5 %. Therefore the thermal effects of the coating and the bulk are of the same order for equal absorbing powers.

As there is a strong thermal effect present in our scenario that has such a small time constant, we have to use a complete description of the heating in the time-domain, i.e. we have to consider transient effects during the cavity build-up. The calculations are explained in the next Sections.

4.3. Time domain simulation of the cavity

To simulate the scan over a single Airy peak of a cavity showing thermal aberration, we have to use a time domain model (see Section 4.2). Figure 4.2 shows a schematic of the general cavity layout that will be simulated.

4.3. Time domain simulation of the cavity

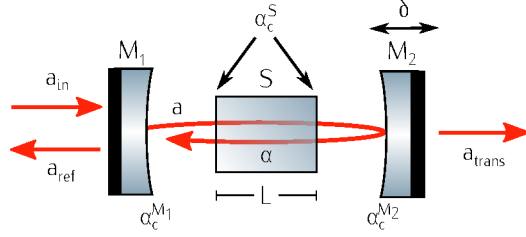


Figure 4.2.: Scheme of the general cavity layout that can be simulated. The intra-cavity field a is confined by the mirrors M_1 and M_2 and is depleted by either the mirror or substrate coating absorptions (α_c^{M1} , α_c^{M2}) and α_c^S or the substrate bulk absorption α .

The incident light field a_{in} passes the incoupling mirror M_1 and is then propagated through the substrate S that might be present inside the cavity. After reflecting off mirror M_2 and again passing the intra-cavity material, the light reaches the entrance again. The field a_n (right behind mirror M_1) after n round-trips can be expressed by the same field after $n - 1$ round trips and is given by

$$a_n = t_1 a_{in} e^{i\phi_{in}} + r_1 r_2 a_{n-1} e^{i(\delta + \phi_{cav})} - \alpha_{tot} a_{n-1}. \quad (4.10)$$

Here r_1 and r_2 are the amplitude reflectivities of mirrors M_1 and M_2 , respectively. The corresponding transmissivities are given by $t_1 = \sqrt{1 - r_1^2}$ and $t_2 = \sqrt{1 - r_2^2}$. The total loss per roundtrip α_{tot} for this cavity is given by

$$\alpha_{tot} = \alpha L + m \alpha_c^S + \alpha_c^{M1} + \alpha_c^{M2}, \quad (4.11)$$

with the bulk power absorption α and the coating absorptions for the substrate α_c^S and the two mirrors α_c^{M1} and α_c^{M2} , respectively. It is assumed that both coating losses for the intra-cavity substrate are equal. The factor m counts for the different cavity geometries. Given an external cavity, m is equal to 4, for a hemilithic cavity it is 2 and for a monolithic cavity it is zero.

Without loss of generality the amplitude of the incident field a_{in} is assumed to be real and is given by the relation

$$a_{in} = \sqrt{\frac{4P_{in}}{c \epsilon_0 \pi w_0^2}}. \quad (4.12)$$

Here, c is the speed of light and ϵ_0 is the vacuum permittivity. The incident mode has a power of P_{in} and a waist radius of w_0 .

For the recurrence relation given by Equation 4.10 we need to specify the initial value for the intra-cavity field a_0 . Since the simulation is started at an arbitrary

4. Modelling thermal effects inside optical cavities

detuning δ_0 we avoid using $a_0 = 0$, but rather use the steady-state solution of a cavity without absorption, which is given by the expression

$$a_0 = t_1 \frac{a_{\text{in}}}{1 - r_1 r_2 e^{i\delta_0}}. \quad (4.13)$$

Otherwise the intra-cavity field will show a short transient oscillation at the beginning of the simulation.

There are three different phases involved in the Equation 4.10, where ϕ_{in} and ϕ_{cav} are due to the thermal effects inside the cavity and the remaining phase δ is due to constantly scanning the resonator above its resonance. Let us first consider the phase δ which is proportional to the number of round-trips. Within the cavity round-trip time $\tau = 2L_c/c = 1/\text{FSR}$ the mirror M_2 moves by the distance $\Delta L_c = v_m \tau$. Here, FSR is the cavities free spectral range, $L_c = s + n_s L_s$ is the optical path for a single-pass. L_s is the length of the intra-cavity substrate with index of refraction n_s and s is the total air gap of the cavity. The velocity v_m of the mirror is given by

$$v_m = N_{\text{FSR}} \lambda 2\omega_s, \quad (4.14)$$

where N_{FSR} is the number of free spectral ranges that were scanned with a frequency ω_s and λ is the wavelength of the incident field. Therefore, $N_{\text{FSR}} \lambda$ is the distance that the mirror moves within half a period of the excitation which is given by $1/(2\omega_s)$. Putting this all together we end up with the following equation for the detuning after n round-trips

$$\delta = \delta_0 + n 2\pi \frac{\Delta L_c}{\lambda} = \delta_0 + n 4\pi N_{\text{FSR}} \frac{\omega_s}{\text{FSR}}. \quad (4.15)$$

The phase ϕ_{in} is mainly due to the absorption of the intra-cavity power at the coating of mirror M_1 . That is because the power inside the resonator is much higher than the incident light power and therefore any thermal effects of the latter might be neglected (the simulation includes both powers). The absorption leads to a temperature gradient inside the incoupling mirror which leads to a time dependent phase of the incident light field. If this phase changes within the order of the cavities build-up time it has an influence on the resulting fields.

The intra-cavity field is in general absorbed by the two coatings of the substrate and its bulk which leads to the time dependent phase ϕ_{cav} . The correct determination of these phases is described in the next Section. Note that we don't have to consider the phases for the transmission of the intra-cavity field through the mirrors M_1 and M_2 since they will only introduce a global phase on the field which can not be measured anyway.

Finally, the output fields are defined by the relations

$$a_n^{\text{trans}} = t_2 a_n e^{i(\delta + \phi_{\text{cav}})/2}, \quad (4.16)$$

$$a_n^{\text{ref}} = r_1 a_{\text{in}} e^{i\phi_{\text{in}}} + t_1 r_2 a_n e^{i(\delta + \phi_{\text{cav}})}. \quad (4.17)$$

4.4. Numerical calculation of the temperature distribution

Here, the superscripts *ref* and *trans* belong to the field in reflection and transmission, respectively. The power of these fields is then given by

$$P_n^{\text{trans}} = \frac{c \epsilon_0 \pi W_0^2}{4} |a_n^{\text{trans}}|^2, \quad (4.18)$$

$$P_n^{\text{ref}} = \frac{c \epsilon_0 \pi W_0^2}{4} |a_n^{\text{ref}}|^2. \quad (4.19)$$

4.4. Numerical calculation of the temperature distribution

In this Section I will summarize the calculation of the thermal aberrations as given by Hello and Vinet [9, 10]. The first of these papers deals with an exact calculation of the temperature profile inside a substrate depending on time and position. The heating is due to the absorption of the bulk material as well as to the absorption of a coating. The latter is assumed to be infinitesimally thin and is therefore simulated by a heat flux. Furthermore, the problem is assumed to be radially symmetric and radiative as well as convective losses can be included. At the very beginning, the substrate is in thermal equilibrium with its environment and is then heated by absorbing the incident laser power, where only small deviations from the environmental temperature T_{ext} are allowed. This assumption leads to the fact that the problem becomes linear and thus the different heating processes (due to coating and bulk losses) can be treated independently. It is further assumed that the temperature profile changes on a scale that is much bigger than the wavelength of the light and the beam radius is much smaller than the radius of the substrate. Lastly, the degradation of the light power inside the material is neglected. All these assumptions are valid as we will use this method to quantify small absorptions.

To solve the heat equation given by

$$\rho C \frac{\partial T(t, r, z)}{\partial t} - K \Delta T(t, r, z) = 0, \quad (4.20)$$

the authors first search for the steady-state solution by writing the temperature as

$$T(r, z) = T_{\text{ext}} + T_{\infty}(r, z), \quad (4.21)$$

demanding that $\Delta T_{\infty}(r, z) = 0$. Here, ρ is the density, C the specific heat and K the thermal conductivity of the material. The function $T(t, r, z)$ is the temperature profile depending on the time t and the position as given by the longitudinal coordinate z and the distance r from the optical axis. The boundary conditions state that the heat at the substrates surface is emitted given by the Stefan-Boltzmann relation

$$F = \sigma'(T^4 - T_{\text{ext}}^4) \approx 4\sigma' T_{\text{ext}}^3 \delta T, \quad (4.22)$$

4. Modelling thermal effects inside optical cavities

where the approximation is valid for small temperature differences $\delta T = T - T_{\text{ext}}$. Here, F is the radiated power per surface area and σ' is the Stefan-Boltzmann constant corrected for emissivity. The general solution for this static problem is then given by

$$T_{\infty}(r, z) = \sum_m \left(A_m e^{k_m z} + B_m e^{-k_m z} \right) J_0(k_m r), \quad (4.23)$$

where J_0 is the zero order Bessel function. Although the coefficients A_m , B_m and k_m can be given analytically, it is necessary to solve some equations numerically in order to really calculate them.

With the knowledge of the static solution T_{∞} it is then possible to determine the transient solution $T_{\text{tr}}(t, r, z)$ by again splitting the temperature into the following terms

$$T(t, r, z) = T_{\text{ext}} + T_{\infty}(r, z) + T_{\text{tr}}(t, r, z). \quad (4.24)$$

Inserting this expression into the heat equation the transient solution has the following form of a rapidly converging Dini series

$$T_{\text{tr}}(t, r, z) = \sum_{\rho, m} \left(e^{-\alpha_{\rho m} t} A_{\rho m} \cos(u_{\rho} \frac{z}{a}) + e^{-\beta_{\rho m} t} B_{\rho m} \sin(v_{\rho} \frac{z}{a}) \right) J_0(\xi_m \frac{r}{a}). \quad (4.25)$$

Again, the coefficients are given by analytical expressions which use the roots of implicit equations that have to be determined numerically. The functions $\cos(u_{\rho} z/a)$ and $\sin(v_{\rho} z/a)$ form an orthogonal basis for functions defined within the interval $[-h/2, h/2]$. Here, h is the length and a the radius of the substrate. The coefficients $\alpha_{\rho m}$ and $\beta_{\rho m}$ are proportional to a characteristic time t_c that is given by

$$t_c = \frac{\rho C a^2}{K}. \quad (4.26)$$

This is the time it needs to reach thermal equilibrium starting when the laser is switched on. For a silicon substrate with radius of half an inch this time is $t_c \approx 2$ s, whereas for the mirrors of a gravitational wave detector it may take several hours to days to reach this steady-state.

After the temperature distribution is calculated, the additional phase $\phi(t, r)$ due to the change in optical path length is given by

$$\phi(t, r) = \frac{2\pi}{\lambda} \frac{dn}{dT} \int_{-h/2}^{h/2} dz (T(t, r, z) - T_{\text{ext}}). \quad (4.27)$$

This is exactly the phase that has to be inserted for ϕ_{cav} and ϕ_{in} in the cavity equations that were given in the last Section. Of course the temperature profile for the incoupling mirror has to be taken for the phase ϕ_{in} and the substrates temperature profile for the phase ϕ_{cav} .

The second paper [10] extends the first one by introducing recurrence relations for successive time steps. These relations can be used for simulating the build-up of an optical field inside a cavity in the time-domain, in the presence of absorbing mirrors and an intra-cavity substrate. The only assumption is that the time steps are much smaller than the characteristic time t_c . As for the simulation described in the next Section the time step is the cavity round-trip time $\tau = 1/\text{FSR}$, which is in the order of nanoseconds, the above assumption is valid since the characteristic time is in the order of seconds to minutes. The prospect of the numerical code from Hello and Vinet is to simulate the deformation and thermal aberrations of the cavity mirrors on time scales of minutes until the steady-state is reached. Therefore the cavity detuning can be treated as being constant and the power build-up inside the cavity can be calculated for a fixed temperature distribution. This is an important difference to the case where high-finesse cavities containing small substrates are used, since the time evolution of the temperature has to be considered during the build-up.

4.5. The simulation code

To implement the calculation as it was described in the last Sections, a C code was developed. The reason for using C was the complexity of the temperature profile calculation which is very CPU consuming. To provide an easy access to the simulation results and to simplify the further development of an automated fit routine, the core functionality is hidden in a library which is accessed via a *Python* interface. A schematic of the code design is illustrated in Figure 4.3. There is a central *Python* module *tksim.py* that is the main application. It parses some command line arguments and then creates an instance of the class *TkSim*, which is defined in the *Python* module *pytksim.py*. It is possible to run the simulation based on the values inside the file that was passed to the *tksim* application and optionally display the results using *Gnuplot* or just print the simulation results. Alternatively, it is possible to run some automated tests to make sure the application works properly.

The format of the initialization files is determined by the *ConfigParser* class which is an intrinsic class of the *Python* distribution. The application uses the default configuration from the file *default.ini* to determine which parameters are available and also assigns the values that are specified in that file to parameters that were not defined. The listing on the next page shows the content of the default file.

The file is splitted into sections (denoted by *[Section name]*), followed by the parameters for the section given as *parameter = value*. Everything after a *#* is considered to be a comment. The parameters in the file have a description and also the units are given.

4. Modelling thermal effects inside optical cavities

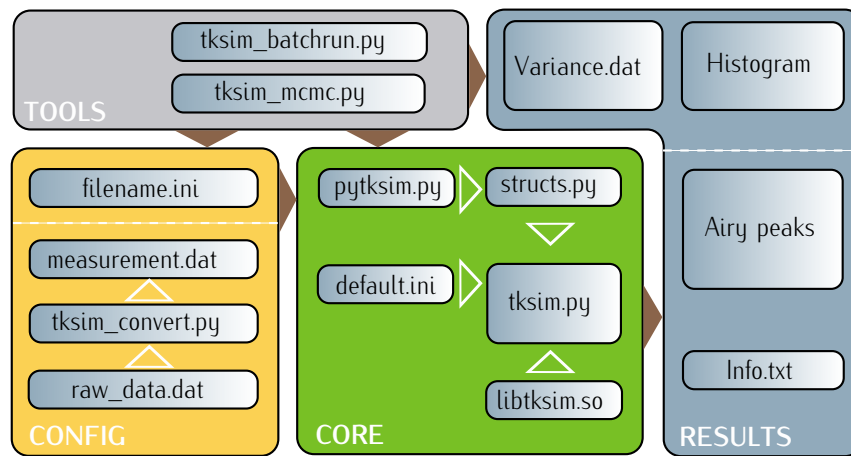


Figure 4.3.: Overview of the code design that was chosen to ease the development of further fitting routines and optimize the speed of the calculation. The core functionality including the calculation of the temperature distribution and the time-domain simulation was implemented in C within the library *libtksim.so*. The surrounding *Python* scripts access this library and perform the statistical analysis.

4.5. The simulation code

```
# Parameter overview and default value definition for pytksim
5  [Laser]
P = 0.0
Lambda = 1064e-9
w0 = 100e-6

10 [Cavity]
mm = 1.0
R1 = 0.9
R2 = 1.0
s = 0.0
15 NFSR_i = 1.0
NFSR_d = 1.0
omega_s = 10.0
delta_start = 0.0
delta_range = 1.0

20 [Measurement]
datafile = none
offset = 0.0
shift_i = 0.0
25 shift_d = 0.0
ref_val = 1.0
trans_val = 1.0
every = 1

30 [Substrate]
n = 1.0
dndT = 0.0
cw = 1.0
rho = 1.0
35 L = 0.0
R = 0.0
alpha = 0.0
alpha_coating = 0.0
a_th = 0.0
40 k_th = 1.0
epsilon = 1.0

[Mirror_1]
45 n = 1.0
dndT = 0.0
cw = 1.0
rho = 1.0

50 alpha = 0.0
alpha_coating = 0.0
a_th = 0.0
k_th = 1.0
epsilon = 1.0

55 #[Mirror 2]

[Control]
xRes = 100
60 mstep = 100
pstep = 1
Tstep = 100
TEPS = 1e-6
alpha_eats_photons = 1
65 T0 = 300.0
term = wxt
infofile = info.txt
datafile = none
phiFactor = 1
70
```

4. Modelling thermal effects inside optical cavities

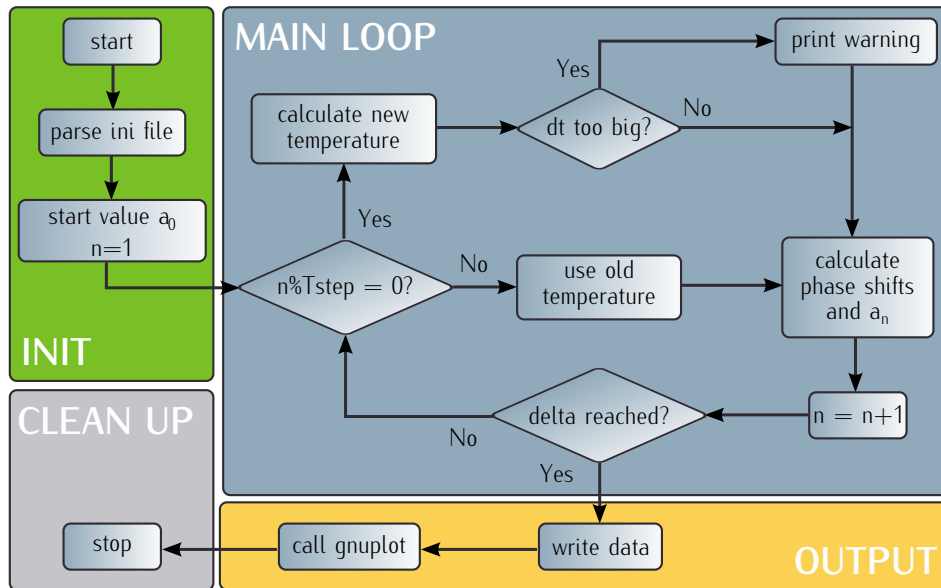


Figure 4.4.: Flowchart of the core calculation that is performed by the numerical time-domain simulation.

The figure 4.4 shows the core functionality of the code. When the simulation is started it first reads the ini file that was given as an argument on the command line. Then, the temperature calculation will be initialized. This includes the allocation of memory and the numerical calculation of the roots of some equations as mentioned in a previous Section. The starting values for the intra-cavity field, output fields and the initial temperature distribution are set here, too. Next, the code enters its main loop, where the fields for each successive round-trip are calculated. First, it is decided whether the temperature profile has to be recalculated. The user can control this step by adjusting the $Tstep$ variable which is the number of round-trips the code waits until the temperature is calculated again. If the temperature difference for two successive calculations is too big (defined by the $Teps$ variable), the code will print a warning. In this case the user might reduce $Tstep$. Note that the determination of the temperature distribution is by far the most CPU consuming part, therefore it is worth to spend some time to adjust this value. In a second step the thermal aberrations as well as the resulting fields are calculated using the relations given in Sections 4.3 and 4.4. Then the round-trip number is increased by one and if the end of the specified detuning is not reached the loop is repeated. If all values were calculated, the simulation optionally writes the raw data to a file and then calls *Gnuplot* to display the results. The last thing is to clean up, which includes freeing

4.6. Airy peak deformation in the presence of absorption

the allocated memory and closing all the file pointers. The next Section will show the qualitative changes of the Airy peaks undergoing thermal aberration inside a cavity.

4.6. Airy peak deformation in the presence of absorption

In this Section I will describe the quantitative influence of the thermal aberrations on the Airy peaks from a thermally loaded cavity. One effect that has not been discussed so far, but which is implicitly present in the simulation is the so called ringing effect [40]. This effect occurs at very fast scan frequencies and high finesse cavities and can be used to determine the finesse of these resonators. The idea behind the ringing effect is that the interference of the fields will change significantly if the phase of the intra-cavity field changes within the build-up time. In Figure 4.5 you can see an example of such peaks at different scan frequencies. Note that the maximum in transmission doesn't have to match the minimum in reflection in this case. Another point is that the cavity output can be bigger than the input. All this is due to the storage capabilities of the resonator and the change in interference of the beams.

Due to the time-domain nature of the code that I use to simulate the thermal effects the ringing effect is automatically included. Note that this effect has nothing to do with the absorption of the substrates or coatings, but only depends on the cavity's finesse and the speed of the mirror, which is given by the scan frequency and the scan range. Hence, the ringing effect will have no contribution to the hysteresis as seen for the thermal aberrations.

In the following it is assumed that the scan frequency is low enough to not introduce any ringing effect. In Figure 4.6 the Airy peaks from a thermally loaded resonator are shown for different absorptions. As you can see, the peak gets broader when shortening the cavity and it gets narrower when lengthening the cavity. This hysteresis effect can be understood as follows. The increasing light power inside the resonator results in a raising temperature and therefore in an increasing optical path length for the intra-cavity field (this is only true if $\partial n / \partial T + a_{th} > 0$, which is true for the materials considered in this thesis). Note that the scan direction has no influence on this, i.e. in both cases the optical path length increases. We might think of it as the mirror M_2 moving away from the mirror M_1 and therefore causing this increasing optical path length. When we now try to shorten the cavity, it will take a longer time to scan over a single peak, since the relative mirror speed is smaller than the speed of the scanned mirror. For lengthening the resonator the effect is just the opposite, i.e. the mirror speeds add up, leading to a faster scan over the peak which thus becomes more narrow.

In the bottom right plot the thermal effect is so strong, that the Gaussian mode is deformed and therefore the simulation is not valid anymore. Only the Airy peak for lengthening the cavity can then be calculated correctly.

4. Modelling thermal effects inside optical cavities

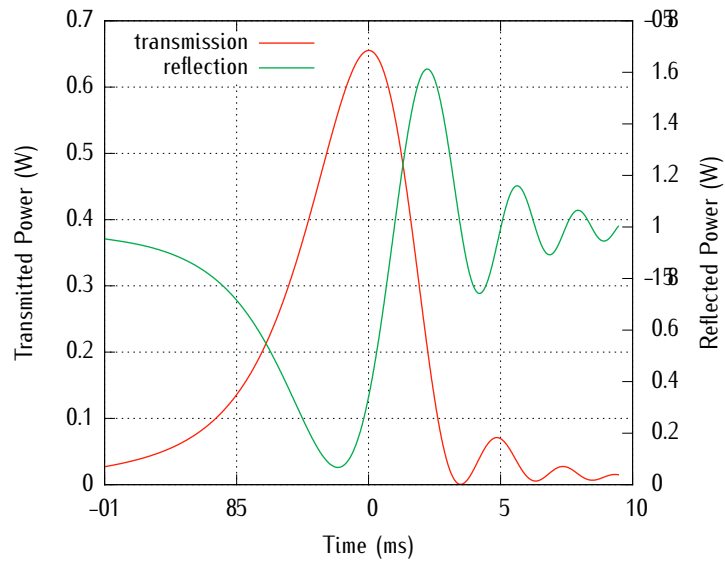


Figure 4.5.: The ringing effect from a high finesse cavity without absorption. The left axis shows the transmitted power, whereas the right axis shows the reflected power.

It is useful to just look at the difference of both scan directions. These plots show directly the hysteresis effect since the curve vanishes if there is no absorption inside the cavity. Figure 4.7 shows the difference plots for the same parameters as were used in the preceding plots.

4.6. Airy peak deformation in the presence of absorption

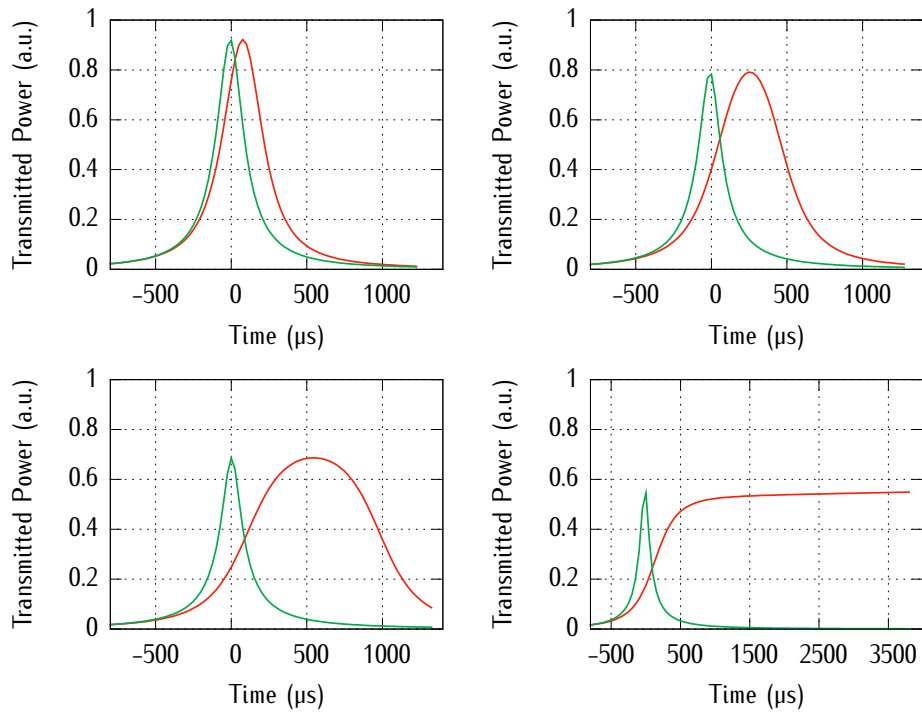


Figure 4.6.: Airy peaks in transmission from an absorbing cavity for different absorptions. As the absorption increases, the peaks get smaller in height and there is a hysteresis for the two scan directions. For lengthening the resonator (green curves) the peaks get narrower whereas the opposite is true for shortening the cavity (red curves). For the red curve in the bottom right plot the simulation is not valid anymore due to mode deformations of the beam.

4. Modelling thermal effects inside optical cavities

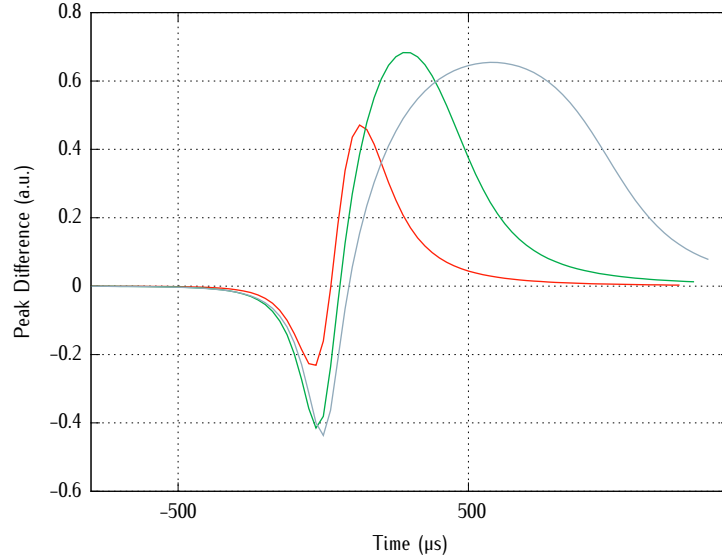


Figure 4.7.: The difference of the two scan directions is a direct measure of the hysteresis effect and therefore of the thermal aberrations. The curves belong to the first three Airy peaks that are shown in Figure 4.6.

4.7. Simulation parameter overview

In the last Section it was shown that there are a couple of parameters that enter the calculation. To reduce the parameter space, I will show in this Section how each parameter influences the result of the simulation. Therefore, we have to quantify the goodness of fit for a given measurement. This is done by using the variance V of the data given by

$$V = \frac{1}{N} \sum_{n=1}^N \left(x_n^{\text{theo}} - x_n^{\text{meas}} \right)^2, \quad (4.28)$$

where N is the number of data points and x is a vector containing the theoretical and experimental data, respectively. In minimizing this quantity, one finds the theoretical data that best describes the experimental data. The simplest method to find this minimum is to do a simple grid search where each parameter is scanned within a certain range and with a given number of steps. In Figure 4.8 you can see the contour plot of such a grid search, where only the two mirror reflectivities were scanned. The variance is minimized for the values $R_1 = 0.90579$ and $R_2 = 0.99819$. This minimum is given by $V_M = 1.35 \cdot 10^{-3}$. The yellow lines in the plot denote the points where the variance reaches two times the minimum V_M which I use as a measure of

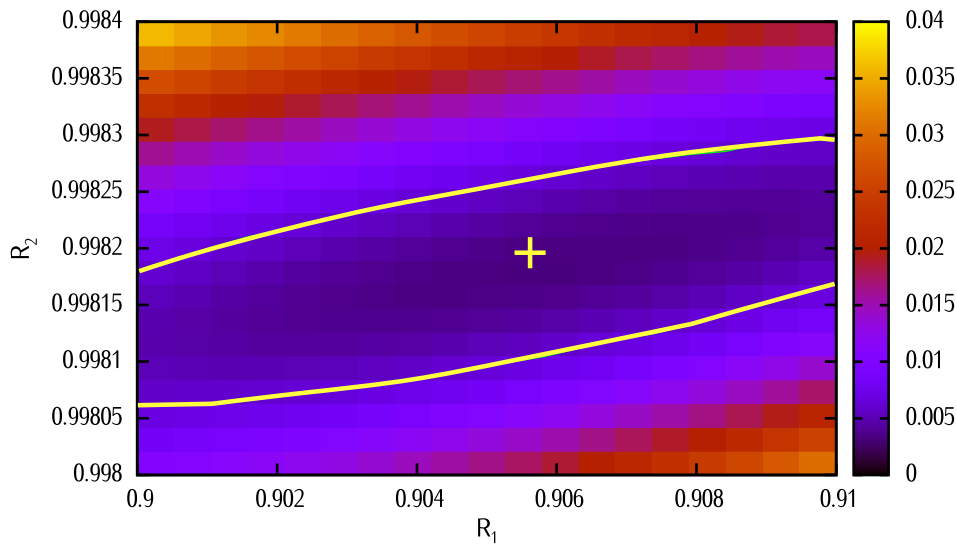


Figure 4.8.: This contour plot shows the result of a grid search for the scan of the two mirror reflectivities. The yellow ellipse indicates the doubling of the minimum variance and the cross marks the best fit values.

the tolerance for a parameter.

To find out how precise the parameters have to be known, I did a grid search for all the parameters involved. The starting point is the best fit to the measurement and from that, a single parameter is varied. Based on this analysis, the parameters can be split up into the following categories:

1. **Weak parameters** have only a very weak influence on the result.
2. **Strong parameters** have an influence on the calculation, but are normally known to a very high accuracy.
3. **Heavy parameters** are the most critical since they are not known very well and have a strong influence on the result.

Table 4.2 gives an overview over the categories including all the parameters. “Very weak” means that the variance is smaller than two times the minimum variance V_M even at deviations of $\pm 20\%$ from the parameters best fit value p_0 . The next category includes the parameters that show a variance of more than $2 V_M$ within the interval of $\pm 15\%$ around p_0 , whereas the heavy parameters show this variance within the interval of only $\pm 5\%$.

The corresponding plots are shown in Figure 4.9 for the weak parameters, Figure 4.10 for the strong parameters and Figure 4.11 for the heavy parameters. For all plots

4. Modelling thermal effects inside optical cavities

Weak parameters	(2 V_M deviation within $\pm 20\%$ around p_0)
n	index of refraction
R	radius of the substrate
s	air gap of the cavity
a _{th}	thermal expansion coefficient
k _{th}	thermal conductivity
dn/dT	temperature dependence of the refractive index
Strong parameters	(2 V_M deviation within $\pm 15\%$ around p_0)
NFSR _d	number of free spectral ranges (decreasing ramp)
lambda	vacuum wavelength of the light field
w0	waist size of the incident beam
cw	specific heat
rho	density
alpha	power absorption of the substrate
L	length of the substrate
Heavy parameters	(2 V_M deviation within $\pm 5\%$ around p_0)
R1, R2	mirror reflectivities
P	incident laser power
omega _s	scan frequency
NFSR _i	number of free spectral ranges (increasing ramp)

Table 4.2.: Overview of the three parameter categories.

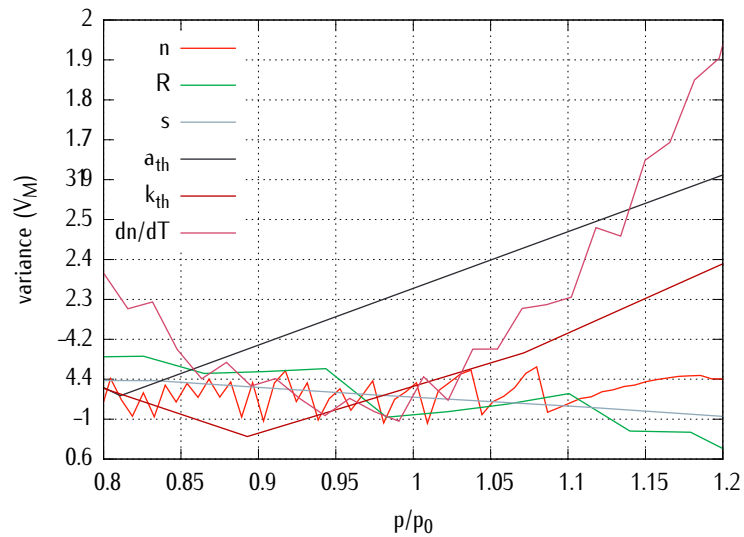


Figure 4.9.: Parameters that have only a very weak influence on the result.

4.7. Simulation parameter overview

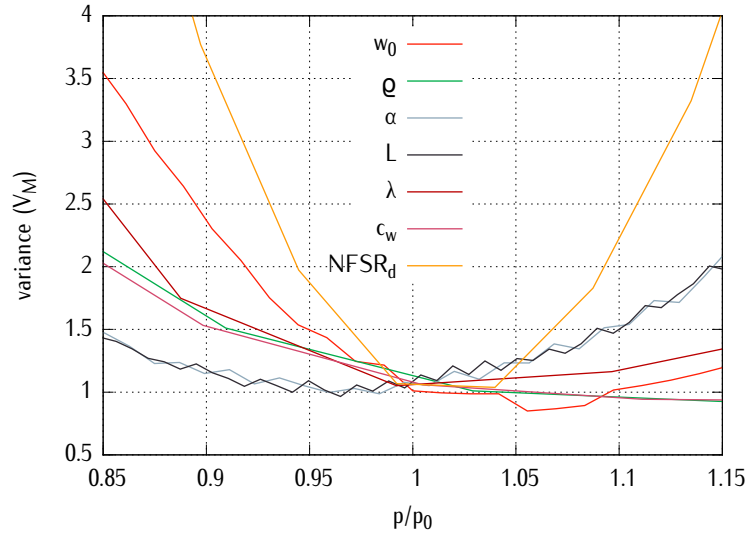


Figure 4.10.: Parameters that have weak influence on the result.

the variance is plotted in units of the minimum variance V_M and each parameter p is normalized to its best fit value p_0 . Note that the parameters α and L have roughly the same influence as $\partial n/\partial T$, although they just fall into the next category.

The reason why the number of FSR for each scan direction falls into two different categories is based on the hysteresis effect. As stated above, the peak gets broader when shortening the cavity, which means that in this case the temperature profile has more time to evolve. Hence the back-action on the light field is stronger compared to the opposite scan direction. Shortening the cavity length is equal to increasing the voltage of the piezo actuator leading to the stronger influence of the parameter NFSR_i compared to NFSR_d.

Since the scan frequency and the number of free spectral ranges that were scanned are normally known very well, the most critical parameters for the simulation are the mirror reflectivities R_1 , R_2 and the laser input power P . Since these are not known to the required accuracy, we can use the measurement of Airy peaks that don't show any hysteresis to determine them. The high influence of especially the mirror reflectivities on the simulation result means on the other hand that we can measure these quantities to a high precision with the help of the simulation. To achieve this, one uses a high scan frequency together with low input power. The missing hysteresis means that all material parameters vanish from the analysis and the only fitting parameters to the Airy peaks are the mirror reflectivities and the input power. Note that all parameters that are related to a substrate are present

4. Modelling thermal effects inside optical cavities

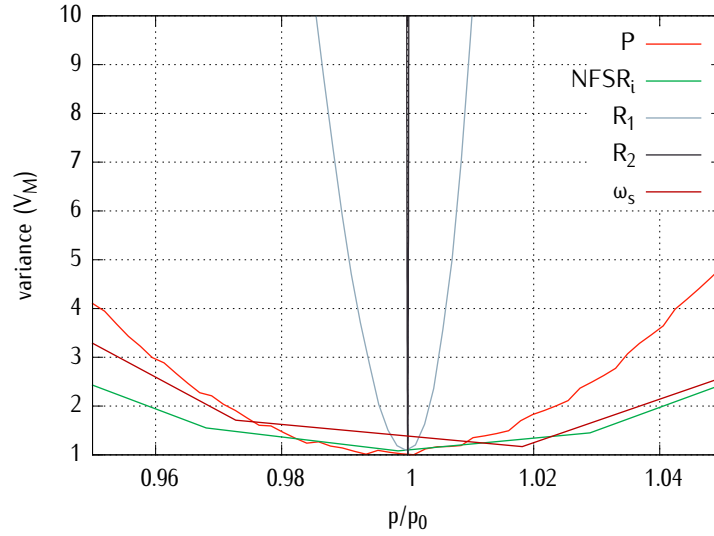


Figure 4.11.: Parameters that have a high influence on the result.

two times in the simulation, because we have the incoupling mirror as well as the intra-cavity substrate.

4.8. Determination of the optical absorption

To test the new measurement method we applied it to the absorption coefficient of lithium niobate doped with 7 mol% magnesium oxide [11]. The derived absorption was $\alpha = (5.9 \pm 0.9) \times 10^{-4}/\text{cm}$ which is in good agreement with a separate measurement of the absorption comparing the measured finesse of the cavity with the theoretical value as given by the mirror reflectivities specified by the manufacturer.

Figure 4.12 shows a schematic of the data that is needed for performing the analysis. We need the photodiode signals in transmission and reflection of the resonator for increasing and decreasing the piezo voltage. Furthermore at least one free spectral range of the cavity has to be scanned in order to determine the speed of the scanned mirror. Alternatively it is possible to generate frequency markers that are much smaller than a free spectral range by using an electro-optic modulator. Additionally, the ramp has to be recorded to determine the scan frequency. The measurements were performed by Jessica Steinlechner. The experimental setup is shown in Figure 4.13. The laser beam is coupled into the cavity consisting of a mirror with reflectivity $R_1 = 0.9$ and the back surface of a $\text{MgO}:\text{LiNbO}_3$ crystal with reflectivity of $R_2 = 0.998$. Since the material is a non-linear crystal of second order we detuned

4.8. Determination of the optical absorption

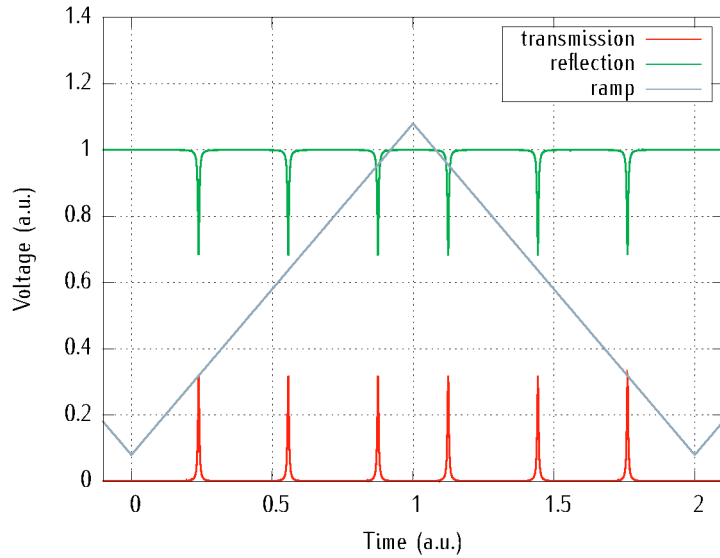


Figure 4.12.: Such a measurement is needed to determine the absorption. Together with the Airy peaks in transmission and reflection, the ramp frequency and the scan range as a multiple of the free spectral range have to be determined.

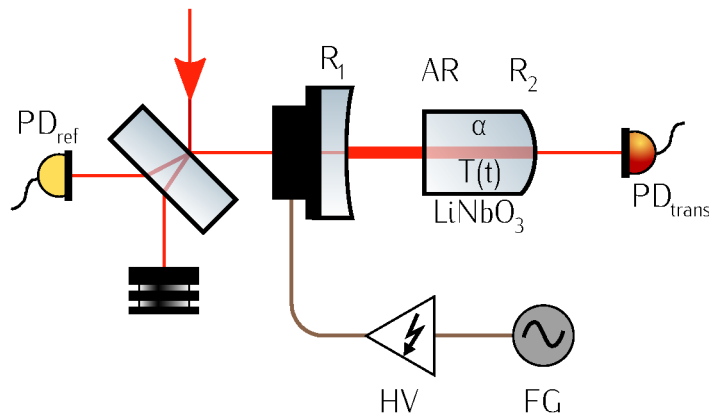


Figure 4.13.: Experimental setup for measuring the absorption of MgO:LiNbO₃. Because of the non-linearity of this material the temperature was detuned far away from the phase matching condition.

4. Modelling thermal effects inside optical cavities

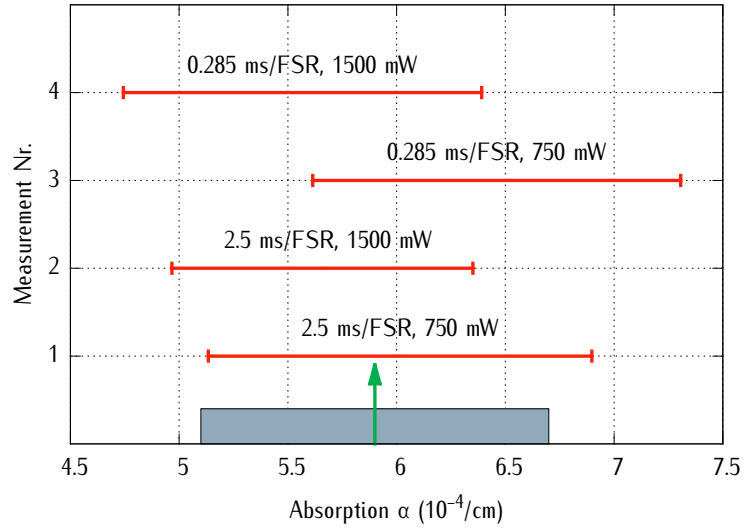


Figure 4.14.: Results of the measurements performed at the hemilithic SHG. The green arrow marks the average value of the absorption and the blue rectangle indicates the mean error.

the temperature well away from the phase matching condition to prevent any second harmonic generation. The incoupling mirror was then scanned by applying a high voltage to a piezo and the transmitted as well as the reflected field was measured using the photodiodes PD_{trans} and PD_{ref} , respectively.

To show the reproducibility of the method, the Airy peaks were measured for different scan frequencies and input powers. The results of the analysis of these measurements are shown in Figure 4.14. As you can see, all these measurements have comparable errorbars and the mean value of these measurements (green arrow) lays well inside each errorbar. The blue rectangle depicts the errorbar, averaged over all measurements.

To make a prediction of the sensitivity of our method, we consider the absorption measurement of crystalline silicon at a wavelength of $\lambda = 1550$ nm. This value has not been measured before, but data at shorter wavelength suggest an absorption coefficient smaller than $10^{-8}/\text{cm}$ [14]. Our simulation is based on a 6.5 cm long silicon sample inside a cavity of finesse 20000 pumped with 1 W of input laser power and an absorption of $\alpha = 10^{-8}/\text{cm}$. The reflectivities of the two cavity mirrors are assumed to be identical. Figure 4.15 shows the Airy peak difference of the two scan directions normalized to the input power in transmission and reflection. The scan velocity used in that simulation was $v_m = 2 \cdot 1550$ nm/s. Because of the high finesse

4.8. Determination of the optical absorption

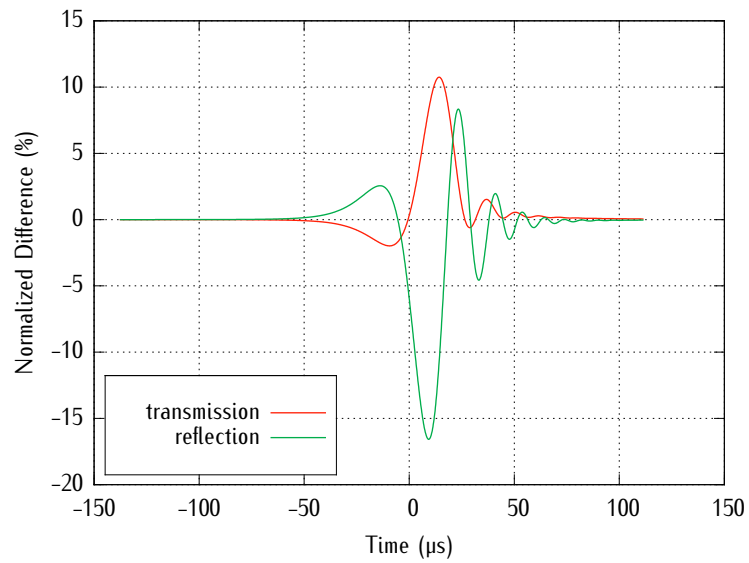


Figure 4.15.: Hysteresis as expected from a crystalline silicon cavity.

of the cavity, the Airy peaks show a rather strong ringing effect that can be seen in the hysteresis curve, too. For the chosen parameters we find a significant hysteresis of up to 16% of the input power.

5. An automated control system for the GEO 600 squeezer

This Chapter describes the automated control system for the GEO 600 squeezed light source. It is based on the LIGO Control and Data System (CDS) [41] and the Experimental Physics and Industrial Control System (EPICS) [42].

5.1. Introduction to the LIGO Control and Data System

The LIGO CDS was developed to digitally control large scale optical experiments like gravitational wave detectors. It is based on a real-time Linux system which runs on an x86 architecture multi-core CPU and uses PCI-X cards to interface the experiment. The computer that runs this real-time system and implements the digital controllers is called the front-end. Together with the so-called frame builder, which is responsible to permanently store the data to disk and also to provide this data on the network, these two components make up the real-time part of the system. Note, that the frame builder does not have to be an independent computer but may be installed on the front-end computer as well.

Ordinary Gigabit Ethernet connections are used to build a private network for each experiment which may contain multiple front-ends and frame builders. Additionally, there are workstations in this network that are not real-time capable but provide the tools that the user needs to develop the digital control software, access the data from the frame builder and operate the experiment. To configure the real-time models and to implement control algorithms that do not require fast execution, the EPICS *channel access protocol* (CA) is used. The EPICS software originates in the high energy physics community and was developed to control particle accelerators which have a huge number of channels that have to be controlled without the need for hard real-time.

The combination of these software components makes it possible to transfer the two main tasks for controlling an optical experiment containing multiple components to the digital world. The first task is to design controllers for each component that do a stabilization of that part independently of all the other parts on the optical table (e.g. locking the length of an optical resonator). These controls often have to be relatively fast and are realized by designing a digital filter that runs on the front-end computer as a real-time kernel module. The CDS currently provides control band-

5. An automated control system for the GEO 600 squeezer

widths of a few kHz. As a rule of thumb, the bandwidth is only one tenth of the sampling rate which is in this case 64 kHz.

On the other hand, there is the task of locking the components in a given sequence. This task is usually done by the person running the experiment by manually operating some knobs and switches within the electronics rack. In the digital world these actions are commonly replaced by operating a graphical user interface (GUI) for the experiment's control on the workstation computer. For the CDS these screens can be created by using the Motif Editor and Display Manager (Medm) which is an easy to use GUI designer. In many cases the sequential locking has to be automated to provide a 24/7 control of the experiment. This can be realized by using one of the scripting interfaces to the EPICS channel access protocol. This protocol uses so-called *process variables* (PVs) which represent a specific EPICS channel. These PVs are managed in a database by *Input/Output Controllers* (IOCs) that can be accessed over a network connection. It is allowed and also common to run multiple IOCs within a single network.

5.2. Overview of the GEO 600 squeezed light source

In this Section I will give a brief overview of the GEO 600 squeezed light source without going into the details of the experimental setup. These can be looked up in [6]. Figure 5.1 shows a schematic layout of the GEO 600 squeezed light source. Most of the light power from the main laser is used to pump a second harmonic generator (SHG) to produce the pump field for the optical parametric amplification (OPA). The harmonic field is then sent towards a filter cavity (MC₅₃₂) that provides a well defined TEM₀₀ mode for the pump beam. To reduce power fluctuations of the field, a Mach-Zehnder interferometer (MZ) was placed in front of the mode-cleaner. The intensity-stabilized harmonic mode is then used to pump the OPA cavity which produces vacuum squeezed states of light at the fundamental wavelength.

These squeezed states are sent towards the dark port of the GEO 600 gravitational wave detector and increase its sensitivity in the high-frequency regime of the detection band. Alternatively, the beam can be sent to a homodyne detector for diagnostic purposes. The local oscillator for the detection is provided by tapping off some light power from the main laser which is then filtered by a mode-cleaning cavity (MC₁₀₆₄).

There are two other lasers present on the squeezing breadboard. Since we deal with vacuum squeezed states of light, it is not possible to get any error signals from this field. To avoid technical noise that would make it impossible to detect squeezing within the detection band, these lasers are frequency shifted with respect to the main laser. Additionally, one of these lasers is orthogonally polarized with respect to the others. With this setup it is possible to coherently control the length of the OPA cavity as well as the phase of the harmonic pump beam which determines the angle of

5.2. Overview of the GEO600 squeezed light source

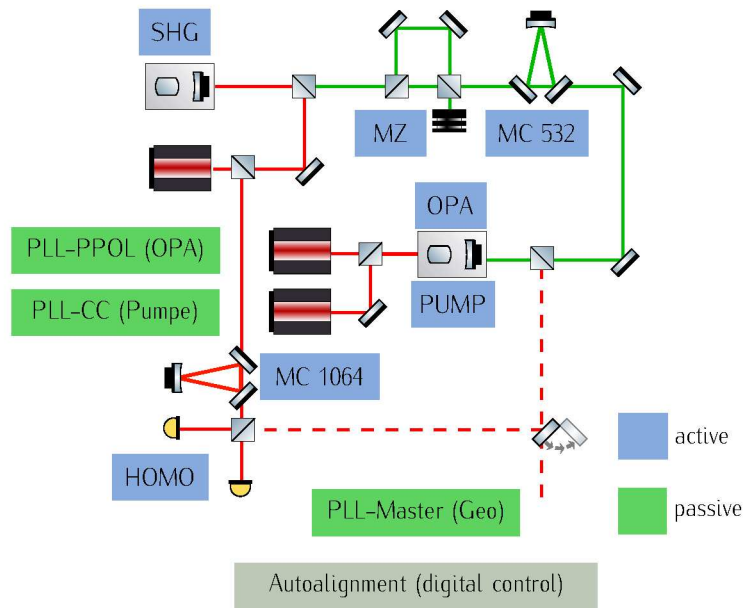


Figure 5.1.: Overview of the GEO 600 squeezed light source. The named components have to be locked in sequence. Active components can be locked and unlocked on purpose, whereas the passive components just return a status of their current lock state. Note, that the flip mirror is not physically present in the experiment, but indicates the two different setups at the cleanroom of the AEI and the cleanroom at Ruthe. The auto-alignment of the squeezed mode to the mode of GEO 600 will be implemented using digital controllers.

5. An automated control system for the GEO 600 squeezer

the squeezing ellipse with respect to the master laser of GEO 600. Of course, all these lasers have to be phase-locked to each other, which is done by using commercially available phase locking loops (PLLs).

All PLLs are denoted to be passive, which means that they can not be locked actively. There is only a switch for locking the device and a status can be gained from each PLL. Therefore, you have to wait until these components lock which may take several minutes.

The flip mirror that can be seen in the schematic is physically not present on the breadboard. This component stands for the two modes of operation, where the diagnostic mode was performed within the clean rooms of the AEI. After the transport to the GEO 600 detector, this diagnostic mode was dropped because the performance of the squeezed light source can be monitored by looking at the spectrum of the gravitational wave detector.

For the GEO 600 squeezed light source it was decided to stick to the analog electronics to control each component on the optical table. The main reason for this is that the experiment needs control bandwidth of up to 10 kHz, which is not available by using the CDS system as it is implemented now (see Section 5.1).

Nevertheless, the squeezer uses a complete CDS system for future migration to digital control of at least some parts. One thing that will be realized using digital control will be the auto-alignment of the squeezer beam to the GEO 600 mode. Therefore, the task for the GEO 600 squeezed light source was to implement the sequential locking which is based on EPICS. On top of this a fully automated generation of system logs should be provided together with a notification system. These tools should help in finding problems in case of a misbehavior of the experiment. The performance of the squeezer as well as some statistics about the duty-cycle and the amount of re-locking attempts for each component should be gained. The next Section discusses a general approach to perform sequential lockings by using a *Python* interface to the EPICS channel access protocol.

5.3. A generic sequential control solution

Within the CDS there is no general solution to do sequential lockings. There are a lot of different ways of how this can be done, but all have in common that they are based on the EPICS layer. A look on the EPICS web site [43] reveals a multitude of interfaces for the EPICS channel access protocol. Widely used are command line tools like *ezca* that can be invoked from a shell script for example. Other solutions use higher-level programming languages for accessing the *process variables* (PVs) that represent a certain data channel within the EPICS channel access protocol. Because of the requirements for the GEO 600 squeezing control application stated further above, we decided to use a *Python* interface to the EPICS channel access protocol. This scripting language has several benefits. First, it is relatively easy to learn even

5.3. A generic sequential control solution

for non-programmers and because of the dynamical typing and the huge amount of modules that can readily be used, it is very efficient for developing applications. Another reason is the object oriented nature of the language which makes it easy to map physical components to *Python* classes and leads to a reusable and well designed code structure.

This Section presents a general approach to implement sequential locking for an experiment that is controlled using the CDS and EPICS. It is based on the *EpicsCA Python* interface that was written by Matthew Newville [44]. The most important object that is defined by the interface is represented by the process variable (*PV*) class. The following code snippet shows the fundamental usage of this class from within a *Python* shell.

```
>>> from EpicsCA import PV
>>> freq = PV('G1:GHF-SHG_RAMP_FRQ')
>>> freq = 3.2
>>> freq
3.2
```

After the class has been imported from the *EpicsCA* module the constructor is called with the name of an EPICS channel as argument. In the example the scan frequency of the second harmonic generation cavity is accessed. To manipulate the value of the channel, the instance of the *PV* class can directly be assigned a number. This instance is also used for reading the current value. This very simple interface to the process variables is realized by using the *Python property* construct. The idea behind it is to map functions for setting and getting a value to an object that behaves like an ordinary variable for the user, while in the background much more happens (in this case the connection to the IOC has to be created for example).

The idea for implementing the sequential locking scheme is to first map each component that has to be controlled to a *Python* object. These objects hold some instances of the *PV* class to access the EPICS channels that are needed in order to lock the part. Then, each component is added to a list which contains the right sequence and which is repeatedly iterated through to keep all the components in lock. As said in the previous Section, for the GEO 600 squeezed light source the components that are part of this list are in sequence

1. GEO 600 master PLL (*master_pll*)
2. PLL for coherent control of the squeezing angle (*cc_pll*)
3. PLL for the OPA cavity length control (*ppol_pll*)
4. OPA cavity length control (*opa*)
5. SHG cavity length control (*shg*)

5. An automated control system for the GEO 600 squeezer

6. Mode-cleaner for the harmonic mode (*mc532*)
7. Mach-Zehnder interferometer (*mz*)
8. Phase of the harmonic pump beam (*pump*)
9. Mode-cleaner for the local oscillator (*mc1064*)
10. Homodyne detection angle (*homo*).

The last two components only have to be locked if the squeezer is run in diagnostics mode. The names that are given in brackets are the names of the instances that represent the controller objects within our *Python* framework. The list of components is represented by an immutable array-like structure (*tuple*) and is defined by the variable *PARTS* within the configuration file *parts.py*. For the GEO 600 squeezer it reads

```
PARTS = (master_pll, cc_pll, ppol_pll, opa, shg, mc532,\
        mz, pump, mc1064, homo)
```

The sequential lock algorithm is depicted in Figure 5.2. After an initialization phase in which all components are unlocked in reverse order, the algorithm enters an infinite loop that repeatedly scans the list of components for a part that lost lock. If such a part is found, the code searches for the first component that is not locked. This is important because it may happen that the loss of lock of an earlier component causes the unlocking of the current component. The next step is to reversely unlock all the parts that appear later in the sequence. Finally, all components can be locked in sequence again, starting from the component that caused the interruption of normal operation.

Such a general description of the locking procedure requires that all components share a common interface. This means that each class that represents a physical component has to provide the functions that are used by the sequential lock algorithm. Therefore the module *Controller.py* defines a class (also named *Controller*) that provides the methods and variables that are listed in Table 5.1. All the objects that are added to the *PARTS* list have to be derived from this main class. The functions that show up in Figure 5.2, namely *lock()*, *unlock()* and *islocked()* are readily provided by this controller class. The derived classes only have to implement the abstract functions *_tryToLock()* and *_tryToUnlock()* which perform a single attempt to lock or unlock a component. Within these functions the member variable *_islocked* has to be set correctly, corresponding to the state of the component. The *lock()* method calls the method *_tryToLock()* until the component is locked or the number of lock attempts given by the member variable *_attempts* is exceeded. Analog to this procedure the method *unlock()* calls the function *_tryToUnlock()* until the component is successfully unlocked. The variable *_lockID* is set automatically, being zero if a

5.3. A generic sequential control solution

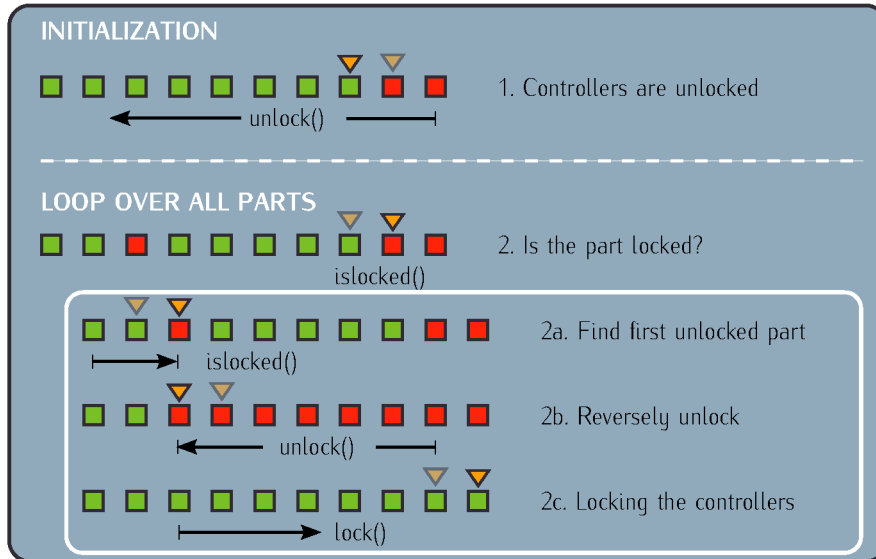


Figure 5.2.: Schematic of the automated lock algorithm. The green boxes indicate locked components whereas the red ones correspond to unlocked components. The transparent triangle marks the previous, the opaque one the current position in the list of components. The arrows mark the range and the direction in which a method call is applied.

Object	Description	Type
lock()	lock the controller	method
unlock()	unlock the controller	method
islocked()	returns the lock status	method
_tryToLock()	try _attempts times to lock the controller	abstract
_tryToUnlock()	try _attempts times to unlock the controller	abstract
_name	name of the controller	string
_islocked	lock status	bool
_lockID	ID for debugging purposes	integer
_attempts	number of lock attempts	integer
_ispassive	whether the controller can actively be locked	bool

Table 5.1.: Members and methods as defined by the controller class in the module *Controller.py*. This class defines the interface for all controller objects. Other classes have to be derived from this class.

5. An automated control system for the GEO 600 squeezer

controller could not be locked or unlocked and otherwise it is the position of the component within the *PARTS* variable if the locking was successful and the negative position if the unlocking was successful. This variable is only used for debugging purposes and to implement *unit tests* for the lock algorithm (see below). In the case that a request to lock or unlock a component was not successful, the code tries to unlock all components and then restarts the sequential lock algorithm after a user specified number of seconds. As this situation has to be considered a severe failure of either the software or the experimental setup, an email is sent to the operators at every restart.

For the GEO 600 squeezer several controller classes had to be derived from the main controller class. These are

PassiveController This class is the most simple one. It represents the PLLs that are used on the squeezer breadboard and can only wait for a specified number of seconds for the component to lock. Unlocking these components can not be done at all. Therefore the *_ispassive* member is set to true.

RtLengthController These objects have access to various EPICS channels that are used to interface the real-time code and initiate the lock of a single component.

MC532 Derived from *RtLengthController* for locking the harmonic mode-cleaner. This extra class is needed, because the Mach-Zehnder interferometer has to be tuned to maximum transmission before the *MC_532* can be locked.

StubController Controller that mimics a physical component. This class is used for implementing unit tests for the sequential lock algorithm. It uses the class *StubPV* that behaves just like the *PV* class except for the process variables being local variables that have no EPICS channel attached to it. This makes it possible to run the tests without having the computer connected to an IOC.

In addition to the controller classes there is another class (*SequentialLock*) that starts and stops the sequential lock algorithm. To make sure that only one instance of this class can be run at the same time, the class was implemented using the singleton pattern [45]. Additionally the process id is written to a lock file and is used to check whether another process is running. In this case the application will refuse to start. If the launch was successful, the components are initialized and the application enters the infinite loop as described earlier. This loop can be interrupted by sending the signal SIGINT to the process.

Each of the classes that were mentioned so far are capable of writing log messages to a file. This is realized by using the logging mechanism that *Python* readily provides in form of the *logging module* [46]. The logging handler that is used is the so-called *rotating log handler*. It works by writing to a file until a specified file size is reached. The handler then makes a copy of this file, deletes all entries from the original file and

5.4. Using the sequential control interface

```
1 2010-03-17 16:15:15,376 - INFO - Initializing (unlocking all controllers) ...
2010-03-17 16:15:18,680 - INFO - Initializing finished
2010-03-17 16:15:18,680 - INFO - Entering automatic control loop
2010-03-17 16:24:33,055 - WARNING - 'Mach-Zehnder' has to be relocked (hv was 2.295987e+03)
5 2010-03-17 16:24:33,595 - INFO - 'Phase lock' unlocked after 1 tries
2010-03-17 16:24:34,139 - INFO - 'Mach-Zehnder' unlocked after 1 tries
2010-03-17 16:24:35,463 - INFO - 'Mach-Zehnder' locked after 1 tries
2010-03-17 16:24:36,539 - INFO - 'Phase lock' locked after 1 tries
2010-03-17 16:24:38,343 - CRITICAL - 'Mach-Zehnder' won't stay in lock for more then 10 seconds
10 2010-03-17 16:24:38,343 - WARNING - 'Mach-Zehnder' has to be relocked (hv was 1.102706e+03)
2010-03-17 16:24:38,883 - INFO - 'Phase lock' unlocked after 1 tries
2010-03-17 16:24:39,427 - INFO - 'Mach-Zehnder' unlocked after 1 tries
2010-03-17 16:24:40,751 - INFO - 'Mach-Zehnder' locked after 1 tries
2010-03-17 16:24:41,826 - INFO - 'Phase lock' locked after 1 tries
15 2010-03-17 16:27:56,154 - INFO - HV range of 'Phase lock' exceeded (was -1.695055e+02)
2010-03-17 16:27:56,694 - INFO - 'Phase lock' unlocked after 1 tries
2010-03-17 16:27:56,954 - WARNING - 'OPA' has to be relocked (hv was 1.142514e+03)
2010-03-17 16:27:57,494 - INFO - 'Phase lock' unlocked after 1 tries
2010-03-17 16:27:58,038 - INFO - 'Mach-Zehnder' unlocked after 1 tries
20 2010-03-17 16:27:58,582 - INFO - 'MC 532' unlocked after 1 tries
2010-03-17 16:27:59,126 - INFO - 'SHG' unlocked after 1 tries
2010-03-17 16:27:59,670 - INFO - 'MC 1064' unlocked after 1 tries
2010-03-17 16:28:00,214 - INFO - 'OPA' unlocked after 1 tries
2010-03-17 16:28:11,475 - CRITICAL - Unable to lock 'OPA' (attempted 10 time(s))
25 2010-03-17 16:28:11,479 - INFO - Shutting down (unlocking all controllers) ...
2010-03-17 16:28:12,019 - INFO - 'Phase lock' unlocked after 1 tries
2010-03-17 16:28:12,563 - INFO - 'Mach-Zehnder' unlocked after 1 tries
2010-03-17 16:28:13,107 - INFO - 'MC 532' unlocked after 1 tries
2010-03-17 16:28:13,655 - INFO - 'SHG' unlocked after 1 tries
30 2010-03-17 16:28:14,203 - INFO - 'MC 1064' unlocked after 1 tries
2010-03-17 16:28:14,746 - INFO - 'OPA' unlocked after 1 tries
2010-03-17 16:28:14,750 - INFO - Shutting down finished
2010-03-17 16:28:14,954 - INFO - Restarting in 60 seconds
2010-03-17 16:29:14,951 - INFO - Initializing (unlocking all controllers) ...
```

Figure 5.3.: Example of a log file generated by the sequential lock algorithm. This file is taken from an early run of the GEO 600 squeezed light source as it was still located in the clean-room of the AEI.

then starts writing the log file again. The number of backup files can also be specified. Log messages can simply be generated by calling one of the methods *info(msg)*, *warning(msg)*, *error(msg)*, *debug(msg)* or *fatal(msg)* on the logging instance. The latter can be created by calling

```
logging.getLogger(LOG_NAME),
```

where *LOG_NAME* is the user defined name of the log handler. An example of the resulting log files can be seen in Figure 5.3.

5.4. Using the sequential control interface

The interface for the sequential lock algorithm has to be configured by editing the three configuration files *config.py*, *parts.py* and *parts_init.py*. The first one is used to define general settings whereas the other files are used to define the controller classes.

Figure 5.4 shows the content of the general configuration file *config.py*. The first settings are related to the previously mentioned log mechanism. Here you can

5. An automated control system for the GEO 600 squeezer

```
1  """General configuration of the sequential locking interface."""
import logging
import logging.handlers
import os
5
home = os.getenv('HOME')
LOG_NAME = 'sco'
LOG_FILE = home + '/sco-working/log/sco.log'
LOG_LEVEL = logging.DEBUG
10 LOG_FORMAT = '%(asctime)s - %(levelname)s - %(message)s'
LOG_SIZE = 1e6
LOG_BACKUP = 5

SCO_LOCK_FILE = home + '/sco-working/log/sco.pid'
15 DUMP_LOCK_FILE = home + '/sco-working/log/dump.pid'

# seconds to wait before restarting the autolock
restart_delay = 60

20 # Epics sleep time is needed to make sure the channels are set
EPICS_SLEEP = 0.5

# initialize the log handling
logger = logging.getLogger(LOG_NAME)
25 handler = logging.handlers.RotatingFileHandler(LOG_FILE,
maxBytes=LOG_SIZE, backupCount=LOG_BACKUP)
formatter = logging.Formatter(LOG_FORMAT)
handler.setFormatter(formatter)

30 logger.addHandler(handler)
logger.setLevel(LOG_LEVEL)

# this function replaces the SMTPHandler which is not working
def sendmail (subject, msg_command, attachments = None):
35     pass
toaddrs = 'nico.lastzka@aei.mpg.de'
toaddrs += ' christian.graef@aei.mpg.de'
toaddrs += ' henning.vahlbruch@aei.mpg.de'
40 toaddrs += ' alexander.khalaidovski@aei.mpg.de'

if attachments == None:
mailcmd = "%s | mutt -s '%s' %s" % (msg_command, subject, toaddrs)
else:
45 mailcmd = "%s | mutt -s '%s' -a %s -- %s" % (msg_command, subject, attachments, toaddrs)

os.system(mailcmd)
```

Figure 5.4.: The configuration file config.py.

5.4. Using the sequential control interface

```
1 ##### FILE -- parts.py #####
# sequential subsystem definition
mc1064 = RtLengthController(name = 'MC 1064',
5   lock_once = PV('G1:GHF-MC1064_TOGGLE_LOCK'),
   thresh_acq = PV('G1:GHF-MC1064_THRESH_ACQ'),
   thresh_inLock = PV('G1:GHF-MC1064_THRESH_INLOCK'),
   freq = PV('G1:GHF-MC1064_RAMP_FRQ'),
   amp = PV('G1:GHF-MC1064_RAMP_AMP'),
10  status = PV('G1:GHF-MC1064_ISLOCKED'),
   reset_output = PV('G1:GHF-MC1064_RESET_OUTPUT'),
   toggle_unlock = PV('G1:GHF-MC1064_TOGGLE_UNLOCK'),
   delay = PV('G1:GHF-MC1064_DELAY'),
   hvmonitor = PV('G1:GHF-MC1064_HVAMP_MON_OUT16'),
15  autolock = PV('G1:GHF-MC1064_AUTOLOCK'))

master_pll = PassiveController(name = 'Master PLL',
   status = PV('G1:GHF-MASTERPLL_OUT16'))

20 execfile('parts_init.py')

PARTS = (master_pll, cc_pll, ppol_pll, opa, mc1064, shg, mc532, mach, pump, homo)

-----
25 ##### FILE -- parts_init.py #####

# initialize all values for the controllers
mc1064.freq = 1
30 mc1064.amp = 25000
mc1064.thresh_acq = 630
mc1064.thresh_inLock = 120
mc1064.hvmin = -140
mc1064.hvmax = 4700
35 mc1064.delay = 1000

master_pll.thresh_inLock = 6000
```

Figure 5.5.: Part of the files `parts.py` and `parts_init.py` that demonstrates the main configuration issues that can be performed by editing these files.

change the name, debug level and format as well as the file size and number of backups for the rotating log handler. The next setting is the file where the process id will be stored to realize a locking mechanism. The next entry is the delay for automatically restarting the algorithm after an error occurred followed by the `EPICS_SLEEP` time that defines the number of seconds to wait until the code continues after an EPICS channel was set. This ensures that the value of a channel was changed successfully. At the end of the file the function `sendmail()` is defined which is called whenever a severe problem occurred that forces the code to restart the sequential control. The list of recipients is defined by the variable `toaddrs`.

The other configuration files `parts.py` and `parts_init.py` are used to define the controllers and connect them to the corresponding EPICS channels. It is also possible to set default values for the members of the controller classes in here. In Figure 5.5 you can see a part of each file. The file `parts.py` is used to instantiate the controller classes and to define the sequence in which the controllers should be locked. In the example that you see in the figure, the fundamental mode-cleaner is defined as an `RtLengthController`. The constructor takes as argument the EPICS channels that are

5. An automated control system for the GEO 600 squeezer

needed for the controller to work properly. Another controller is the PassiveController that is used for the PLLs in this case. Note that this controller is pretty simple and just needs a single EPICS channel to judge whether the component is in lock.

The last configuration file is executed from within the file *parts.py* using the *Python* command *execfile()*. The advantage of this splitting is that the user may change the member values defined in *parts_init.py* at run time of an application and then reread the configuration on the fly. The code snippet of this file shows the definition of various parameters as for example the frequency and amplitude of the ramp for the MC₁₀₆₄. The file *parts.py* can not be read at runtime since this would create new instances of the components. At this stage the controller classes can be used interactively from within a *Python* shell. An example session for locking the fundamental mode-cleaner may look like this:

```
>>> from parts import *
>>> mc1064.freq          # print the current ramp frequency
1.0
>>> mc1064.freq = 10.0 # change the frequency to 10 Hz
>>> mc1064.islocked()  # see whether the component is locked
False
>>> mc1064.lock()      # initiate a lock sequence
>>> mc1064.islocked() # confirm that the lock was successful
True
>>> mc1064.unlock()   # unlock the component again
```

To start the automated sequential lock control, another *Python* script is used. The command line usage of this script is as follows

```
SequentialLocking.py start | stop | restart | status.
```

The script is called by using the *nohup* application so that it is safe to log out of the workstation without quitting the sequential locking process.

5.5. Controlling the GEO 600 squeezer

This Section explains the details of the software implementation for the GEO 600 squeezed light source. Beneath the sequential lock algorithm introduced in the preceding Section, there are several scripts as well as a graphical user interface (GUI) designed for controlling the squeezer.

All this software is located in a Git repository and made available via NFS (network file system) on both the workstation and the front-end computer. The clone URL for this repository is *git@mclane:~/sco.git*. There is also a working copy under *\$HOME/sco-working* that is also distributed via NFS. All the software is developed and executed from within the latter folder. The repository consists of the following files and folders:

5.5. Controlling the GEO600 squeezer

Member name	description
freq	frequency of the ramp
amp	ramp amplitude
thresh_acq	acquisition threshold
thresh_inLock	inlock threshold
hvmin	minimum of the HV range
hvmax	maximum of the HV range
delay	switch delay

Table 5.2.: Parameters that can be set within the configuration file `parts_init.py`. Note that not all of these parameters are available for all the components.

ghf.mdl The Simulink model which has to be compiled to generate the real-time code.

c-code This folder includes the customized real-time code for locking and ramping of the components. These files are inserted by the Simulink model as C code blocks and are automatically compiled when using the `rtmodule` shell script.

ChannelList_ghf.txt This file holds the channel names and the rates of the channels that are to be acquired.

doc Some documentation about the usage.

log The files for logging and locking of the sequential algorithm are written to this directory.

medm Custom Medm screens that are used for diagnostic purposes and to manually lock single components.

pysco Within this folder the *Python* classes for the sequential lock algorithm can be found. It also contains all the configuration files and the operator GUI.

scripts Several utility scripts for controlling and debugging the squeezed light source.

The real-time kernel module is generated from the Simulink model `ghf.mdl` using the `rtmodule` script as described in Appendix A.4. This shell script reads the file `ChannelList_ghf.txt` to set the channels that are to be acquired and automatically compiles the custom C code that resides within the C code folder.

The configuration files for the lock algorithm were already described in a previous Section. Table 5.2 shows the list of all the parameters that can be set within the file `parts_init.py` for the controller classes used for the squeezer. There are two thresholds that can be set, realizing a *Schmitt-Trigger*. The first (`thresh_acq`) determines at which photodiode level the lock switches should be turned on, whereas the second

5. An automated control system for the GEO600 squeezer

(*thresh_inLock*) is used as the criterion whether the controller is in lock. The high voltage range given by *hvmin* and *hvmax* is used to force a relock for a component if its dynamical range is about to be exceeded. After a relock the components are usually far away from the borders of the actuator range since the search for an operating point is always started right in the middle of this range. The delay parameter sets the delay between the switches when turning on the lock.

The command line control of the squeezed light source is the same as already described in the last Section. It has to be executed from within the *pysco* folder. Especially for the squeezer there is an additional *Python* script (*dump_spectra.py*) within the *pysco* directory which is used to start and stop the automatic generation of the squeezing spectra when running in diagnostic mode. The usage is as follows

```
dump_spectra.py start | stop | restart | status.
```

This means that you have to give at least one argument on the command line which is either one of *start*, *stop*, *restart* or *status*. Like for the start of the sequential locking interface this process is also started using the *nohup* application. The *nohup* output is written to the log folder. The *dump_spectra.py* script uses the *Python* interface to the NDS which is explained in Appendix A.2. The configuration of this script is done directly in the file *dump_spectra.py*. Table 5.3 shows all the parameters that can be adjusted for this process.

parameter	default	description
channelname	G1:GHF-HOMO_SQZMON_OUT_DAQ	Homo PD AC channel
samplefreq	32768.0	sample frequency of the channel
duration	0.1	length of the time series for a single spectrum
dt	900	generate spectrum every dt seconds
send_every	4*3600	send an email every send_every seconds
f1	1./duration	start frequency
f2	10e3	end frequency
navg	1000	number of averages
abspath	\$HOME/sco-working/data/specs	path where the results will be stored

Table 5.3.: Configuration parameters of *dump_spectra.py* script that is used to acquire the squeezing spectra when running in diagnostic mode.

The data will be stored in a folder structure under the path given by *abspath*. There you will find the folders *dat*, *eps* and *gif* for the raw data, eps images and

5.5. Controlling the GEO600 squeezer

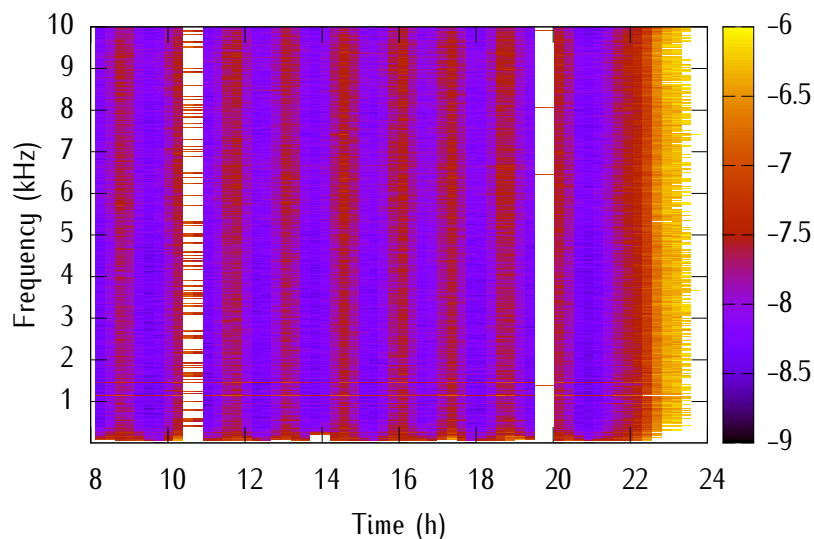


Figure 5.6.: Example of a squeezing map that was automatically generated by the *dump_spectra.py* script. It shows the performance of the squeezer over 16 hours.

gif images, respectively. Each of these folders contains the data in subfolders of the format *Year/Month/Day* and each filename consists of the time the data was taken. Every time a new spectrum is created, the files *animation.gif* and *histogram.eps* are updated. At the end of the day, these files contain an animation of the spectrum as well as a 2D map of the squeezing versus frequency and time. These two files are also sent via email to get an overview of the squeezer performance. Figure 5.6 shows an example of a squeezing map. These kind of plots show the squeezing spectrum over time. In the example the squeezer was controlled for approximately 16 hours, producing a squeezing between -7.5 dB and -8.5 dB. The period of the oscillation in the squeezing strength is due to the air conditioning in the clean room. Three times the squeezed light source produced less than -6 dB of squeezing which was due to the second harmonic generation cavity drifting around its operating point.

Within the folder *scripts* there are several utility scripts that can be used for initialization, debugging and statistical purposes. These scripts are:

5. An automated control system for the GEO 600 squeezer

dutycycle.py

This script will print out the duty-cycle for each component and the total duty-cycle within a certain period of time.

```
usage: dutycycle.py start_time stop_time
```

The times have to be given in the format “2010-03-23 15:04:48”.

relocks.py

This script will print out the relock statistics for each component.

```
usage: relocks.py start_time stop_time
```

The time format is the same as for the duty-cycle script.

fit_shotnoise.gp

This script is used to fit a polynomial to the measured shot noise. This curve can then be subtracted from the squeezing channel to get the correct dB scale. You first have to get the spectrum of the shotnoise (e.g. using *CDSplot*) and then save it under *shot.txt*. This file is then read by the *Gnuplot* script to make the fit. The coefficients used in the fit can then be copied to the method *shotnoise()*.

master_switch.py

The script toggles between manual and autolock mode. Use it if you want to lock the squeezer in the lab without disconnecting the whole CDS system.

```
usage: master_switch.py man | auto
```

setFilterGains.sh

Set the filter gains properly after a front-end restart.

```
usage: setFilterGains.sh
```

throw_out_of_lock.sh

Throw a certain component out of lock. Useful to test the autolock functionality.

```
usage: throw_out_of_lock.sh component
```

Component may be one of *homo*, *mc1064*, *mc532*, *mach*, *pump*, *opa* or *shg*.

5.6. An operator GUI using the Qt libraries



Figure 5.7.: Screenshot of the operator GUI for controlling the GEO 600 squeezed light source.

5.6. An operator GUI using the Qt libraries

To especially facilitate the manual control of the squeezer, a graphical user interface (GUI) was developed. Since the lower levels of the control software were written in *Python*, this GUI was developed by using the *Python* interface to the *Qt4* graphical library [47]. Thereby, the *QtDesigner* was used to build the GUI. This tool is roughly comparable to *Medm* which is normally used to build user interfaces for the CDS.

A screenshot of the operator GUI is depicted in Figure 5.7. The window of the GUI is divided into three parts. On top, there are three buttons to start and stop the scripts for the automated locking, the dumping of the squeezing spectra and the real-time kernel module. On the left side there are three LED like status fields that indicate whether the passive controllers (the PLLs) are locked.

In the middle of the window there is a panel for manually controlling the squeezed light source. This includes the locking and unlocking of each component as well as to turn on and off the ramp individually. Right below of the ramp switches there are two input fields where the user can specify the ramp's amplitude and frequency. These fields are read when pressing any of the ramp-on buttons and therefore specify

5. *An automated control system for the GEO 600 squeezer*

the values for the currently invoked ramp. On the left side there are further buttons to open and close the shutter and to trigger the auto-alignment of the squeezed beam which should be done by using another real-time code on a separate front-end. These latter two components are not implemented yet.

The series of buttons on the bottom of the window are used to quickly access the Medm screens (custom screens as well as the standard testpoint screen) and the log files that are generated by the squeezer control. When pressing the configure button the *Kate* editor opens the configuration files for the squeezer. The operator can then edit these files. After saving the changed files, the read configuration button has to be pressed in order to make the changes visible to the code.

A. Self-developed applications

The following Sections give an overview of all the source code that was developed during the work for this thesis.

A.1. *CDSplot*

During the development of the automatic control for the GEO 600 squeezed light source, the tool *CDSplot* was written on top of the frame builder access library (see Appendix A.2). With this tool it is possible to plot time series and spectra of either archived data or online data that are accessed via the network data service. Therefore, *CDSplot* is a lightweight alternative to *LigoDV* and the *Dataviewer*. The update rate when viewing online data is approximately 1 Hz, so the tool can not be used as a software oscilloscope at the moment. With the current implementation of the data acquisition daemon (daqd) it is possible to realize update frequencies of 16 Hz in principle which would be sufficient to implement real-time data viewing tools in the future.

The screenshot in Figure A.1 shows the main window of *CDSplot*. At startup the application searches for a frame builder on the local network and connects to it if possible. Alternatively, the frame builder might be specified on top of the window. Within the *Channels* panel the desired channel name and its rate can be chosen from a list of all channels that are known to the frame builder. Next, the *Data acquisition* panel provides controls for choosing the kind of data (online or acquired) and the type of plot (time series or spectrum). Lastly, the *Plot settings* panel provides the setting of the plot ranges and allows to enable a logarithmic scale for each axis. Currently, all the data is piped to *Gnuplot* by using a *Python* interface. From the *Export* button on the lower panel it is possible to export either the raw data or an encapsulated postscript image of the graph.

A. Self-developed applications

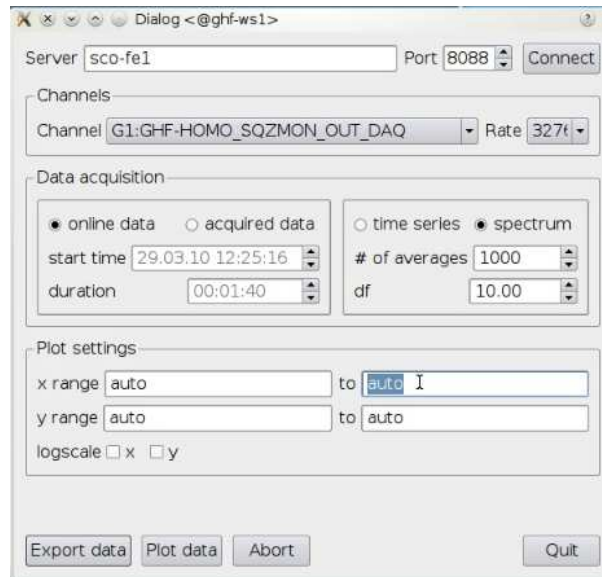


Figure A.1.: The main window of *CDSplot*.

A.2. `FB_access.py`

In order to monitor the squeezing spectrum of the GEO 600 squeezed light source, it was necessary to access the data on the frame builder. Since the automatic control of the squeezer was implemented using *Python* classes, it was decided to also provide a frame builder access library within this language. The module `FB_access.py` provides the following functions

LoadLibDaqxs () There is an underlying C-library that was written by Alex Ivanov that provides the most basic functions for interacting with the frame builder. This library must be located in the path that is set by the environment variable `AEICDS_LIB`. It is usually not necessary to call the function `LoadLibDaqxs` by the user, since all the other functions will call it.

FindFramebuilder () Returns the name and the port of the first frame builder that was found on the local network.

ConnectToFramebuilder (server, port) Tries to connect to the specified frame builder.

DisconnectFromFramebuilder() Disconnects from the frame builder. Since there is only one frame builder that can be accessed by the library at a time it is not necessary to provide the frame builder to this function.

A.3. JamMt - Just another mode matching tool

GetChannelListFromFramebuilder (server, port) Returns a list of all channels that are known to the frame builder including their acquisition rates.

GetDataFromFramebuilder (server, port, channelname, rate, duration) The data of a certain channel is returned at the chosen rate and for the defined duration. Optionally, the start time may be specified as well.

GetSpectrum (data, samplefreq, navg = 1, df = None) Returns the spectrum of the data that was returned by the previous function call. The number of averages and the frequency resolution may be given as optional arguments.

A.3. JamMt - Just another mode matching tool

JamMt is a Java application that lets the user interactively shift lenses and gives online feedback on how a Gaussian beam transforms. This makes it a useful tool to do modematchings for optical experiments. JamMt is based on a previous tool that was written by Andre Thüring in C++.

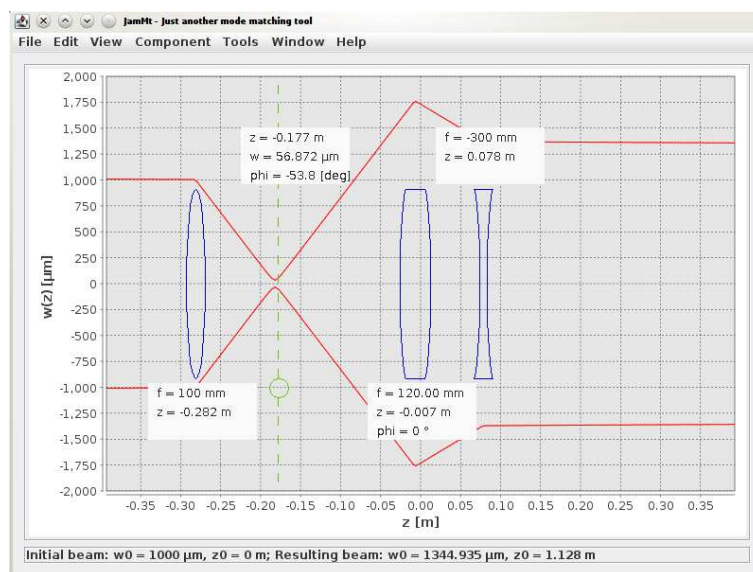


Figure A.2.: Main window of JamMt

The main features of this tool are

- Automatically search for mode matchings provided certain boundary conditions

A. Self-developed applications

- Simulation of linear cavities (calculation of eigenmode)
- Thick (i.e. real) lenses can be used
- Materials can be defined using their Sellmeier equation

JamMt can be downloaded from the following web page

<http://www.sr.bham.ac.uk/dokuwiki/doku.php?id=geosim:jammt>

For more information and usage instructions see the documentation that comes with the application.

A.4. rtmodule

This is a shell script that serves as a wrapper around the compilation and installation commands that are needed when creating real-time modules for the CDS system. It has to be run on the front-end machine. The usage of this script is

```
rtmodule xyz.mdl cmd
```

where 'xyz' is the name of the model and 'cmd' is either one of

compile	-	compile the model
install	-	install the model
clean	-	cleaning up directories
start	-	start the model
stop	-	kill the model
check	-	perform some tests on the system
log	-	show the log file
all	-	clean, compile, install, check, start, log

The typical usage is to run

```
rtmodule xyz.mdl all
```

to invoke a clean build of the Simulink model and finally start the model.

Another feature of this script is that you can provide a file *ChannelList_xyz.txt* where all the channels are listed that are to be acquired (xyz is the name of your model). If this file exists, your channel list will be build from scratch and the channels defined in *ChannelList_xyz.txt* will be acquired. The file may contain two columns separated by a comma. The first one is the channel name and the second column is the data acquisition rate which is optional.

All C code that is placed inside the folder *c-code* will automatically be included in the build. These functions belong to the *cdsFunctionCall* part in the Simulink model.

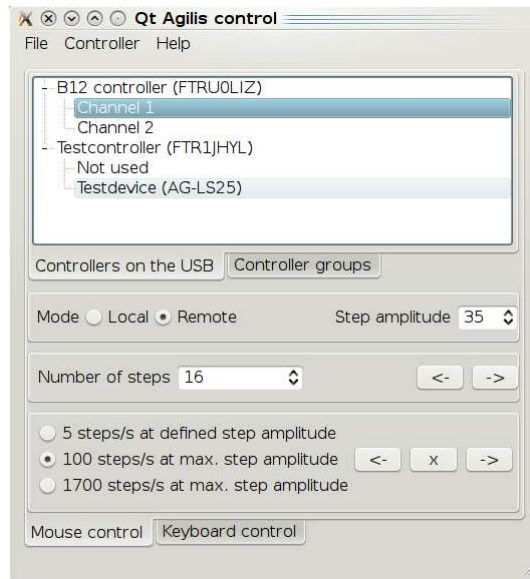


Figure A.3.: Main window of QtAgilisControl

A.5. QtAgilisControl

This application is a graphical user interface for accessing the Agilis controllers from Newport [48]. QtAgilisControl uses the *libaguc2* (see Appendix A.6) to access the controllers via USB port. The user can interact either with the mouse or via keyboard with the controllers. In the latter case, the shortcuts can be defined by the user for each controller via a simple configuration file. Since the controllers are identified by their unique controller ID (specified by the manufacturer) it is possible to address controller specific keys. Different controllers may also be grouped so that they react simultaneously on user commands. This way it is possible to operate controllers in common mode or differential mode. Figure A.3 shows the main window of the application. For more information see the online help that comes with the program.

A.6. libaguc2

This library includes functions for accessing the Agilis controllers from Newport [48] by using the *libftdi* [49]. The latter library provides functions to talk to FTDI's USB to serial converter chips. The Agilis controllers can be used to operate PZT driven linear stages, mirror mounts or rotation stages.

The header file for this library includes data structures to specify a single Agilis controller as well as a whole group of controllers. Furthermore, all features of the

A. Self-developed applications

controllers can be accessed by easy to use functions. The content of this header file is shown in the following listing

```
/** @file ag-uc2.h
 * Definition of function that are used to interact with the AG-UC2 controller.
 */
5
#ifdef __AG_UC2_H__
#define __AG_UC2_H__

#include <stdio.h>
10 #include <string.h>
#include <stdlib.h>

#include "ftdi.h"

15 #ifdef WIN32
#define sleep(x) Sleep(x)
#endif

#define USB_DBG_LVL 0 /**< libusb debug level */
20 #define VENDOR_ID 0x104d /**< Vendor Id of the AG-UC2 controller */
#define PRODUCT_ID 0x3000 /**< Product Id of the AG-UC2 controller */

#define CMDSIZE 65 /**< Size of the command array (minimum size is 65) */
#define EOL "\r\n" /**< Command terminator */
25

/** This structure defines a certain AG-UC2 controller. */
typedef struct {
    char name[80]; /**< Human readable name for the controller */
    char chn1[80], chn2[80]; /**< Human readable name for each channel */
30    char serial_nr[80]; /**< The controllers unique serial number */
    int amp1, amp2; /**< the step amplitudes for each channel */
    int jog1, jog2; /**< the jog mode for each channel */
    int nstep1, nstep2; /**< the step number for each channel */
    char fkey1, bkey1, fkey2, bkey2; /**< keys to step forward/backward */
35    struct usb_device *dev; /**< The libusb structure to handle the device */
} agilis_controller;

/** This structure implements a single linked list for controller groups */
typedef struct list_element{
40    struct list_element *next; /**< pointer for the next element in the list */
    agilis_controller *ag_ctrl; /**< member of the controller group */
    int axis; /**< the axis of the controller that is member of the group */
    int fact; /**< the step number is multiplied by this number to allow for common/differential modes */
} agilis_group_member;
45

/** This structure defines a controller group */
typedef struct group{
    char name[80]; /**< Human readable name for the controller group */
    agilis_group_member *first; /**< pointer to the first element in the list */
50    char fkey, bkey; /**< keys to step forward/backward the hole group */
} agilis_group;

int agilis_init (agilis_controller **ag_ctrl, char *fname, int verbose);
int agilis_deinit (void);
55 int agilis_open (agilis_controller ag_ctrl);
int agilis_close (void);
int agilis_set_communication_properties (void);
int agilis_write_command (agilis_controller ag_ctrl, unsigned char *cmd, int check, unsigned char *buf, int size);
int agilis_write_config_file (agilis_controller *ag_ctrl, int ndev, agilis_group *ctrl_group, char *fname);
60 int agilis_parse_config_file (agilis_controller **ag_ctrl, int ndev, agilis_group **ctrl_group, char *fname);

int agilis_set_jog_mode (agilis_controller ag_ctrl, int axis, int mode);
int agilis_measure_position (agilis_controller ag_ctrl, int axis, int *pos);
int agilis_set_mode (agilis_controller ag_ctrl, char mode);
65 char agilis_get_mode (agilis_controller ag_ctrl);
int agilis_move_to_limit (agilis_controller ag_ctrl, int axis, int mode);
int agilis_absolute_move (agilis_controller ag_ctrl, int axis, int *pos);
int agilis_tell_limit_switch (agilis_controller ag_ctrl, unsigned char* status, int size);
int agilis_relative_move (agilis_controller ag_ctrl, int axis, int nstep);
70 int agilis_reset (agilis_controller ag_ctrl);
int agilis_stop_motion (agilis_controller ag_ctrl, int axis);
int agilis_set_step_amplitude (agilis_controller ag_ctrl, int axis, int amp);
int agilis_get_step_number (agilis_controller ag_ctrl, int axis);
int agilis_get_error (agilis_controller ag_ctrl, unsigned char* error, int size);
75 int agilis_tell_steps (agilis_controller ag_ctrl, int axis);
```


A.7. Extending the power of N.L.C.S.

```
int agilis_get_status (agilis_controller ag_ctrl, int axis, unsigned char* status, int size);
int agilis_firmware_version (agilis_controller ag_ctrl, unsigned char* fv, int size);
int agilis_zero_position (agilis_controller ag_ctrl, int axis);

80 int agilis_get_jog_mode (agilis_controller ag_ctrl, int axis, unsigned char *mode, int size);
int agilis_get_step_amplitude (agilis_controller ag_ctrl, int axis, char direction);
int agilis_group_init (agilis_group *ctrl_group);
int agilis_group_append(agilis_group *ctrl_group, agilis_controller *ag_ctrl, int axis, int fact);
int agilis_group_set_step_amplitude(agilis_group grp, int amp);
85 int agilis_group_relative_move(agilis_group grp, int steps);
int agilis_group_absolute_move(agilis_group grp, int *pos);
int agilis_group_set_jog_mode(agilis_group grp, int jog);
int agilis_group_stop_motion(agilis_group grp);

90 int agilis_get_index (agilis_controller *ag_ctrl, int ndev, char *serial_nr);
char* strip (char* string, int size);

#endif
```

A.7. Extending the power of N.L.C.S.

Although N.L.C.S. has a lot of options on how to display the calculated data, there might be situations where it can not produce a desired plot. Examples are to scan an unsupported parameter or to maximize some quantity over a parameter other than the scan parameter (see Figure 3.5). The next listing shows a *Python* script that was used to scan the squeezing of the input states to produce the plots for the *v-class* and *s-class* entanglement at a beamsplitter (see Figure 3.8).

```
import os

scanrange = (0.0, -20.0)
5 steps = 10

def generateConfig (sqz):
    cfg = """
    Laser {
10     Port 1 { Xp = {%lf, %lf}}

        Port 2 {
            Xp = {%lf}
            theta = {0.5}
15     }
    }

    Cavity { Mirror 1 { R = {0.5, 0.5}}}

20 Plot {
    step = 1
    scan = "homodyne angle"
    y = "entanglement"
    range = {0, 2}
25 }
    """ % (sqz, sqz, sqz)
```

A. Self-developed applications

```
        fout = open('tmp.nlcs', 'w')
        fout.write(cfg)
30     fout.close()

    def runNLCS ():
        os.system('./nlcs-0.11 -c tmp.nlcs tmp2.dat')

35     def getEntanglement ():
        fin = open('tmp2.dat')
        line = fin.readline()
        fin.close()

40     return float(line.split()[27]), float(line.split()[32])

    if __name__ == '__main__':
        fout = open('tmp3.dat', 'w')
        for i in xrange (steps):
45             sqz = scanrange[0] + \
                    i*(scanrange[1] - scanrange[0])/(steps - 1)
                generateConfig(sqz)
                runNLCS()
                s_class, v_class = getEntanglement()
50             fout.write('%e\t%e\t%e\n' % (sqz, s_class, v_class))

        fout.close()
```

The main function beginning at line 42 loops over the scan parameter which is in this case the squeezing level in dB. For each value of the parameter the function *generateConfig* is called that writes a new configuration file for N.L.C.S. inserting the actual squeezing value. The next step is to run N.L.C.S. using only the *-c* option. This invokes only a calculation of the system without plotting the result in the end. The last step is then to parse the amount of entanglement from the data file by calling *getEntanglement*. Since the homodyne angle is scanned in this example and the entanglement does not depend on this value, it is sufficient to parse the entanglement from the first data set in the output file. For other situations it might be needed to find e.g. the maximum of the data in a specific column within each file (see Figure 3.5 for an example).

B. Steepest slope position of an Airy peak deformed by the Kerr-effect

The field E_{trans} in transmission of an optical resonator is described by the function

$$E_{\text{trans}} = \frac{te^{t\frac{\delta}{2}}}{1 - re^{t\delta}} E_{\text{in}}, \quad (\text{B.1})$$

where E_{in} is the complex field amplitude of the incident light field, $t = t_1 t_2$ and $r = r_1 r_2$ is the product of the mirror amplitude transmissivities and reflectivities, respectively. For reasonably high values of the finesse F , the bandwidth of the Airy peak $\delta\nu$ is given by

$$\delta\nu = \frac{\text{FSR}}{F}, \quad (\text{B.2})$$

where FSR is the cavities free spectral range. This means that the Airy peak is located within a range of $2\pi/F$ of the detuning parameter δ . Therefore we can assume that $\delta \ll 1$ and the transmitted power P_{trans} can be written as

$$\begin{aligned} P_{\text{trans}}(\delta) &= |E_{\text{trans}}|^2 \\ &= \frac{t^2 P_{\text{in}}}{1 + r^2 - 2r \cos(\delta)} \\ &\approx \frac{t^2 P_{\text{in}}}{1 + r^2 - 2r(1 - \frac{\delta^2}{2})}. \end{aligned} \quad (\text{B.3})$$

Here, P_{in} is the power of the incident beam and we expanded the cosine term for small arguments. By setting the second derivative of the approximated expression for the transmitted power to zero, we get the detuning δ_0 at which the slope of the Airy peak is maximized. This position reads

$$\delta_0 = \pm \frac{1 - r}{\sqrt{3r}}. \quad (\text{B.4})$$

Inserting this value into the expression for P_{trans} and normalizing it to the highest peak value at $\delta = 0$ we get

$$\xi = \frac{P_{\text{trans}}(\delta_0)}{P_{\text{trans}}(0)} = \frac{3}{4}. \quad (\text{B.5})$$

B. Steepest slope position of an Airy peak deformed by the Kerr-effect

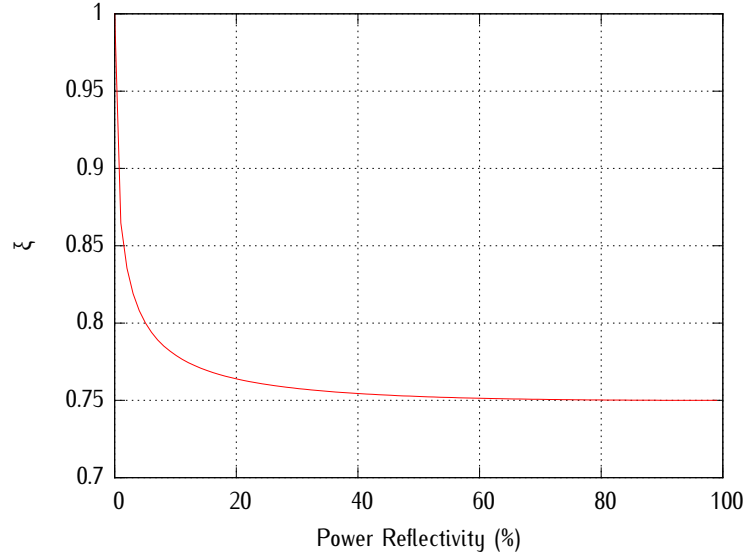


Figure B.1.: Exact position of the steepest slope of an Airy peak.

This means that the steepest slope of an Airy peak occurs when the transmitted power amounts to 75 % of the maximum power in transmission. Figure B.1 shows the exact position of the steepest slope for arbitrary reflectivities. The approximation is valid for mirror reflectivities greater than $R \approx 60\%$.

For the optical Kerr-effect , the detuning reads

$$\delta' = \delta + n_2|E|^2, \quad (\text{B.6})$$

where E is the intra-cavity field amplitude and n_2 is the so-called Kerr constant. Since the transmitted field is proportional to the intra-cavity field, the Airy peak is now given by an implicit function of the form

$$y(x) = [1 + a \cos(x + b y(x))]^{-1}. \quad (\text{B.7})$$

From the derivative of the implicit equation $F(x, y(x)) = 0$ it follows

$$y'(x) = -\frac{\partial_x F}{\partial_y F}, \quad (\text{B.8})$$

and with this equation one gets the second derivative of the implicit function $y(x)$, which is given by

$$y''(x) = -\frac{1}{F_y^3} \left(F_{xx} F_y^2 + F_{yy} F_x^2 - 2F_y F_x F_{xy} \right). \quad (\text{B.9})$$

Here, $F_x = \partial_x F$ denotes the partial derivative. For the Airy peak of a Kerr cavity the following relations between the derivatives are valid

$$F_y = 1 + b F_x, \quad (\text{B.10})$$

$$F_{yy} = b^2 F_{xx}, \quad (\text{B.11})$$

$$F_{xy} = b F_{xx}. \quad (\text{B.12})$$

Setting $y''(x) = 0$ and inserting these relations yields

$$\begin{aligned} 0 &= F_{xx} F_y^2 + F_{yy} F_x^2 - 2F_y F_x F_{xy}, \\ &= F_{xx} (1 + b F_x)^2 + b^2 F_{xx} F_x^2 - 2b F_{xx} F_x (1 + b F_x), \\ &= F_{xx}. \end{aligned} \quad (\text{B.13})$$

This means that the condition for the second derivative of the Kerr Airy peak being zero is exactly the same as for the ordinary Airy peak and therefore the steepest slope occurs also at 75 % of the maximally transmitted power for high enough reflectivities.

Bibliography

- [1] T. Maiman, “Stimulated optical radiation in ruby,” *Nature*, vol. 187, no. 4736, pp. 493–494, 1960.
- [2] P. Franken, G. Weinreich, C. Peters, and A. Hill, “Generation of optical harmonics,” *Physical Review Letters*, vol. 7, no. 4, pp. 118–119, 1961.
- [3] R. Slusher, B. Yurke, L. Hollberg, and J. Mertz, “Observation of squeezed states generated by a cavity 4-wave mixer,” *JOSA A*, vol. 2, no. 13, pp. P107–P108, 1985.
- [4] H. Vahlbruch, S. Chelkowski, B. Hage, A. Franzen, K. Danzmann, and R. Schnabel, “Coherent control of vacuum squeezing in the gravitational-wave detection band,” *Physical Review Letters*, vol. 97, pp. 011101/1–4, July 2006.
- [5] H. Vahlbruch, M. Mehmet, S. Chelkowski, B. Hage, A. Franzen, N. Lastzka, S. Gossler, K. Danzmann, and R. Schnabel, “Observation of squeezed light with 10-db quantum-noise reduction,” *Physical Review Letters*, vol. 100, pp. 033602/1–4, January 2008.
- [6] H. Vahlbruch, A. Khalaidovski, N. Lastzka, C. Gräf, K. Danzmann, and R. Schnabel, “The Geo 600 squeezed light source,” *Class. Quantum Grav.*, vol. 27, p. 084027 (8 pp.), April 2010.
- [7] G. D. Boyd and D. A. Kleinman, “Parametric interaction of focused gaussian light beams,” *Journal of applied physics*, vol. 39, pp. 3597–3639, July 1968.
- [8] G. Vidal and R. Werner, “Computable measure of entanglement,” *Physical Review A*, vol. 65, pp. 032314/1–11, March 2002.
- [9] P. Hello and J.-Y. Vinet, “Analytical models of thermal aberrations in massive mirrors heated by high power laser beams,” *J. Phys. France*, vol. 51, pp. 1267–1282, 1990.
- [10] P. Hello and J.-Y. Vinet, “Numerical model of transient thermal effects in high power optical resonators,” *J. Phys. France*, vol. 3, pp. 717–732, 1993.
- [11] N. Lastzka, J. Steinlechner, S. Steinlechner, and R. Schnabel, “Measuring small absorptions by exploiting photothermal self-phase modulation,” *Appl. Opt.*, vol. 49, pp. 5391–5398, 2010.

Bibliography

- [12] W. Winkler, K. Danzmann, A. Rüdiger, and R. Schilling, “Heating by optical-absorption and the performance of interferometric gravitational-wave detectors,” *Physical Review A*, vol. 44, pp. 7022–7036, December 1991.
- [13] V. Braginsky, M. Gorodetsky, and S. Vyatchanin, “Thermodynamical fluctuations and photo-thermal shot noise in gravitational wave antennae,” *Physics Letters A*, vol. 264, pp. 1–10, December 1999.
- [14] V. Loriette and D. Boccara, “Absorption of low-loss optical materials measured at 1064 nm by a position-modulated collinear photothermal detection technique,” *Applied Optics*, vol. 42, pp. 649–656, February 2003.
- [15] Siegmann, *Laser*. University Science Books, 1986.
- [16] R. W. Boyd, “Intuitive explanation of the phase anomaly of focused light beams,” *J. Opt. Soc. Am.*, vol. 70, no. 7, pp. 877–880, 1979.
- [17] S. Feng and H. Winful, “Physical origin of the gouy phase shift,” *Optics Letters*, vol. 26, pp. 485–487, April 2001.
- [18] A. Freise, *Finesse Manual*. <http://www.gwoptics.org/finesse/download/Finesse-0.99.8.pdf>.
- [19] G. A. Reider, *Photonik. Eine Einführung in die Grundlagen*. Springer Verlag, 1997.
- [20] G. Heinzl, “Resonant sideband extraction - Neuartige Interferometrie für Gravitationswellendetektoren,” Master’s thesis, AEI Hannover, 1995.
- [21] C. Caves and B. Schumaker, “New formalism for 2-photon quantum optics: 1. quadrature phases and squeezed states,” *Physical Review A*, vol. 31, no. 5, pp. 3068–3092, 1985.
- [22] R. W. Boyd, *Nonlinear optics*. Academic Press, second ed., 2003.
- [23] F. Zernike and J. E. Midwinter, *Applied Nonlinear Optics*. Dover Publications, 1973.
- [24] <http://www.sr.bham.ac.uk/dokuwiki/doku.php?id=geosim:n.l.c.s>.
- [25] N. Lastzka, “Analyse nichtlinearer Resonatoren,” Master’s thesis, AEI Hannover, 2005.
- [26] <http://www.nongnu.org/confuse/>.

- [27] J. DiGuglielmo, B. Hage, A. Franzen, J. Fiurasek, and R. Schnabel, “Experimental characterization of gaussian quantum-communication channels,” *Physical Review A*, vol. 76, pp. 012323/1–9, July 2007.
- [28] R. Schnabel, J. Harms, K. Strain, and K. Danzmann, “Squeezed light for the interferometric detection of high-frequency gravitational waves,” *Classical and Quantum Gravity*, vol. 21, pp. S1045–S1051, Sp. Iss. SI March 7 2004.
- [29] S. Chelkowski, H. Vahlbruch, B. Hage, A. Franzen, N. Lastzka, K. Danzmann, and R. Schnabel, “Experimental characterization of frequency-dependent squeezed light,” *Physical Review A*, vol. 71, pp. 013806/1–8, January 2005.
- [30] J. Maeda and K. Kikuchi, “Squeezing characteristics analysis of a fundamental-confined second-harmonic generation system by means of a self-consistent method,” *JOSA B*, vol. 14, pp. 481–493, March 1997.
- [31] Z. Ou, “Propagation of quantum fluctuations in single-pass 2nd-harmonic generation for arbitrary interaction length,” *Physical Review A*, vol. 49, pp. 2106–2116, March 1994.
- [32] D. F. Walls and G. J. Milburn, *Quantum Optics*. Springer, second ed., 1995.
- [33] A. White, J. Mlynek, and S. Schiller, “Cascaded second-order nonlinearity in an optical cavity,” *Europhysics Letters*, vol. 35, pp. 425–430, August 1996.
- [34] S. Chaturvedi, K. Dechoum, and P. D. Drummond, “Limits to squeezing in the degenerate optical parametric oscillator,” *PRA*, vol. 65, pp. 1–15, February 2002.
- [35] K. Arai, R. Takahashi, D. Tatsumi, K. Izumi, Y. Wakabayashi, H. Ishizaki, M. Fukushima, T. Yamazaki, M. Fujimoto, A. Takamori, K. Tsubono, R. DeSalvo, A. Bertolini, S. Marka, V. Sannibale, T. Uchiyama, O. Miyakawa, S. Miyoki, K. Agatsuma, T. Saito, M. Ohashi, K. Kuroda, I. Nakatani, S. Telada, K. Yamamoto, T. Tomaru, T. Suzuki, T. Haruyama, N. Sato, A. Yamamoto, and T. Shintomi, “Status of japanese gravitational wave detectors,” *Classical and Quantum Gravity*, vol. 26, p. 204020 (9 pp.), October 2009.
- [36] <http://www.et-gw.eu>.
- [37] U. Willamowski, T. Gross, D. Ristau, and H. Welling, “Calorimetric measurement of optical absorption at 532nm and 1064nm according to iso/fdis 11551,” *LBOC - Third International Workshop on Laser Beam and Optics Characterization*, vol. 2870, pp. 483–494, 1996.
- [38] S. Hild, H. Lück, W. Winkler, K. Strain, H. Grote, J. Smith, M. Malec, M. Hewitson, B. Willke, J. Hough, and K. Danzmann, “Measurement of a low-absorption

Bibliography

- sample of oh-reduced fused silica,” *Applied Optics*, vol. 45, pp. 7269–7272, October 1 2006.
- [39] M. Evans, S. Ballmer, M. Fejer, P. Fritschel, G. Harry, and G. Ogin, “Thermo-optic noise in coated mirrors for high-precision optical measurements,” *Physical Review D*, vol. 78, pp. 102003/1–10, November 2008.
- [40] L. Matone, M. Barsuglia, F. Bondu, F. Cavalier, H. Heitmann, and N. Man, “Finesse and mirror speed measurement for a suspended fabry-perot cavity using the ringing effect,” *PRA*, vol. 271, pp. 314–318, July 2000.
- [41] <http://www.ligo.caltech.edu/~rolf/>.
- [42] <http://www.aps.anl.gov/epics/>.
- [43] <http://www.aps.anl.gov/epics/extensions/index.php>.
- [44] <http://cars9.uchicago.edu/newville/Epics/Python/doc/EpicsCA.html>.
- [45] E. Gamma, R. Helm, R. Johnson, and J. M. Vlissides, *Design Patterns: Elements of Reusable Object-Oriented Software*. Addison-Wesley, 1994.
- [46] <http://docs.python.org/library/logging.html>.
- [47] <http://www.riverbankcomputing.co.uk/software/pyqt/intro>.
- [48] http://search.newport.com/?q=*%&x2=sku&q2=AG-UC2.
- [49] <http://www.intra2net.com/en/developer/libftdi/>.

Publications

— 2010 —

1. N. Lastzka, J. Steinlechner, S. Steinlechner, and R. Schnabel, “Measuring small absorptions by exploiting photothermal self-phase modulation,” *Appl. Opt.*, vol. 49, pp. 5391–5398, 2010.
2. J. Abadie, ..., N. Lastzka, ..., “Predictions for the rates of compact binary coalescences observable by ground-based gravitational-wave detectors,” *Classical and Quantum Gravity*, vol. 27, September 2010.
3. J. Abadie, ..., N. Lastzka, ..., “Search for gravitational-wave inspiral signals associated with short gamma-ray bursts during ligo’s fifth and virgo’s first science run,” *Astrophysical Journal*, vol. 715, pp. 1453–1461, June 2010.
4. H. Vahlbruch, A. Khalaidovski, N. Lastzka, C. Gräf, K. Danzmann, and R. Schnabel, “The Geo 600 squeezed light source,” *Class. Quantum Grav.*, pp. 084027 (8 pp.), vol. 27, 2010.
5. J. Abadie, ..., N. Lastzka, ..., “All-sky search for gravitational-wave bursts in the first joint ligo-geo-virgo run,” *Physical Review D*, vol. 81, pp. 102001 (20 pp.), May 2010.
6. M. Mehmet, H. Vahlbruch, N. Lastzka, K. Danzmann, and R. Schnabel, “Observation of squeezed states with strong photon-number oscillations,” *Physical Review A*, vol. 81, pp. 013814/1-7, January 2010.

— 2009 —

7. A. Khalaidovski, A. Thuring, H. Rehbein, N. Lastzka, B. Willke, K. Danzmann, and R. Schnabel, “Strong reduction of laser power noise by means of a kerr nonlinear cavity,” *Physical Review A*, vol. 80, pp. 053801 (7 pp.), November 2009.

Bibliography

— 2008 —

8. H. Vahlbruch, M. Mehmet, S. Chelkowski, B. Hage, A. Franzen, **N. Lastzka**, S. Gossler, K. Danzmann, and R. Schnabel, “Observation of squeezed light with 10-db quantum-noise reduction,” *Physical Review Letters*, vol. 100, pp. 033602/1-4, January 2008.

— 2007 —

9. **N. Lastzka** and R. Schnabel, “The gouy phase shift in nonlinear interactions of waves,” *Optics Express*, vol. 15, pp. 7211–7217, June 2007.

— 2005 —

10. **N. Lastzka**, “Analyse nichtlinearer Resonatoren,” Master’s thesis, AEI Hannover, 2005.
11. S. Chelkowski, H. Vahlbruch, B. Hage, A. Franzen, **N. Lastzka**, K. Danzmann, and R. Schnabel, “Experimental characterization of frequency-dependent squeezed light,” *Physical Review A*, vol. 71, pp. 013806/1-8, January 2005.

Acknowledgements

First I would like to thank Prof. Dr. Karsten Danzmann for giving me the opportunity to work at such a great institute. For the mentoring and encouragement over the years I'm grateful to Prof. Dr. Roman Schnabel. It was an exciting experience to be part of the squeezing group from the first generation of squeezed states of light in Hanover to the first implementation of a squeezed light source at a gravitational wave detector.

The daily work was unburdened by many people. My special thank goes to my long time roommate James DiGuglielmo and my earlier mates Moritz Mehmet and Gudrun Wanner. For sharing my anger produced by the CDS when implementing the software control for GEO 600 but also for the fun times we had, I would like to thank Christian Gräf, Alexander Khalaidovski and Henning Vahlbruch. The generation of nice images is fun since Alexander Franzen created his *Component Library* and made it available not only for *Illustrator* users. Thanks Ali!

For proofreading this manuscript and fruitful discussions I would like to thank Helge Müller-Ebhardt, Gerrit Kühn, Christian Gräf, Henning Vahlbruch, Aiko Sambrowski and Andre Thüning.

My family and my parents in-law supported and encouraged me all the time. Without them this thesis would not have been possible at all. And finally, twelve points go to the loveliest person on the planet – Frauke, this is for you!

Nico Lastzka, October 2010